MODELING CIRCULATION DYNAMICS AND SUBMARINE MELT IN

GREENLAND FJORDS

by

DUSTIN CARROLL

A DISSERTATION

Presented to the Department of Earth Sciences
and the Graduate School of the University of Oregon
in partial fulfillment of the requirements
for the degree of
Doctor of Philosophy

June 2017

DISSERTATION APPROVAL PAGE

Student: Dustin Carroll

Title: Modeling Circulation Dynamics and Submarine Melt in Greenland Fjords

This dissertation has been accepted and approved in partial fulfillment of the requirements for the Doctor of Philosophy degree in the Department of Earth Sciences by:

Alan W. Rempel	Chairperson
David A. Sutherland	Core Member
Joshua J. Roering	Core Member
Emily L. Shroyer	Core Member
Mark Carey	Institutional Representative

and

Scott L. Pratt   Dean of the Graduate School

Original approval signatures are on file with the University of Oregon Graduate School.

Degree awarded June 2017

DISSERTATION ABSTRACT

Dustin Carroll

Doctor of Philosophy

Department of Earth Sciences

June 2017

Title: Modeling Circulation Dynamics and Submarine Melt in Greenland Fjords

Meltwater accumulated on the Greenland Ice Sheet drains to glacier beds, discharging into fjords hundreds of meters below sea level. The injection of meltwater at depth generates an upwelling plume that entrains warm ocean water as it rises along the terminus, increasing submarine melt and driving a fjord-scale exchange flow. However, due to sparse ocean-glacier observations, we lack a process understanding of how plumes control fjord circulation and submarine melt. Combining numerical modeling, theory, and observations, this dissertation investigates near-glacier plume dynamics, the influence of glacier depth on plume structure and submarine melt, and the role of fjord-glacier geometry on circulation in tidewater glacier fjords.

In Chapter II, I use buoyant plume theory and a nonhydrostatic, three-dimensional ocean–ice model to investigate the sensitivity of plume dynamics to subglacial discharge, turbulent diffusivity, and conduit geometry. Large discharges result in plumes with positive temperature and salinity anomalies in the upper water column. Fjord circulation is sensitive to conduit geometry; distributed subglacial discharge results in a stronger return flow of warm water toward the terminus. In Chapter III, I use buoyant plume theory, initialized with realistic ranges of subglacial discharge, glacier depth, and ocean

stratification, to investigate how plume structure and submarine melt vary during summer months in 12 Greenland fjords. Grounding line depth is a primary control on plume-induced submarine melt: deep glaciers produce warm, salty subsurface plumes that undercut termini, and shallow glaciers produce cold, fresh surface-confined plumes that can overcut. Finally, in Chapter IV, I use regional-scale numerical ocean simulations to systematically evaluate how fjord circulation forced by subglacial plumes, tides, and wind stress depends on fjord width, glacier depth, and sill height. Glaciers grounded below sill depth can draw shelf waters over a shallow sill and into fjord basins with seasonal subglacial discharge; this process is independent of external shelf forcing. These results underscore the first-order effect that subglacial discharge and fjord-glacier geometry have in controlling fjord circulation and, thus, ocean heat flux to the ice.

This dissertation includes previously published and co-authored material.

CURRICULUM VITAE

NAME OF AUTHOR: Dustin Carroll

GRADUATE AND UNDERGRADUATE SCHOOLS ATTENDED:

University of Oregon, Eugene, OR
Moss Landing Marine Laboratories, California State University Monterey Bay,
    Marina, CA
Westmont College, Santa Barbara, CA

DEGREES AWARDED:

Doctor of Philosophy, Earth Sciences, 2017, University of Oregon
Master of Science, Marine Science, 2009, Moss Landing Marine Laboratories,
        California State University Monterey Bay
Bachelor of Science, Computer Science, 2004, Westmont College

AREAS OF SPECIAL INTEREST:

Physical Oceanography
Ocean-ice Interactions
Numerical Ocean Modeling

PROFESSIONAL EXPERIENCE:

Graduate Teaching and Research Fellow, University of Oregon,
        Department of Earth Sciences, 2012-2017

Arctic LTER Research Technician, University of Michigan, 2011-2012

Chief Software Engineer, Moss Landing Marine Laboratories, 2009-2011

Research Assistant, Central and Northern California Ocean Observing System,
        2007-2009

Summer Intern, Monterey Bay Aquarium Research Institute, 2006

Software Engineer, Scientific Drilling International, 2005

Research Assistant, Westmont College, Department of Chemistry, 2003-2004

GRANTS, AWARDS AND HONORS:

Research Excellence Award, Department of Geological Sciences,
University of Oregon, 2016

Baldwin Scholarship, Department of Geological Sciences,
University of Oregon, 2016

Bayer Scholarship, Department of Geological Sciences,
University of Oregon, 2015

Thayer Scholarship, Department of Geological Sciences,
University of Oregon, 2014

AGU Outstanding Student Paper Award, 2013

Johnston Fellowship, Department of Geological Sciences,
University of Oregon, 2012

NSF Antarctic Service Medal, 2010

PUBLICATIONS:

Moon, T., Sutherland, D.A., **Carroll, D**. , Felikson, D., Kehrl, L.M., and F. Straneo. Subsurface iceberg melt key to Greenland fjord freshwater budget, "in review".

Carroll, D. , Sutherland, D.A., Shroyer, E.L., Nash, J.D., Catania, G.A., and L.A. Stearns. Subglacial discharge-driven renewal of tidewater glacier fjords, "in review".

Jackson, R.H., Shroyer, E.L., Nash, J.D., Sutherland, D.A., **Carroll, D**. , Fried, M.J., Catania G.A., Bartholomaus, T.C., and L.A. Stearns. Subglacial plume structure and transport from repeat near-glacier surveying: implications for plume parameterizations, "in review".

Amundson, J.M. and **D. Carroll**. Topographic modulation of subglacial discharge and submarine melting during tidewater glacier retreat, "in revision".

Carroll, D., Sutherland, D.A., Hudson, B., Moon T., Catania, G.A., Shroyer, E.L., Nash, J.D., Bartholomaus, T.C., Felikson D., Stearns, L.A., Noël, B.P., and M.R. van den Broeke. 2016. The impact of glacier geometry on meltwater plume structure and submarine melt in Greenland fjords. Geophysical Research Letters, 43(18): 9739-9748.

Breaker, L.C., Loor, H.R., and **D. Carroll**. 2016. Trends in sea surface temperature off the coast of Ecuador and the major processes that contribute to them. Journal of Marine Systems, 164, 151-164.

Bartholomaus, T.C., Stearns, L.A., Sutherland, D.A., Shroyer, E.L., Nash, J.D., Walker, R., Catania, G., Felikson, D., **Carroll, D.**, Fried, M.J., Noël, B.P., and M.R. van den Broeke. 2016. Contrasts in the response of adjacent fjords and glaciers to ice-sheet surface melt in West Greenland. Annals of Glaciology, 1-14.

Carroll, D., Sutherland, D.A., Shroyer, E.L., Nash, J.D., Catania G.A., and L.A. Stearns. 2015. Modeling turbulent subglacial meltwater plumes: implications for fjord-scale buoyancy-driven circulation. Journal of Physical Oceanography, 45(8): 2169-2185.

Breaker L.C., Murty T.S., and **D. Carroll**. 2013. A frequency domain approach for predicting the signal strength of tsunamis at coastal tide gauges. Journal of Coastal Research, 30(3): 562-574.

Breaker, L.C., Murty T.S., **Carroll, D**., and W.J Teague. 2011. The response of the Monterey Bay to the Great Tohoku Earthquake of 2011. Science of Tsunami Hazards, 30(3): 153-163.

Cazenave, F., Zook, R., **Carroll, D**., Flagg, M., and S. Kim. 2011. Development of the ROV SCINI (Submersible Capable of under Ice Navigation and Imaging) and deployment in McMurdo Sound, Antarctica. Journal of Ocean Technology, 6(3): 39-57.

Breaker, L.C., Murty T.S., Norton J. G., and **D. Carroll**. 2009. Comparing sea level response at Monterey, California from the 1989 Loma Prieta earthquake and the 1964 Great Alaskan Earthquake. Science of Tsunami Hazards, 28(5): 255-271.

Carroll, D., Broadus, R., Hanson, J., Conant, T., and A.M Nishimura. 2005. Study of the phosphorescent triplet state of 2-Indanone: Use of a microcontroller based photon counter and pulse train generator. Journal of Undergraduate Chemistry Research, 1: 85-89.

ACKNOWLEDGMENTS

This dissertation has greatly benefited from the contributions of many people. First, a huge thank you to my advisor David Sutherland for being a wonderful and supportive mentor during my Ph.D. David always provided me with the intellectual freedom to develop my own ideas, patiently guided my focus back on track when needed, and demonstrated by example that being a rigorous scholar and maintaining a work-life balance are not mutually exclusive. Additionally, I would like to thank UO committee members Mark Carey, Alan Rempel, and Josh Roering for their guidance and feedback. A special thank you to Emily Shroyer and Jonathan Nash, who provided an endless source of enthusiasm, research ideas, and advice throughout my graduate career. Finally, I would like to thank Shandy and my extended family for their unwavering love and support.

TABLE OF CONTENTS

Chapter   Page

Chapter   Page

LIST OF FIGURES

xiv

Figure   Page

CHAPTER IV

LIST OF TABLES

CHAPTER I

INTRODUCTION

Submarine melting of ice due to warm ocean waters has been increasingly implicated as a mechanism for the retreat and destabilization of marine-terminating glaciers worldwide. However, due to sparse ocean-glacier observations in these ice-choked systems, we lack a precise understanding of how ocean circulation, driven by ice sheet meltwater and shelf-forced flows, controls submarine melt rates and glacier stability. This work seeks to advance our fundamental understanding of how high-latitude fjord and glacier systems interact with the coastal ocean by investigating the following questions. How does ice sheet meltwater impact near-shore and coastal circulation? Under what conditions are glaciers most sensitive to ocean melt? What controls the flow of warm subsurface waters toward the ice? To address these questions, this dissertation uses high-resolution numerical ocean modeling, theory, and observations from Greenland fjord-glacier systems to investigate near-glacier plume dynamics, the influence of glacier depth on plume structure and submarine melt, and the role of fjord-glacier geometry on plume, wind, and tidally-forced circulation in tidewater glacier fjords.

Chapter II was coauthored with David Sutherland (University of Oregon), Emily Shroyer (Oregon State University), Jonathan Nash (Oregon State University), Ginny Catania (University of Texas in Austin), and Leigh Stearns (University of Kansas), and published in the *Journal of Physical Oceanography* in August 2015.

Meltwater accumulated on the Greenland Ice Sheet often drains to glacier beds, discharging into fjords hundreds of meters below sea level. The injection of buoyant meltwater at depth drives an upwelling plume that entrains warm ocean waters as it rises

along the ice face, increasing submarine melt and driving fjord circulation. In Chapter II, I use a high-resolution ocean–ice model to investigate the sensitivity of meltwater plume dynamics and fjord circulation to subglacial discharge rates, turbulent diffusivity, and subglacial conduit geometry. These results demonstrate that plumes with large vertical velocities penetrate to the surface near the ice face; however, fjord stratification can create a barrier that traps plumes at depth as they flow down-glacier. Large discharges result in plumes with positive temperature and salinity anomalies in the upper water column. For these flows, turbulent entrainment along the ice face acts as a mechanism to vertically transport heat and salt. This work demonstrates that fjord circulation is sensitive to conduit geometry; a distributed subglacial network results in a stronger flow of warm water toward the glacier.

Chapter III was coauthored with David Sutherland (University of Oregon), Ben Hudson (University of Washington), Twila Moon (University of Bristol), Ginny Catania (University of Texas in Austin), Emily Shroyer (Oregon State University), Jonathan Nash (Oregon State University), Tim Bartholomaus (University of Idaho), Denis Felikson (University of Texas in Austin), Leigh Stearns (University of Kansas), Brice Noël (Utrecht University), and Michiel van den Broeke (Utrecht University), and published in *Geophysical Research Letters* in October 2016.

Building upon the framework developed in Chapter II, Chapter III uses buoyant plume theory initialized with realistic ranges of subglacial discharge, glacier depth, and ocean stratification to investigate how simulated plume structure and submarine melt vary during summer months in 12 Greenland fjords. This work demonstrates that glacier depth is a strong control on plume-induced submarine melt; deep glaciers produce warm,

salty subsurface plumes that undercut termini and shallow glaciers produce cold, fresh surface-trapped plumes that support semiuniform or overcut termini. Due to sustained upwelling velocities, plumes in cold, shallow fjords can induce equivalent melt rates compared to warm, deep fjords.

Chapter IV is coauthored with David Sutherland (University of Oregon), Emily Shroyer (Oregon State University), Jonathan Nash (Oregon State University), Ginny Catania (University of Texas in Austin), and Leigh Stearns (University of Kansas), and was submitted to the *Journal of Geophysical Research: Oceans* in April 2017.

In Chapter IV, I extend the near-glacier results from Chapters II and III to the larger fjord-scale system. Here I use regional-scale numerical ocean simulations to evaluate how fjord circulation forced by plumes, tides, and wind stress depends on fjord width, grounding line depth, and the presence of submarine sills. Glaciers grounded below sill depth can draw shelf waters over a shallow sill and into fjord basins with seasonal subglacial discharge; this process is independent of external shelf forcing. Rotational effects strongly control the cross-fjord structure of the exchange flow; plumes in wide fjords develop geostrophically-balanced recirculation cells that increase the dilution and residence time of glacially-modified waters. In narrow fjords the rapid drawdown of basin waters by the vertical plume allows shelf waters to cascade deep into the basin; in wide fjords the return flow consists of a thin, boundary current that flows toward the terminus slightly below sill depth. Wind stress can significantly amplify the subglacial discharge-driven exchange flow; however, strong near-surface stratification limits wind-induced mixing to the upper water column. Tidal mixing over a sill increases in-fjord transport of deep shelf waters and erodes ambient stratification in the basin.

These results underscore the first-order importances of subglacial discharge and fjord-glacier geometry in controlling circulation and renewal in tidewater glacier fjords.

CHAPTER II

MODELING TURBULENT SUBGLACIAL MELTWATER PLUMES:

IMPLICATIONS FOR FJORD-SCALE BUOYANCY-DRIVEN CIRCULATION

This chapter was published in *Journal of Physical Oceanography* in August 2015. I was lead author on the paper, developing the methodology, analyzing the data, and writing the manuscript. David Sutherland (University of Oregon), served as advisor, aiding in data interpretation and manuscript editing. Emily Shroyer (Oregon State University), Jonathan Nash (Oregon State University), Ginny Catania (University of Texas in Austin), and Leigh Stearns (University of Kansas) provided feedback on manuscript drafts and aided in manuscript editing.

1. Introduction

Convective motions are ubiquitous in the ocean and atmosphere, arising from statically unstable density differences between a source fluid and its environment under the influence of gravity. Buoyant plumes are one example of turbulent gravitational convection, where an isolated source of buoyancy drives the mean flow (Turner 1973). These plumes, typically characterized by turbulent dynamics with high Reynolds number, occur over an enormous range of scales and are forced by both natural and anthropogenic sources, such as volcanic eruptions, hydrothermal vents at ocean ridges, fires, and the discharge of pollutants (Woods 2010).

The primary goal of this paper is to apply the general model of turbulent plumes to a timely environmental problem: the subglacial discharge of meltwater into Greenland's outlet glacier fjords. The rate of mass loss from the Greenland Ice Sheet (GrIS) quadrupled over the last two decades and currently accounts for one quarter of

global sea-level (GSL) rise (Cazenave and Llovel 2010; Straneo and Heimbach 2013; Enderlin et al. 2014). Submarine melting due to warm ocean waters has been increasingly implicated as a major factor in controlling the stability and acceleration of outlet glaciers worldwide (Joughin et al. 2012; Straneo and Heimbach 2013). With a projected GSL rise of 0.5-1.2 meters by 2100 under the IPCC "business as usual" scenario, understanding how a warming ocean contributes to dynamic mass loss from the GrIS is critical to predict and mitigate future climate change (Kopp et al. 2014).

Numerous studies indicate that subglacial discharge at the grounding line of Greenland's glaciers drives a turbulent plume that rises along or near the ice face (Motyka et al. 2003; Salcedo-Castro et al. 2011; Xu et al. 2012, 2013; Sciascia et al. 2013). The turbulent plume entrains warm Atlantic-origin water (AW) at depth, providing a mechanism for delivering heat to the ice face. In a steady state balance, the outflowing plume is balanced by a return flow of AW at depth. The resultant turbulent plume-driven flow has been proposed as a mechanism for setting up a fjord circulation pattern that transports heat to Greenland's outlet glaciers (Rignot et al. 2010; Straneo et al. 2012; Motyka et al. 2013); however, in-situ evidence that this mode of circulation governs heat transport over any timescale is lacking due to the difficulty of making sustained measurements near the glacier terminus in these remote, ice-choked fjords.

Although we lack sufficient observations to test the plume-driven circulation hypothesis, progress has been made on understanding plume dynamics near the ice-ocean interface using numerical methods. Current models include 1-D theory-based models (Jenkins 2011), 2-D numerical simulations (Salcedo-Castro et al. 2011), more complex general circulation models (GCMs) (Xu et al. 2012, 2013; Sciascia et al. 2013, 2014), and

finite-element methods (FEMs) (Kimura et al. 2014). Recent studies have parameterized

plumes in coarser fjord-scale models (Cowton et al. 2015) and investigated the effect of

subglacial hydrology on melt rates (Slater et al. 2015). Both 2-D and 3-D conduit

geometries have been modeled with subglacial discharge entering the fjord either through

a continuous crack along the grounding line (i.e., a line source) (Figure 1a) or from a

number of discrete subglacial conduits (Figure 1b).
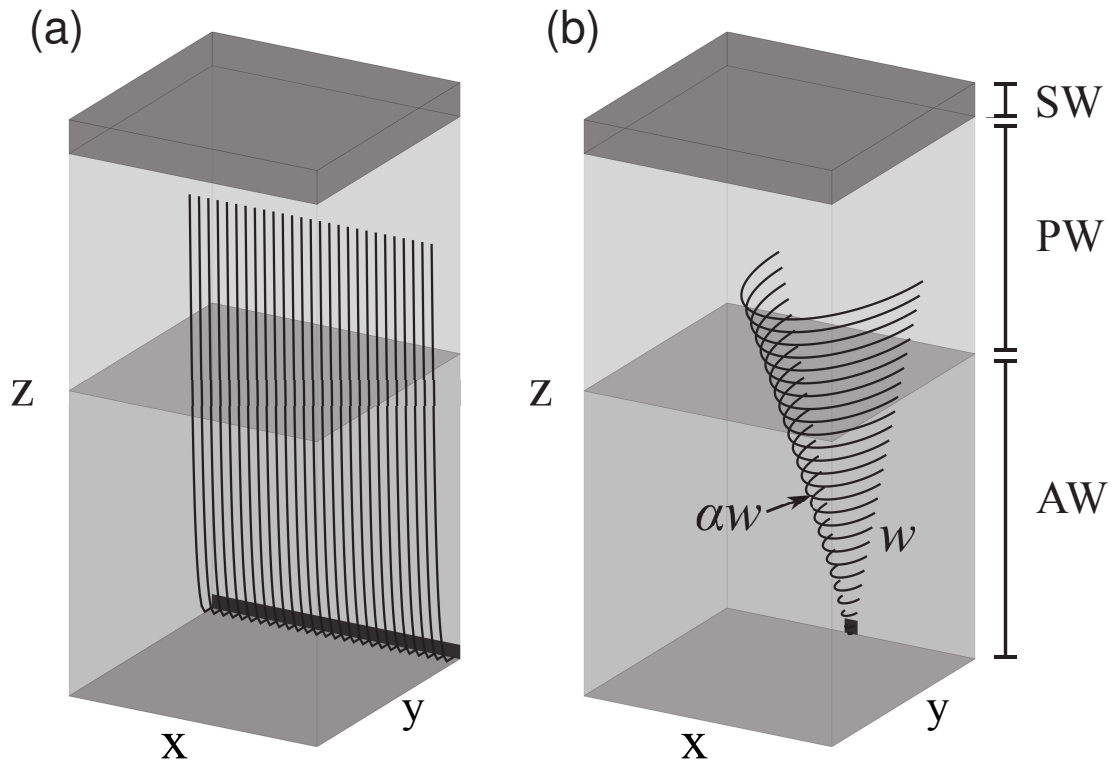
FIG. 1. Idealized schematic of (a) line and (b) point source plumes rising through a three layer stratification of Atlantic water (AW), polar water (PW), and surface water (SW) layers. In the line plume, subglacial discharge is distributed uniformly across the width of the grounding line. The point source plume is forced by a source of buoyancy discharged through a single subglacial conduit. As the plumes rise, they entrain dense ambient water and gradually lose vertical momentum.

To date, an eddy-resolving simulation with appropriate handling of the turbulent energy cascade has yet to be run, and instead models have relied on simplified parameterizations for the turbulent entrainment and diffusivity.

Previous investigators (Sciascia et al. 2013) have used line plume theory (Ellison and Turner 1959) as a basis for parameterizing turbulent entrainment in 2–D models. However, this 2–D line plume theory is not applicable to meltwater discharged from discrete subglacial conduits. Other 3-D modeling efforts have attempted to resolve the turbulent plume (i.e., ≤1-m grid spacing) from an individual channel, but these models are too computationally intensive to investigate the far- field plume (Xu et al. 2013). Additionally, coarser resolution models that resolve the fjord often assume idealized homogenous or two-layer ambient stratification (Sciascia et al. 2013; Kimura et al. 2014). Although these previous efforts have been useful, the necessary limitations imposed by numerical models combined with the expansive parameter space encompassed by the 200+ GrIS outlet glaciers highlight the need for further GCM simulations.

In this paper, we develop a general framework for determining circulation patterns forced by meltwater plume dynamics, using buoyant plume theory and a 3-D, non-hydrostatic version of the MITgcm (Marshall et al. 1997). This study differs from previous work in that we shift the focus to downstream of the ice face – investigating how basic model parameters relevant to all outlet glacier systems (e.g., subglacial discharge rates, conduit geometry, turbulent diffusivity, and fjord stratification) determine fjord-scale circulation. This approach allows us to investigate the effect of the spatial distribution of submarine melting along the glacier terminus, identify the transition between point source and line plume regimes, and quantify the downstream

properties and mixing of the plume. In order to correctly estimate the magnitude of ocean

heat transport toward the glacier in future fjord-scale models, we need to resolve the

vertical tracer structure and terminal level of the outflowing plume.

2. Background

a. Physical Setting

For the case studies considered here, the ambient temperature and salinity is based

on data collected from Rink Fjord, west Greenland (Figure 2).
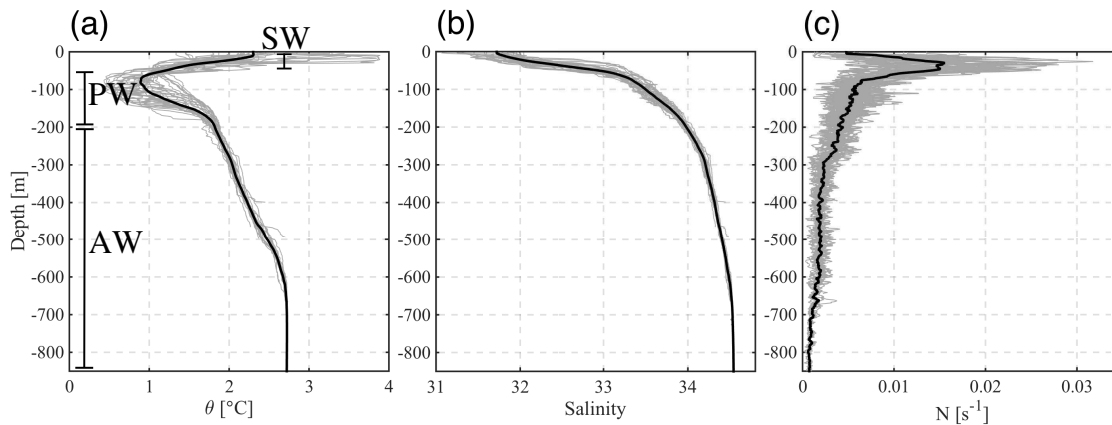
FIG. 2. (a) Potential temperature, (b) salinity, and (c) buoyancy frequency profiles from a September 2013 cruise aboard the R/V Sanna in Rink Fjord, west Greenland. Warm, fresh SW overlays cold PW. Warm, salty AW is found at depth. Mean profiles are represented with a black line.

This deep, tidewater glacier is exposed to a complex density stratification that is typical

of outlet glacier fjords in Greenland (Straneo et al. 2011; Chauché et al. 2014), providing

an ideal physical setting to investigate meltwater plumes rising through strong vertical

density gradients. Warm, salty AW occupies the bottom layer, overlaid by relatively cold,

fresh polar water (PW). A thin layer of seasonal surface water (SW), consisting of runoff

and ice melt warmed by solar radiation, is present near-surface. At many locations within

9

the fjord, conductivity/temperature/depth (CTD) measurements were taken with a 6 Hz XR-620 RBR sensor. From these temperature and salinity profiles, we calculate a mean summer buoyancy frequency $\overline{N}(z)$ profile, where the overbar represents an average of profiles taken during our synoptic survey (Figure 2c). In the summer, stratification reaches a maximum at 30 m depth, at the strong density interface between the PW and SW layer.

Estimates of subglacial discharge in GrIS fjords, such as Rink Fjord, are not well constrained and depend on unknown parameters such as: ablation rate, catchment surface area, and the efficiency of the subglacial channel network (Chu 2014). Previous investigators have estimated summer subglacial discharges of ~200-500 m^3 s^{-1} at Store Glacier (Xu et al. 2012, 2013), while estimates of surface meltwater entering Sermilik and Jakobshavn Fjord are ~174 m^3 s^{-1} (Andersen et al. 2010) and 750-1500 m^3 s^{-1} (Echelmeyer et al. 1991), respectively. Chauché et al. (2014) estimates a summer subglacial discharge into Rink Fjord of 1000±300 m^3 s^{-1} in 2009 and 1500±450 m^3 s^{-1} in 2010. Given the wide range and large uncertainties for estimates of subglacial discharge in GrIS fjords, we use a subglacial discharge flux of 1, 10, 75, 150, 300, 500 and 750 m^3 s^{-1} to simulate a variety of possible summer discharge scenarios. The discharges tested were adequate to produce a range of subsurface and surface-trapped plumes (see section 4a for details).

b. Buoyant Plume Theory

To develop insight into the interaction between subglacial buoyancy flux and stratification, we consider an idealized model of a non-rotating, axisymmetric turbulent plume discharged from a point source of buoyancy into a stratified ambient fluid. We

build upon the classical model of point source plumes in a uniformly stratified

environment (Morton et al. 1956), hereafter referred to as MTT56. The MTT56 model

has been widely used in modeling turbulent plumes for the last half-century, and has been

verified extensively using both laboratory experiments and observations over a diverse

parameter space (Turner 1973; List 1982; Woods 2010). To apply this model to Green-

land's outlet glacier fjords, we assume that the point source plume is bisected into a half-

plume by the vertical ice face, the buoyancy flux of the plume is due to steady subglacial

discharge (i.e., we assume submarine melting has a second-order effect), the plume

initially has no horizontal momentum, and the half-plume rises in a continuously

stratified ambient fluid (Caulfield and Woods 1998). To represent a half-plume, we scale

the prescribed subglacial discharge flux by a factor of two (equation 5). The MTT56

model is based upon three fundamental assumptions. First, the rate of horizontal

entrainment at the edge of the plume, u_e, is linearly proportional to the vertical velocity w

at that height,

$$u_e = \alpha w, \tag{1}$$

with the dimensionless entrainment constant α (Figure 1). The edges of a turbulent plume

entrain quiescent water from outside, progressively increasing the mass flux of the plume

as it rises. At high Reynolds number this process is independent of molecular viscosity.

We assume that the plume velocity and buoyancy have a "top-hat" profile, where the

value is constant inside the plume and zero outside. The value for the entrainment

constant depends on the choice of the plume profile; we adopt a value of α = 0.13,

representative of a pure plume forced by buoyancy alone (Linden 2000). The second

assumption is that mean vertical velocity and buoyancy exhibit self-similarity at all

heights, with a conic shape emanating from the point source (Figure 1b). Mass and momentum fluxes are defined as integrals of the mean values taken across the width of plume. The third and final assumption is that local variations of density in the plume ρ' are small compared to the background density ρ_0 (where $\rho = \rho_0 + \rho'$). Under this assumption, we invoke the Boussinesq approximation (i.e., fluxes of mass can be considered fluxes of volume).

The MTT56 formulation yields a model for three key characteristics of the plume as a function of height z above the source: the radius b, vertical velocity w, and reduced gravity $g' = \frac{\rho_p - \rho_a}{\rho_0}$, where g is the gravitational acceleration, ρ_p is the density of the plume, and ρ_a is the ambient density. Fluxes of volume Q, momentum M, and buoyancy F are expressed as

$$Q = 2\pi \int_0^\infty wr \, dr, \tag{2a}$$

$$M = 2\pi \int_0^\infty w^2 r \, dr, \text{ and} \tag{2b}$$

$$F = 2\pi \int_0^\infty wg' \, dr, \tag{2c}$$

where r is the radial distance. Averaging over the cross-sectional area of the plume leads to a system of 3 prognostic governing equations:

$$\frac{dQ}{dz} = 2\alpha M^{1/2}, \tag{3a}$$

$$\frac{dM}{dz} = \frac{QF}{M}, \text{and} \tag{3b}$$

$$\frac{dF}{dz} = -N(z)^2 Q. \tag{3c}$$

12

Following Caulfield and Woods (1998), we extend the original MTT56 formulation to have the buoyancy frequency N be a function of height above the point source instead of a constant:

$$N(z) = \sqrt{-\frac{g}{\rho_0}\frac{d\rho(z)}{dz}}. \qquad (4)$$

This system of ordinary differential equations is integrated numerically using a fourth-order Runge-Kutta method (Burden and Faires 2010). Boundary conditions for volume Q and momentum M fluxes are zero at the grounding line depth. The buoyancy flux for the half-plume is prescribed at the boundary as

$$F_0 = g'(2Q_{sg}), \qquad (5)$$

where Q_{sg} is the subglacial discharge flux. By scaling the solutions, we recover the diagnostic variables w, b, and g':

$$w \sim \frac{M}{Q}, b \sim \frac{Q}{M^{1/2}}, g' \sim \frac{F}{Q}. \qquad (6)$$

Depending on the strength of the prescribed buoyancy flux and ambient stratification, the plume reaches neutral buoyancy at depth or at the free surface. We define the plume outflow depth as the level of neutral buoyancy, where $\rho_p = \rho_a$ (i.e., where the buoyancy flux $F = 0$). As the plume reaches its maximum height (defined to be where the momentum flux $M = 0$), the assumptions of self-similarity and linear entrainment no longer hold and the integration is stopped. More complex models are required to resolve the terminal level and downstream properties of the plume.

3. Buoyant Plumes in Ocean GCMs

The extended MTT56 model provides a useful foundation for investigating point source plumes in a stratified environment; however, it only resolves plume properties

13

along the upward centerline trajectory, assumes a constant entrainment coefficient and linear model for the entrainment rate, and does not incorporate a buoyancy flux from the melting ice face. To overcome some of these limitations, we use the Massachusetts Institute of Technology general circulation model (MITgcm) in a 3-D high-resolution, non-hydrostatic configuration to simulate line and point source meltwater plumes rising along a melting glacier terminus. The MITgcm is a developed version of Marshall et al. (1997), which solves the primitive Boussinesq form of the Navier-Stokes equations on an Arakawa staggered C-grid (Arakawa and Lamb 1977). The MITgcm is useful for modeling buoyant plumes due to its non-hydrostatic capabilities (Marshall et al. 1998), and has been used to simulate non-hydrostatic dynamics in glacier environments (Xu et al. 2012, 2013; Sciascia et al. 2013, 2014; Gladish et al. 2015; Cowton et al. 2015; Slater et al. 2015).

a. MITgcm Configuration

We use the MITgcm to investigate the sensitivity of near-glacier and downstream plumes to variations in horizontal eddy diffusivity (κ_H), subglacial discharge (Q_{sg}), and the number of subglacial conduits (Table 1).

Name	Conduit	dx/dy (m)	Q_{sg} (m^3 s^{-1})	κ_H (m^4 s^{-1})
pntSENS1	1x point	10	10, 75, 150, 300, 500, 750	0.125
pntSENS2	1x point	10	10, 75, 150, 300, 500, 750	0.25
pntSENS3	1x point	10	10, 75, 150, 300, 500, 750	0.5
pntPLM3	3x point	10	10	0.25
pntPLM5	5x point	10	10	0.25
pntPLM10	10x point	10	10	0.25
linePLM	Line source	10	10, 75, 150	0.25

TABLE 1. List of MITgcm simulations (see section 3 for details).

We define downstream as oriented in the direction of the outflowing plume (i.e., away from the ice face in the along-fjord direction). The model domain is an idealized

representation based on Rink Fjord, with a length of 100 km and depth of 850 m. The along-fjord horizontal resolution (Δx) is 10 m within 1 km of the terminus, telescoping to 10 km at the open western boundary (fjord mouth). A fjord width of 1 km is used, with a uniform across-fjord resolution (Δy) of 10 m and periodic lateral boundary conditions. For the range of Q_{sg} tested, the fjord width was adequate to prevent the plume from reaching the lateral boundaries in the near-glacier field. A uniform vertical resolution (Δz) of 10 m with 85 levels was used. Temperature and salinity are restored to the prescribed initial conditions at the open western boundary, which includes a 50 km restoration region to prevent internal waves reflecting back into the near-glacier field.

Near the glacier, the internal Rossby radius of deformation is larger than the fjord width and we assume that rotational effects have a second-order effect (i.e., f is set to zero in the model simulations). The equation of state (JMD95Z) follows Jackett and Mcdougall (1995). The model has a non-linear free surface and no-slip conditions enforced at the seabed and ice face. Additional simulations with a free-slip condition on the ice face resulted in slightly fresher plumes with larger vertical velocities near the grounding line. Bottom drag is parameterized with a quadratic drag law coefficient $C_D = 2.5 \times 10^{-3}$. We use a volume-conserving "virtual" salt flux for the subglacial discharge, where the freshwater flux is implemented as a salt flux (Huang 1993; Sciascia et al. 2013) and has no associated mass flux in the continuity equation. The Rink Isbræ glacier terminus is represented as a 850 m deep solid boundary, with a uniform ice temperature of -2 °C. Submarine melting and freezing processes on the ice wall are parameterized with a system of equations that represent the conservation of heat and salt

combined with a linear equation for the freezing point of seawater (Hellmer and Olbers 1989; Holland and Jenkins 1999; Losch 2008; Xu et al. 2012).

We perform a range of experiments with subglacial discharge values of 10, 75, 150, 300, 500, and 750 m³ s⁻¹ injected at the grounding line. The subglacial discharge has a salinity of 0 psu with temperature set to the salinity-pressure dependent freezing point at the grounding line depth (-0.628 °C). The efflux velocity is linearly restored over a 1-day timescale to increase numerical stability.

The relative importance of buoyancy and inertial forces in a meltwater plume can be described by the Froude number (Syvitski 1989; Mugford and Dowdeswell 2011). The Froude number can also be written as a ratio of the Reynolds and Grashof number (Arakeri et al. 2000; Salcedo-Castro et al. 2011),

$$\text{Fr} = \frac{\text{Re}}{\text{Gr}^{1/2}} \tag{7}$$

The Reynolds number is defined as $Re = uh/v$, where u is the horizontal velocity in the subglacial conduit, h is the height of the subglacial conduit (30 m), and v is the kinematic viscosity of seawater. The Grashof number characterizes the buoyancy flux:

$$\text{Gr} = \frac{(\rho_a - \rho_0)gh^3}{\rho_0 v^2} \tag{8}$$

For our upper-bound Q_{sg} of 750 m³ s⁻¹, $\text{Re} \sim 2.5 \times 10^7$ at the subglacial conduit and $\text{Gr} \sim 7.3 \times 10^{15}$, ensuring a Fr < 1. Therefore, our simulations correspond to a plume regime dominated by buoyancy forces (i.e., the injected subglacial discharge does not result in a jet), allowing for comparison with the MTT56 model.

b. Parameterization of Turbulent Entrainment

Turbulent entrainment processes in the MITgcm are not resolved and are parameterized here by a constant eddy diffusivity and viscosity. Sciascia et al. (2013) demonstrated that for 10 m grid resolution, the choice of horizontal eddy diffusivity, κ_H, was critical to correctly represent the dynamics of a 2-D line plume modeled in MITgcm. The choice of κ_H determines the rate of turbulent entrainment, constraining the reduced gravity and terminal level of the plume. Xu et al. (2012) used a Laplacian vertical viscosity of 0.1 m^2 s^{-1} and a biharmonic κ_H of 300 m^4 s^{-1} for a horizontal grid resolution of 20 m. Finer-scale models have used a Laplacian κ_H of 0.25 m^2 s^{-1} (Sciascia et al. 2013, 2014) and 0.01 m^2 s^{-1} (Xu et al. 2013) for 10 m and 1 m grid resolution, respectively.

For our experiments, we vary a biharmonic κ_H to evaluate the sensitivity of the downstream plume to this parameter. The horizontal eddy diffusivity and viscosity are set to be equal and range from 0.125, 0.25, and 0.5 m^4 s^{-1}. The eddy diffusivities are chosen to be large enough to suppress numerical instabilities, yet small enough to allow the model to reproduce sharp gradients and eddies. Following Sciascia et al. (2013), we use a constant Laplacian vertical eddy viscosity of 10^{-3} m^2 s^{-1}. A 3rd order, direct-space-time flux-limited advection scheme is used to increase the accuracy of the plume front and eliminate extrema in the tracer field. The simulations are integrated for 5 days, which is sufficient time for the plume to span the 1 km, 10 m resolution subdomain.

c. Conduit Geometry and Plume Interaction

To simulate 3–D point source plumes, subglacial discharge is injected horizontally into the fjord through a single 30 m x 30 m conduit at the grounding line depth. Additionally, we simulate a line plume and multiple point sources to evaluate how

subglacial conduit spacing affects the downstream properties of the plume in a 3-D

domain. For the line plume, subglacial discharge is injected uniformly as a buoyancy

source across the entire width of the glacier through a 1000 m x 30 m conduit at the

grounding line depth with an efflux velocity of 3.33×10^{-4} m s^{-1}. To investigate the

transition between coalescing point source and line plume regimes, we perform

experiments with multiple 30 m x 30 m conduits at 100, 200, and 400 m spacing

distributed across the 1 km glacier width (10, 5, and 3 conduits). The efflux velocities for

the 100, 200, and 400 m conduit spacing are 1.11×10^{-3} m s^{-1}, 2.2×10^{-3} m s^{-1}, and

3.7×10^{-3} m s^{-1}, respectively.

4. Results

a. Extended MTT56 Experiments

Numerically integrating the MTT56 governing equations with the continuous

stratification profile from Rink Fjord gives solutions for the vertical structure of volume,

momentum, and buoyancy flux (Figure 3). The theory predicts a range of surface and

subsurface plumes with ambient stratification representative of summer. For $Q_{sg} = 75$

and 150 m^3 s^{-1}, the plumes reach maximum height in the PW and SW layers (< 50 m).

The lower-bound Q_{sg} of 1 m^3 s^{-1} results in a subsurface plume that reaches to a maximum

height of 400 m. For $Q_{sg} = 300$ m^3 s^{-1}, the plume penetrates the meltwater pycnocline and

reaches the free surface (Figure 3b); however, the level of neutral buoyancy remains near

100 m within the PW region.

For maximum $Q_{sg} = 750$ m^3 s^{-1}, the level of neutral buoyancy reaches the free

surface and the plume becomes surface-trapped (not shown). During the initial plume

rise, the buoyancy flux is nearly constant due to the vertical homogeneity of the AW

properties near the grounding line depth where the fluid is very weakly stratified (Figure 3c).
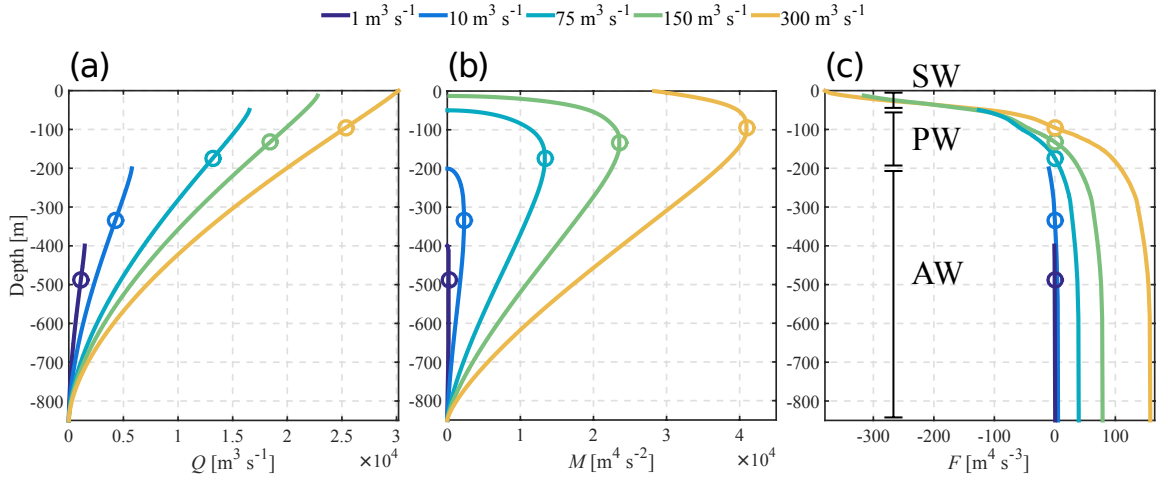
FIG. 3. (a) Plume volume, (b) momentum, and (c) buoyancy flux from the extended MTT56 model with an entrainment constant a of 0.13. Subglacial discharge fluxes of 1, 10, 75, 150, and 300m^3 s^{-1} are prescribed. Ambient stratification is the mean $N(z)$ synoptic summer profile from Rink Fjord. Circles represent the level of neutral buoyancy ($F = 0$).

Once the plumes rise ~250 m above the grounding line depth, stratification increases as the ambient density begins to decrease (Figure 2) as does the buoyancy flux. At the level of neutral buoyancy, the plume's buoyancy flux crosses zero and the plume becomes negatively buoyant. The plume gradually loses its vertical momentum as it continues to rise through the AW and PW layers (Figure 3b). For $Q_{sg} < 75$ m^3 s^{-1}, the level of neutral buoyancy is reached well below the ~50 m deep SW layer (Figure 3c). For $Q_{sg} \geq 75$ m^3 s^{-1}, the plume's residual vertical momentum allows for penetration into near-surface depths. Downstream of the glacier terminus, the terminal level of the plume should be bounded by the maximum height and the level of neutral buoyancy.

b. MITgcm Experiments

For the 3-D MITgcm point source simulations, the discharge of buoyant meltwater at the grounding line results in a turbulent plume that rises vertically along the glacier terminus. The plumes remain attached to the vertical glacier terminus until they reach their maximum height, at which point they separate and flow horizontally away from the ice face (Figure 4).
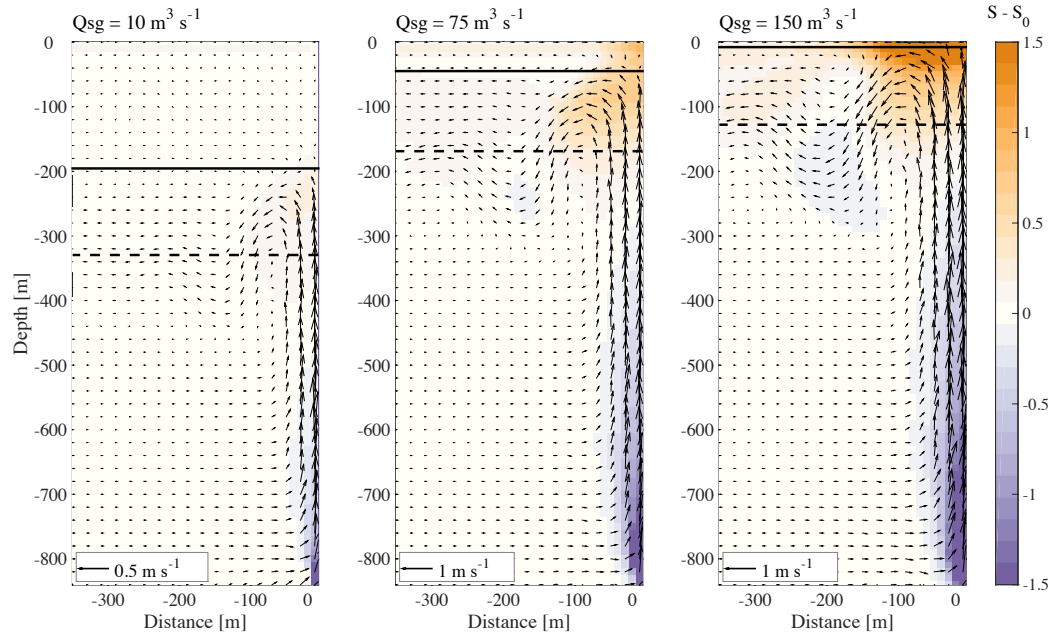
FIG. 4. Cross-section view of near-glacier salinity anomaly for subglacial discharge fluxes of 10, 75, and 150 m^3 s^{-1}; black arrows represent velocity vectors. The cross section is taken at the plume centerline; tracer and velocity fields are averaged over a 3-day period. Salinity anomaly is the difference between the 3-day mean and initial conditions. A horizontal eddy diffusivity of 0.5 m^4 s^{-1} is prescribed. The solid black line represents the MTT56 maximum plume height ($M = 0$); the dashed black line is the level of neutral buoyancy ($F = 0$).

Note that we use the term "plume" to describe the both vertical plumes rising along the ice face and horizontal buoyancy-driven currents that flow away from the glacier as

surface gravity currents or subsurface intrusions. As the plumes rise, they entrain dense

ambient fluid, increasing the volume flux and expanding radially (Figures 4 and 5).
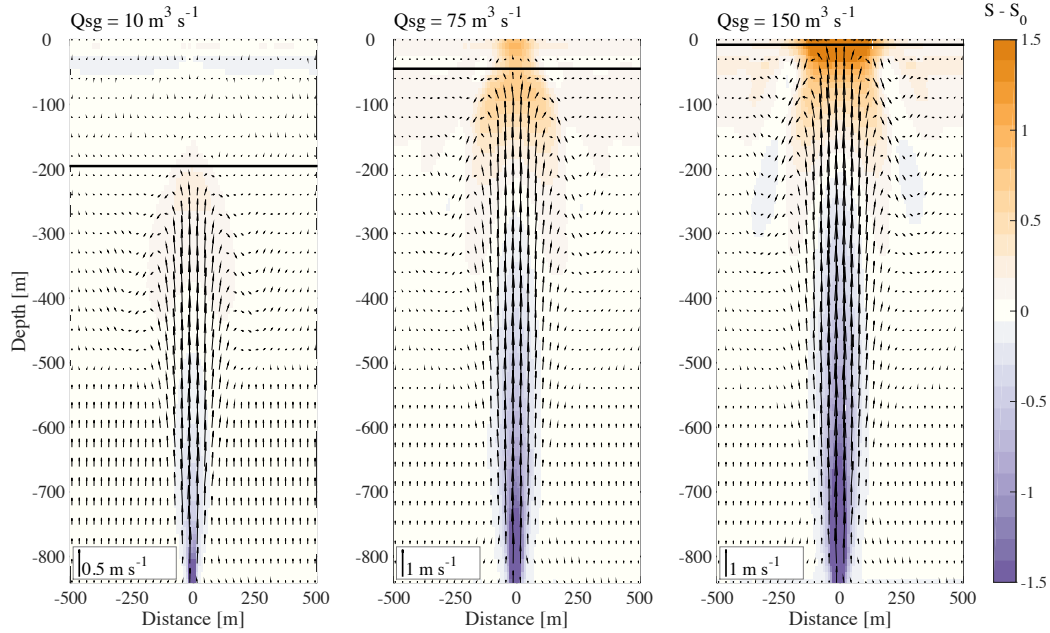
FIG. 5. Ice face view of near-glacier salinity anomaly for subglacial discharge fluxes of 10, 75, and 150 m^3 s^{-1}, black arrows represent velocity vectors. Tracer and velocity fields are averaged over a 3-day period. The salinity anomaly is defined as the difference between the 3-day mean and the initial conditions. A horizontal eddy diffusivity of 0.5 m^4 s^{-1} is prescribed. The black line represents the MTT56 maximum plume height ($M = 0$).

The initial dilution of the plume is determined by the rate of subglacial discharge and the

choice of horizontal eddy diffusivity/viscosity. The salinity of the plume in the first wet

cell adjacent to the subglacial conduit is 32.98 and 25.46 for a Q_{sg} of 10 and 150 m^3 s^{-1},

corresponding to a reduced gravity g′ of 0.01 and 0.07 m s^{-2}, respectively. The reduced

gravity for pure meltwater at the grounding line is 0.22 m s^{-2}, demonstrating that the

plume is quickly diluted with entrained AW as it exits the subglacial conduit. The model

simulations are in good agreement with the MTT56 level of neutral buoyancy and

maximum height, implying that the MITgcm bulk plume properties are consistent with

theory. The simulations also reproduce the inertial overshoot that is evident in the MTT56 solutions. The inertial overshoot occurs uniformly in the radial direction, constrained only by the vertical glacier terminus. For large subglacial discharges, the horizontal length scale for a turbulent plume to transition into a steady outflow can exceed 500 m (Figure 6a). We note that for our largest Q_{sg} of 750 m^3 s^{-1}, the plume did not exhibit an inertial overshoot and remained surface-trapped (not shown).

At 1 km downstream, the terminal level of the outflowing plumes are centered near the MTT56 level of neutral buoyancy (Figure 6a,b). A Q_{sg} of 10 m^3 s^{-1} results in a weak outflow, with a maximum horizontal plume velocity of 0.04 m s^{-1} 1 km downstream of the terminus (Figure 6b). A Q_{sg} of 300 m^3 s^{-1} results in a faster-flowing plume, with a maximum downstream horizontal velocity of 0.20 m s^{-1} (Figure 6b). For $Q_{sg} < 150$ m^3 s^{-1}, submarine melting along the glacier terminus results in a weak inflow/outflow below the terminal level of the discharge-driven plume. This small-scale structure is amplified and biased towards inflow as subglacial discharge is increased. The relatively slow downstream plume velocities provide a sharp contrast to the large vertical velocities at the glacier terminus, which are on the order of meters per second. Our results also highlight the importance of the seasonal SW layer in bounding the terminal level of the plume. For large subglacial discharges, vertical momentum enables the plume to penetrate through the stratification maximum at the PW-SW interface. However, for Q_{sg} < 750 m^3 s^{-1}, the level of neutral buoyancy is bounded by the SW layer – resulting in a plume that reaches the free surface at the ice face and is trapped underneath buoyant SW as it flows away from the glacier.
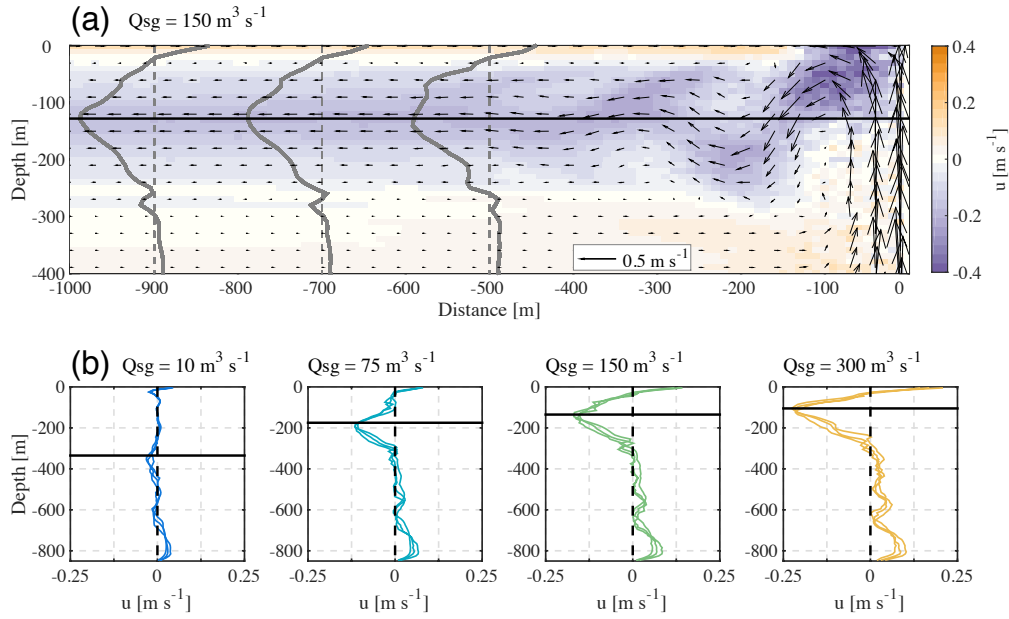
FIG. 6. (a) Cross-section view of mean horizontal velocity for a subglacial discharge flux of 150 m^3 s^{-1}; black arrows represent velocity vectors. The black line is the MTT56 level of neutral buoyancy. Mean horizontal velocity profiles are shown at 500, 700, and 900m downstream of the glacier. The cross section is taken at the plume centerline; velocity fields are averaged over a 3-day period. A horizontal eddy diffusivity of 0.5 m^4 s^{-1} is prescribed. (b) Horizontal velocity profiles taken 1 km downstream of the glacier for all point source simulations; the solid black line is the MTT56 level of neutral buoyancy (F = 0).

A comparison of plume water properties at the glacier terminus and 1 km downstream is shown in Figure 7. At the glacier terminus, the θ-S properties of the plume fall along the runoff mixing line, indicating the mixing of fresh subglacial discharge with the deep AW layer. For both low and high subglacial discharge fluxes, the near-glacier and downstream water properties are bounded by the runoff and melt lines. The heat required to melt ice combined with the mixing of meltwater with ambient fluid results in a melt line in θ-S space, with a so called "Gade slope",

$$\frac{\partial T}{\partial S} = \frac{1}{S}\left[\frac{L}{C_p} - \frac{C_i}{C_p}(T_i - T_f) - (T_f - T)\right],\qquad(9)$$

where T is temperature, S is salinity, L is the latent heat of fusion for ice, C_i and C_p are specific heat capacities of ice/water, T_i is the temperature of ice, and T_f is the freezing point temperature (Gade 1979; Jenkins 1999; Mortensen et al. 2013). For the low discharge case of 10 m^3 s^{-1}, the SW layer is more buoyant than the initial dilution of the plume as it exits the subglacial conduit (Figure 7a). Compared to the initial θ-S conditions, the profile 1 km from the glacier shows warming and a slight increase of salinity at depth, indicating the influence of glacially modified AW from the plume (Figure 7b).
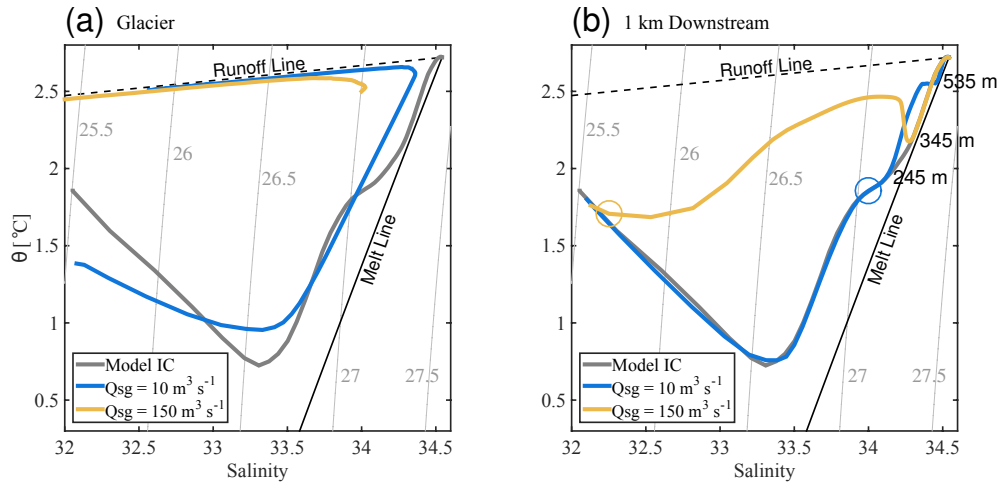
FIG. 7. (a) Potential temperature–salinity profiles at the glacier terminus and (b) 1 km downstream for point source plumes with a subglacial discharge flux of 10 and 150 m^3 s^{-1}. The gray profile represents the initial model conditions. Solid black and dashed lines represent mixing due to glacial melt (melt line) and subglacial discharge (runoff line), respectively. The starting point of the mixing lines is set to ambient water at the grounding line depth. Circles represent the maximum height from the MTT56 model projected on the downstream profile.

Compared to the low discharge case, a high discharge of 150 m^3 s^{-1} exhibits drastically different downstream θ-S properties and ambient water mass modification. At this Q_{sg}, the plume reaches a maximum height at ~5 m below the free surface, encompassing the entire water column at the glacier terminus. The dynamics of the fjord are determined by the large subglacial discharge flux, with submarine melting having a second order effect. As it rises, the plume vigorously entrains heat and salt into the PW/SW layers, increasing the temperature and salinity of the upper water column.

c. MITgcm Sensitivity Analysis

Both the vertical velocity and maximum height of the plume at the glacier terminus are robust to the tested range of κ_H (Figure 8).
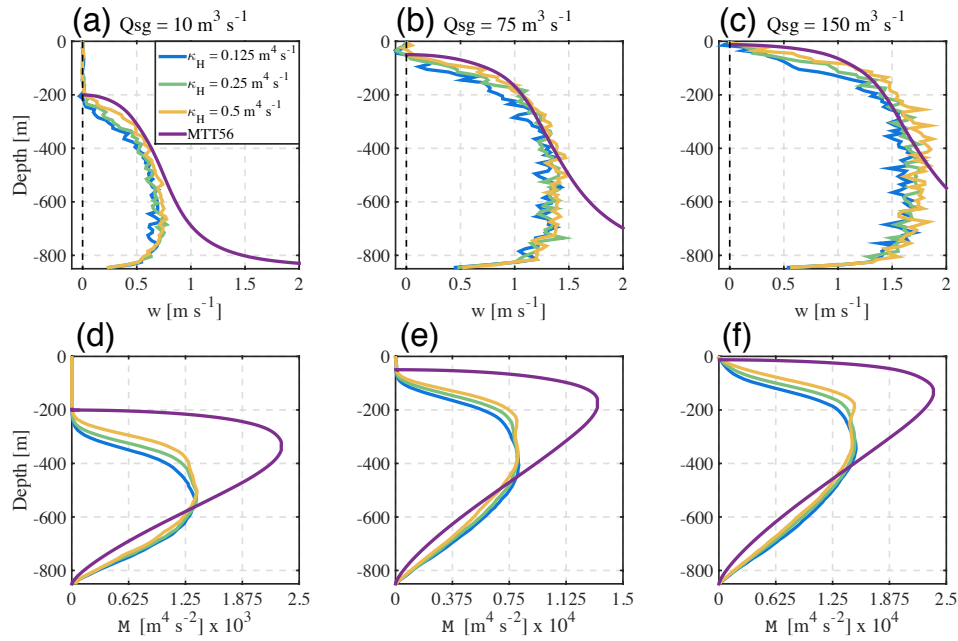
FIG. 8. Mean centerline vertical velocities at the glacier terminus for subglacial discharge fluxes of (a) 10, (b) 75, and (c) 150 m^3 m^{-1}. (d),(e),(f) The corresponding momentum fluxes. Note the different scales used in the momentum fluxes. Horizontal eddy diffusivities are varied from 0.125 to 0.5 m^4 s^{-1}. Velocities are averaged over a 3-day period. Purple profiles represent the MTT56 solutions.

An increase of κ_H by a factor of two results in slightly increased vertical velocities (<10%) and turbulent entrainment. For a κ_H of 0.25 m^4 s^{-1}, a subglacial discharge flux of 10 m^3 s^{-1} results in a maximum vertical velocity of 0.78 m s^{-1} (Figure 8a). Subglacial discharge fluxes of 75 and 150 m^3 s^{-1} produce a more vigorous plume, with a maximum vertical velocity of 1.46 and 1.79 m s^{-1}, respectively (Figure 8b,c). Away from the grounding line depth, the MITgcm vertical velocities agree well with the MTT56 solutions (Figure 8a,b,c). At the grounding line, the MTT56 vertical velocities asymptote to infinity due to the zero volume flux ($Q = 0$) boundary condition. The corresponding MITgcm momentum fluxes (Figure 8d,e,f) are within a factor of two of the MTT56 solutions, with the largest discrepancies occurring at mid-column depths.

Volume transports (Q_{out} and Q_{in}), binned by salinity class, indicate the shift in entrainment between model runs (Figure 9a). Positive transports indicate flow towards the glacier terminus; negative values represent the outflowing plume. For all simulations, the net flow across the open boundaries is balanced (i.e., $Q_{out} = Q_{in}$). Volume transports are averaged between 900 m and 1 km downstream of the glacier and computed in salinity bins of 0.05. To provide an estimate of the bulk salinity of the in- and out-fjord transports, we compute volume weighted salinities as

$$\bar{S}_{in} = \iint_A (U_{in} S_{in})\, dA \Big/ \iint_A U_{in}\, dA \text{, and} \tag{10}$$

$$\bar{S}_{out} = \iint_A (U_{out} S_{out})\, dA \Big/ \iint_A U_{out}\, dA, \tag{11}$$

where u_{in} and u_{out} and S_{in} and S_{out} are the in and out-fjord velocities and salinities, respectively. A thin return flow of SW with a salinity of ~32.25 is present in all cases and is not included in the calculations. A subglacial discharge flux of 10 m^3 s^{-1} results in a

multi-cell circulation in the fjord (Figure 9a), with a deep cell driven by subglacial

discharge and a weaker upper- column cell driven by submarine melt.
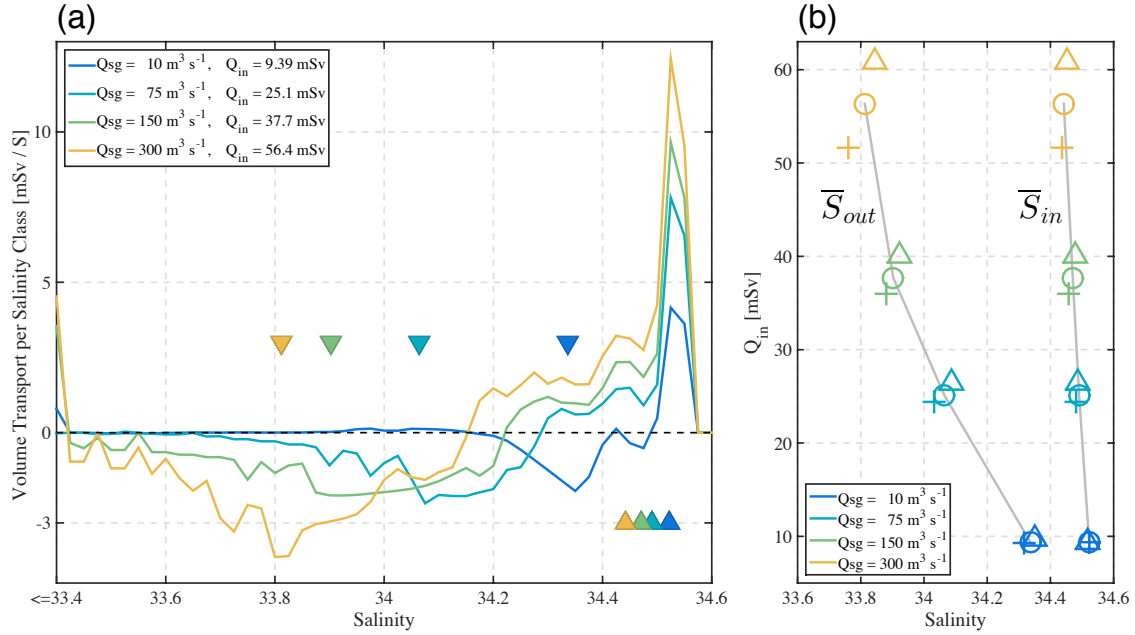
FIG. 9. (a) Downstream volume transport binned by salinity class for point source plumes with a subglacial discharge flux of 10, 75, 150, and 300 m^3 s^{-1}. Horizontal eddy diffusivity is 0.25 m^4 s^{-1}. The term Q_{in} is the integrated, cross-sectional volume transport toward the glacier. Downward-pointing triangles represent S_{out}; upward-pointing triangles are S_{in}. (b) Summary plot demonstrating the sensitivity of Q_{in} and S to subglacial discharge. Triangles, circles, and crosses represent a κ_H of 0.125, 0.25, and 0.5 m^4 s^{-1}, respectively.

For higher Q_{sg}, the circulation is primarily two-layer, with a single inflow and outflow.

An increase of κ_H results in a weaker, more viscous transport of AW toward the glacier

(Figure 9b). Increasing κ_H results in a slightly more diluted plume, shifting the

downstream outflow to lower salinity classes. For κ_H of 0.25 m^4 s^{-1}, this gives S_{in} =

34.52, 34.49, 34.47, and 34.44 for a corresponding subglacial discharge flux of 10, 75,

150, and 300 m^3 s^{-1}. The corresponding S_{out} values are 34.34, 34.06, 33.90, and 33.81.

d. Comparison of Line and Point Source Plumes

To investigate the role of subglacial conduit spacing on the downstream properties of the plume, we simulate multiple point source plumes spaced at 400, 200, and 100 m intervals across the glacier terminus (Figure 10). A Q_{sg} of 10 m^3 s^{-1} is used in these simulations. For a conduit spacing of 400 and 200 m, the plumes remain separated and interact weakly at their lateral boundaries (Figure 10a,b).
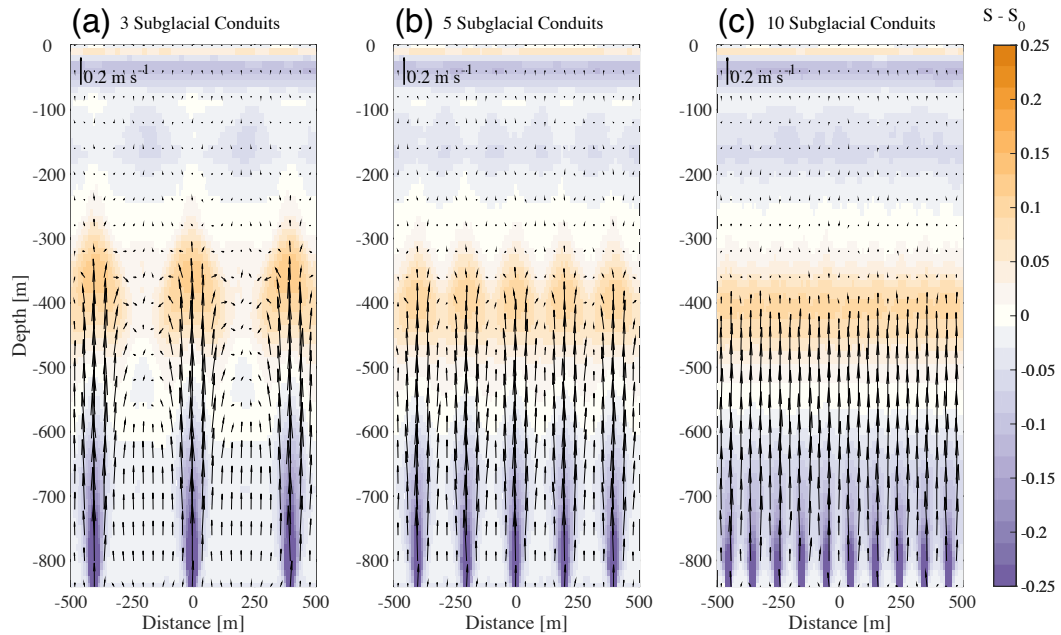
FIG. 10. Ice face view of near-glacier salinity anomaly for multiple point source plumes spaced uniformly at (a) 400-, (b) 200-, and (c) 100-m intervals across the glacier terminus; black arrows represent velocity vectors. Subglacial discharge is 10 m^3 s^{-1}; tracer and velocity fields are averaged over a 3-day period. Salinity anomaly is the difference between the 3-day mean and initial conditions. A horizontal eddy diffusivity of 0.25 m^4 s^{-1} is prescribed.

When the conduit spacing is reduced to 100 m, the plumes coalesce and begin to approximate a continuous line plume (Figure 10c). The distribution of the subglacial discharge through multiple conduits is modeled by a lower efflux velocity, decreasing the

vertical velocity of the plume. Volume transport binned by salinity class for one, three, five, and ten point source plumes and a continuous line plume is shown in Figure 11a.
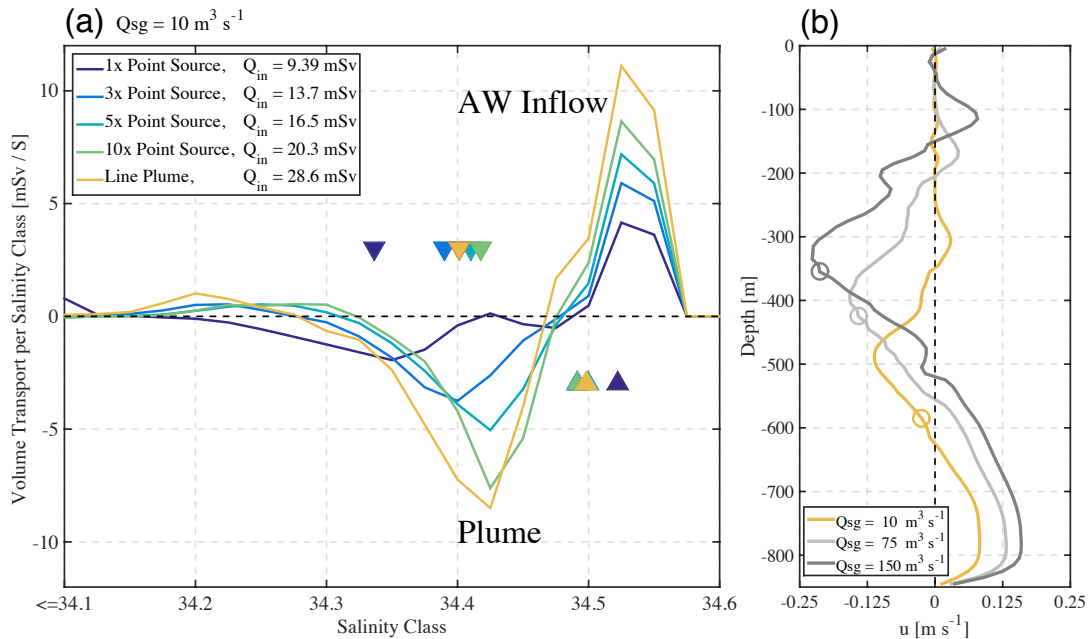
FIG. 11. (a) Downstream volume transport binned by salinity class for 1, 3, 5, and 10 point source plumes and a continuous line plume. The term Q_{in} is the integrated, cross-sectional volume transport toward the glacier. Downward-pointing triangles represent S_{out}; upward-pointing triangles are S_{in}. (b) Mean line plume horizontal velocity profiles taken 1 km downstream from the glacier terminus at the plume centerline. Velocity fields are averaged over a 3-day period. Circles represent the level of neutral buoyancy from Jenkins (2011).

For both line and point source plumes, the flux of subglacial discharge drives a multi-cell circulation in the fjord – with multiple inflow and outflows distributed across a range of salinity classes. The maximum positive volume transports are centered between salinity classes of 34.49-34.52, corresponding to the return flow of AW toward the glacier terminus. While the return flows fall within a similar range of salinity classes, the outflows vary depending on the terminal level and plume type (i.e., line or point source). The line plume strongly dilutes the subglacial discharge, resulting in a much larger Q_{in}

compared to the initial Q_{sg} and driving a vigorous buoyancy-driven circulation in the fjord. As the conduit spacing increases, the magnitude of volume transport decreases, reaching a minimum in the case with a single subglacial conduit. Line plumes with subglacial discharge fluxes of 10–150 m^3 s^{-1} result in deep outflows centered at depths > 300 m (Figure 11b).

5. Discussion

The 3-D MITgcm plume simulations presented here are in good agreement with the extended MTT56 model, demonstrating that ocean GCMs can capture the bulk properties of a point source plume based on similarity theory. While the MTT56 model provides a useful tool for exploring the range of plume regimes that exist across outlet glacier parameter space (i.e., subsurface vs. surface-trapped), 3-D models such as the MITgcm are essential to capture the fjord-scale circulation and spatial distribution of submarine melt across the ice face – which has important consequences for grounding line stability and glacial undercutting. The application of the MTT56 model to estimate submarine melt rates is limited, particularly in shallow fjords, due to the vertical velocity tending to infinity at the grounding line. A point source formulation of more complex models such as Jenkins (2011), where the initial vertical velocity is prescribed by assuming a balance between buoyancy and frictional drag, would provide a computationally efficient tool for estimating melt rates in systems with discrete subglacial conduits. We find that the use of realistic stratification profiles and a reasonable choice of horizontal eddy diffusivity are critical to represent the bulk dynamics of the plume, consistent with the results of previous modeling studies (Sciascia et al. 2013; Kimura et al. 2014). We note that the MTT56 model is only valid for a

summer regime, where plume dynamics are dominated by subglacial discharge and submarine melting has a second-order effect. The downstream outflow depths of the modeled line plumes are biased high compared to the level of neutral buoyancy calculated using the model from Jenkins (2011). This bias is reduced as the discharge rate is increased (Figure 11b).

Our study demonstrates that the terminal level and water properties of meltwater plumes can vary dramatically with increasing distance from the glacier terminus. The presence of strong stratification can result in plumes that reach the free surface in the near-glacier field and then transition into subsurface intrusions at roughly the level of neutral buoyancy downstream (Figure 6). After the initial overshoot of the plume, several dampened vertical oscillations about the level of neutral buoyancy occur, which act to further mix ambient fluid into the plume and modify water properties as the plume flows away from the ice face. In this region, the plume behaves as a fountain, consisting of a turbulent shear flow driven by upward vertical momentum with an opposing negative buoyancy flux (Turner 1966; Ansong et al. 2008; Kaye 2008). We note that the use of a constant eddy diffusivity does not allow for representation of internal wave or shear-driven mixing, which may be important in this region.

To investigate a wider range of subglacial discharge fluxes and stratification profiles, we use the extended MTT56 model to explore plume outflow depth in GrIS outlet glacier fjord parameter space (Figure 12). MTT56 was run with both constant N (Figure 12a) and idealized stratification profiles with varied pycnocline depths (Figure 12c), representing a range of seasonal stratification profiles in a typical GrIS fjord.
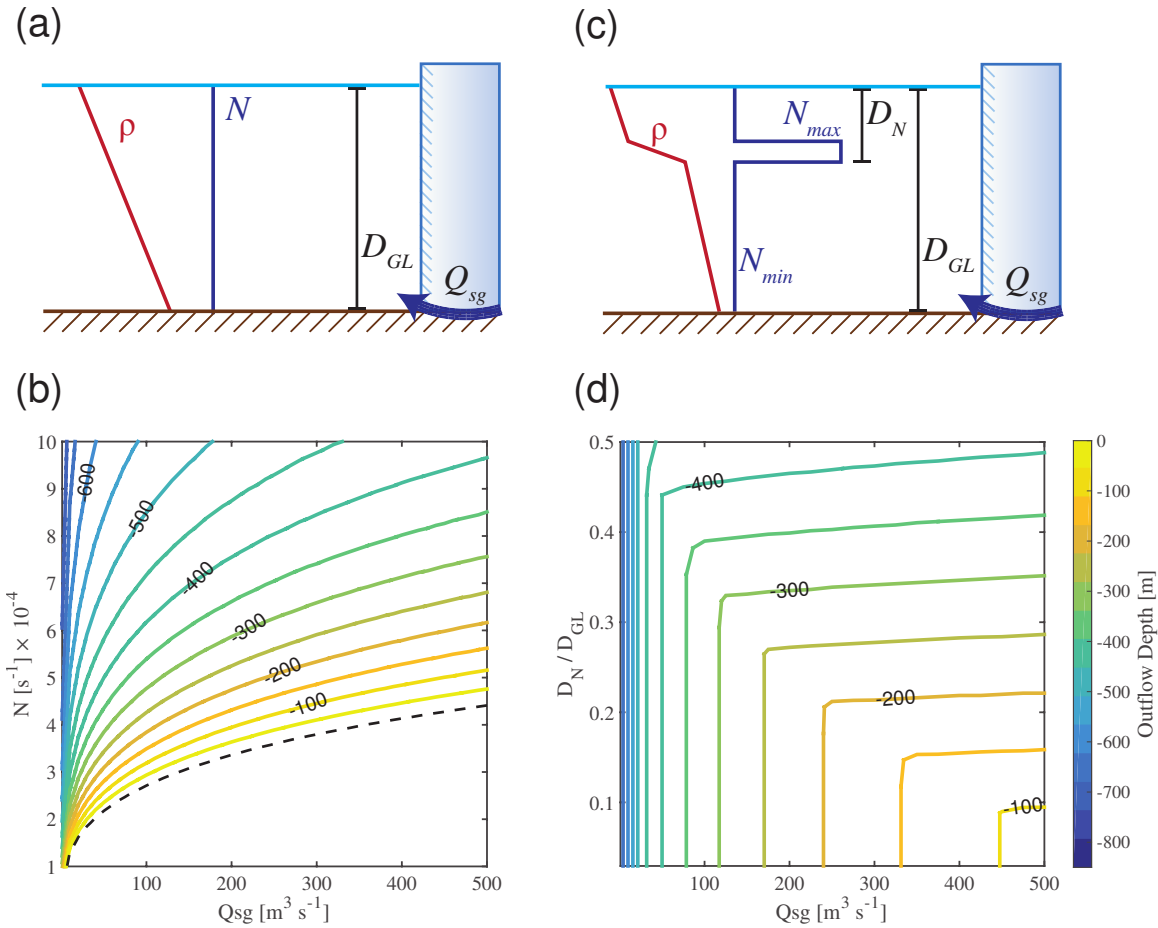
FIG. 12. (a) Idealized representation of density and buoyancy frequency profiles for fjords with constant stratification. (b) Plume outflow depth, defined as the level of neutral buoyancy from the MTT56 model, as a function of constant stratification and subglacial discharge. Dashed black line represents the free surface. (c) Idealized representation of density and buoyancy frequency profiles for fjords with a two-layer stratification. (d) Outflow depth for a range of pycnocline depths D_N and subglacial discharges. For each run, N_{max} is 0.02 s^{-1} and N$_{min}$ is 0.005 s^{-1}. In all cases, the grounding line depth D_{GL} is set to 850 m.

For constant $N < 3 \times 10^{-4}$ s^{-1} and Qsg > 150 m^3 s^{-1}, the level of neutral buoyancy reaches the free surface and the plumes become surface-trapped (Figure 12b). A pycnocline with N_{max} of 0.02 s^{-1} bounds the level of neutral buoyancy at depth for the entire range of Q_{sg} tested, resulting in subsurface outflows (Figure 12d). Subglacial discharge of meltwater into strongly stratified outlet glacier fjords with deep grounding

lines results in subsurface outflows – for shallow fjords with weaker stratification, we would expect plumes to be surface-trapped.

During winter, stratification likely decreases near the surface due to the lack of SW. However, plumes may still be trapped at depth due to the seasonal reduction of Q_{sg}. For our 3-D point source simulations, low subglacial discharge results in a multi-cell circulation in the vertical (Figure 6), consistent with observational results from Sermilik Fjord, east Greenland (Straneo et al. 2011; Sutherland and Straneo 2012). Sciascia et al. (2013) showed that for low subglacial discharge fluxes in a two-layer stratification, large amounts of relatively fresh glacially modified water can be exported at depth at the AW-PW interface. Our results indicate that large discharges of meltwater in deep, strongly stratified fjords can result in plume outflows with positive temperature and salinity anomalies (Figures 4,5). In this flow regime, turbulent entrainment along the glacier terminus acts as a mechanism to vertically transport heat and salt upwards in the water column. These results are in agreement with recent fjord-scale models (Cowton et al. 2015) and hydrographic observations from Godthåbsfjord, west Greenland (Kjeldsen et al. 2014). During ice-dammed lake drainage events, large amounts of warm, saline water were brought to the near-surface layers, indicating turbulent entrainment of AW at the glacier terminus. Warm plumes may result in increased submarine melting of icebergs and sea ice, resulting in a weakening of ice mélange and additional fluxes of freshwater to the ambient stratification.

This study also demonstrates the importance of having *a priori* knowledge of the subglacial hydrology and conduit/ice face geometry. With constraints on fjord stratification, grounding line depth, and conduit geometry, our results suggest that plume

33

properties could be used to provide a back-of-the-envelope calculation of subglacial discharge rates – which are difficult to measure in-situ. During summer conditions, variability in surface ablation results in a time-evolving network of subglacial conduits (Cowton et al. 2013), which could lead to a wide range of line and point source plumes rising along the glacier terminus. Previous laboratory and modeling results have shown that when two point source conduits are within close proximity to each other, separate axisymmetric plumes can coalesce into a single plume (Kaye and Linden 2004; Cenedese and Linden 2014). Our simulations with multiple conduits agree with recent studies by Kimura et al. (2014) and Slater et al. (2015), demonstrating that narrow conduit spacing in deep fjords can result in coalescing plumes. In our simulations, coalescing point source and line plumes result in a more vigorous buoyancy-driven fjord circulation (Figure 11a). For the equivalent Q_{sg}, line plumes produce deeper, more diluted outflows than point source plumes. These results suggests that current 2-D models may overestimate the strength of the buoyancy-driven circulation in systems where subglacial discharge is injected through discrete conduits. The discharge of meltwater through a distributed system of subglacial conduits would result in weaker efflux velocities at the grounding line, decreasing the vertical velocity of the plumes. However, the increased surface area available for turbulent heat transfer to the glacier face may result in an net increase of melt across the entire glacier terminus, especially for wide glaciers. Recent results from Slater et al. (2015) demonstrate that subglacial hydrology has an important control on submarine melt rates, with the transition from a single conduit to a distributed system increasing melt by a factor of 5. Clearly, further studies are needed to assess the impact of ice face topography, channel shape, and plume regimes on submarine melt rates.

We note that these results rely on the simplified assumption of fixed boundary conditions at the fjord mouth, which provide a constant source of ocean heat in the AW layer. In Greenland, renewal of basin water may play an important role in the heat budget of fjords with sills. Observations from Godthåbsfjord show that dense inflows contribute to the basin water, lasting 1-3 months, with warm inflows related to pulses in the AW content of the West Greenland Current (Mortensen et al. 2011, 2013). It is unclear if this renewal process is ubiquitous across other Greenland outlet glacier fjords; however, preliminary results from Ilulissat Icefjord suggest that renewal occurs over the shallow sill and toward Jakobshavn Glacier (Gladish et al. 2015).

Dynamics other than buoyancy-driven flows – tides, katabatic winds, and intermediary circulation (Straneo et al. 2010; Jackson et al. 2014; Sciascia et al. 2014; Sutherland et al. 2014) – may also be critical to heat transport and renewal of water in the fjords. Other limitations of our model include the highly idealized model domain. Many Greenlandic fjords, including Rink, have one or multiple sills, which may strongly constrain the plume-driven circulation and the return flow of AW toward the glacier. The neglected rotational effects and cross-fjord circulation may be important further downstream of the glacier where the fjord width widens to ~15 km. Additionally, the use of a constant eddy diffusivity does not represent the full range of mixing processes in the overshoot region, which may result in deeper outflows than an eddy-resolving simulation.

6. Conclusions

Greenland's fjords couple the ice sheet margins to the continental shelf, forming the boundary between the accelerating GrIS and the coastal ocean. We use buoyant plume

theory and non- hydrostatic, three-dimensional MITgcm simulations to investigate how meltwater plume dynamics and the resultant fjord-scale circulation depend on subglacial discharge, ambient stratification, turbulent diffusivity, and subglacial conduit geometry. While classic plume theory provides a useful estimate of the plume's outflow depth, 3-D ocean-ice models are needed to resolve the fjord-scale circulation and spatial distribution of submarine melting along the ice face. Plumes with large vertical velocities penetrate to the free surface near the ice face; however, subsurface stratification maxima can create a barrier that can trap plumes at depth as they flow away from the glacier. Large subglacial discharges result in vigorous turbulent entrainment of bottom water, transporting heat and salt upwards in the water column and producing warm, salty outflows. We find that fjord-scale circulation is highly sensitive to subglacial conduit geometry; multiple point source and line plumes result in stronger return flows of Atlantic water toward the ice face. Our results indicate the need for further observations that constrain the heat and salt budgets between GrIS outlet glacier fjords and the coastal ocean. In-situ measurements of turbulent dissipation rates and velocity/tracer profiles in the near-glacier plume are critical.

7. Bridge

In Chapter II, I used buoyant plume theory and a nonhydrostatic, three-dimensional ocean–ice model to investigate near-glacier plume dynamics. To extend these results across Greenland, in Chapter III, I use buoyant plume theory, initialized with realistic ranges of subglacial discharge, glacier depth, and ocean stratification, to investigate how simulated plume structure and submarine melt vary during summer months in 12 Greenland fjords.

THE IMPACT OF GLACIER GEOMETRY ON MELTWATER PLUME STRUCTURE AND SUBMARINE MELT IN GREENLAND FJORDS

This chapter was published in *Geophysical Research Letters* in October 2016. I was lead author on the paper, developing the methodology, analyzing the data, and writing the manuscript. David Sutherland (University of Oregon) served as advisor, aiding in data interpretation and manuscript editing. Ben Hudson (University of Washington) contributed probability-based glacier catchments. Brice Noël (Utrecht University) and Michiel van den Broeke (Utrecht University) provided estimates of runoff from the Regional Atmospheric Climate Model. Twila Moon (University of Bristol), Emily Shroyer (Oregon State University), Jonathan Nash (Oregon State University), Ginny Catania (University of Texas in Austin), Tim Bartholomaus (University of Idaho), Denis Felikson (University of Texas in Austin), and Leigh Stearns (University of Kansas) provided feedback on manuscript drafts and aided in manuscript editing.

1. Introduction

Mass loss from the Greenland Ice Sheet quadrupled from 1992-2011 [Shepherd et al., 2012]. The acceleration, retreat, and thinning of outlet glaciers [van den Broeke et al., 2009; Enderlin et al., 2014] coincided with a warming of Atlantic waters [Straneo and Heimbach, 2013], leading to the hypothesis that marine-terminating glaciers are sensitive to ocean forcing [Vieli and Nick, 2011]. On the Greenland shelf, warm, salty Atlantic Water is typically found at depth, overlaid by cold, fresh Polar Water and a seasonal layer of warm Surface Water [Straneo et al., 2012]. Warming of subsurface Atlantic waters in

Greenland fjords can lead to increased submarine melting [Holland et al., 2008; Motyka et. al., 2011], which has been implicated as a mechanism for promoting calving [O'Leary and Christoffersen, 2013; Luckman et al., 2015] and accelerating glacier flow [Nick et al., 2009].

Submarine melting is determined by the net ocean heat flux to the ocean-ice boundary layer through processes that are highly dependent on fjord circulation [Straneo et al., 2010, 2011, 2012]. Previous work shows that there is large regional and temporal variability in fjord circulation. For example, southeast Greenland fjords are forced by subglacial plumes during summer [Straneo et al., 2011] and dominated by shelf-forced flows during winter [Jackson et al., 2014; Jackson and Straneo, 2016]. Subglacial plumes are a primary feature of west Greenland fjords during summer [Mortensen et al., 2013; Chauché et al., 2014; Bartholomaus et al., 2016], and may be relatively more important year-round compared to southeast Greenland due to the lack of strong shelf-forced flows. Given uncertainty in the relative importance of shelf-forced circulation across Greenland, it is first necessary to characterize subglacial plumes – the most commonly observed feature thought to be dominantly responsible for terminus melt and fjord circulation during the meltwater season [Straneo and Cenedese, 2015].

Our understanding of how subglacial plumes vary across Greenland fjords is, however, severely limited. Direct observations of plumes are sparse due to the difficult working conditions at calving termini [Stevens et al., 2016]. Recent work tracing the pathways of glacially modified water suggests heterogeneity in plume properties, with shallow glaciers unable to entrain deep reservoirs of Atlantic-origin water [Beaird et al., 2015]. Previous theoretical results [Jenkins et al., 2011; Slater et al., 2016] and numerical

ocean models [Xu et al., 2012,2013; Sciascia et al., 2013; Cowton et al., 2015; Slater et al., 2015; Carroll et al., 2015] have provided key insight into plume dynamics at glacier termini. However, no systematic set of sensitivity experiments has been conducted to show how subglacial plumes and submarine melt rates in Greenland fjords vary over the broad range of observed oceanographic stratification profiles, with all of the environmental complexities that this entails.

Here we use a buoyant plume model [Cowton et al., 2015] paired with shipboard hydrographic observations to characterize subglacial plumes and submarine melt in 12 major Greenland fjords (Figure 1 and Table 1).

Glacier	GL (m)	Ocean T (°C)	OHC (GJ m^{-2})	Hydrographic Data
Upernavik 4 (UP4)	100	1.35 ± 0.11	1.68 ± 0.07	2013[b] and 2015
Umiamako (UMI)	230	1.56 ± 0.01	3.38 ± 0.05	2013
Kangerdlugssup Sermerssua (KS)	250	1.12 ± 0.16	2.86 ± 0.13	2013–2015
Kangiata Nunata Sermia (KNS)	250	1.80 ± 0.45	3.85 ± 0.65	2006, 2007[b]–2009, and 2011–2013
Heilprin (HP)	350	0.64 ± 0.01	2.03 ± 0.15	2003
Store (ST)	500	2.07	7.19	2010[b]
Tracy (TR)	610	0.73 ± 0.01	3.85 ± 0.21	2003
Helheim (HG)	650	2.70 ± 0.44	15.3 ± 2.29	2008–2012
Kangerdlugssuaq (KG)	650	0.80 ± 0.18	5.07 ± 0.68	1993, 2004, 2009, and 2012
Jakobshavn (JI)	800	2.43 ± 0.01	17.1 ± 0.11	2009
Alison (AL)	850	1.17	9.34	2014[b]
Rink Isbræ (RI)	850	2.32 ± 0.07	16.5 ± 0.74	2013–2015

[a]The errors in ocean temperature and heat content represent the uncertainty (1 standard deviation) due to temporal and spatial variability in fjord stratification. Supporting information contains additional details on grounding line depth and hydrographic data sources.
[b]Single CTD cast is denoted.

Table 1. Mean grounding line depth (GL), mean depth-averaged ocean temperature (Ocean T), mean ocean heat content (OHC), and summer hydrographic data coverage for all modeled systems (* denotes single cast). Errors in ocean temperature and heat content represents uncertainty (one standard deviation) due to temporal and spatial variability in fjord stratification. Supporting information contains additional details on grounding line depth and hydrographic data sources.

We show that systematic differences in modeled plume circulation at mean summer discharge levels are due to variability in grounding line depth and fjord hydrography, demonstrating that the coupled fjord-glacier system is responsible for modulating the

mixing of ice sheet runoff with seawater. While our analysis is limited to fjords with available hydrographic and bathymetric data, our study encompasses a greater range of observed summer ocean properties and grounding line depths than previously examined [Straneo et al., 2012] (Table 1 and Table S1; see Appendix A for all supplemental figures for this Chapter).
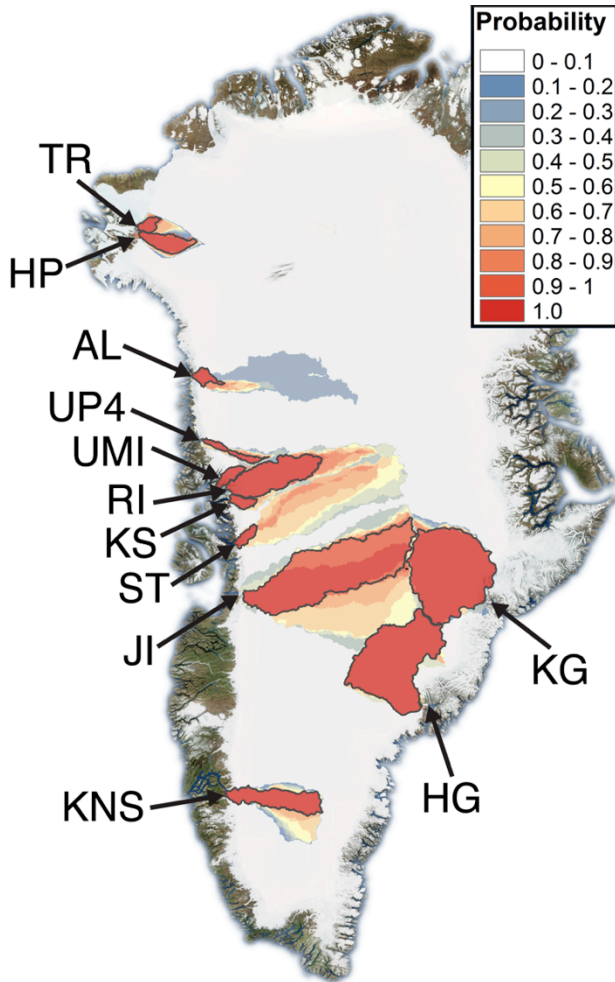
Figure 1. Greenland outlet glaciers examined in this study and their respective probability-based catchments. Colors show the probability that a region of the ice sheet contributes meltwater to the outlet glacier, grey boundaries represent the 95% probability level catchments used to estimate subglacial discharge.

We generate daily estimates of subglacial discharge for each glacier by pairing a probability-based algorithm for delineating ice sheet catchments with a high-resolution

model of surface runoff [Noël et al., 2015]. Finally, we utilize repeated hydrographic surveys to show that our results are robust to synoptic and interannual variability in fjord stratification.

2. Materials and Methods

2.1 Subglacial Plume Model

We use a steady-state plume model to characterize subglacial plumes rising along a melting, vertical terminus. The governing equations are based on a stream tube model [Smith, 1975; Killworth, 1977; MacAyeal, 1985; Jenkins, 2011], modified for a half-conical plume forced by a discrete source of subglacial discharge [Cowton et al., 2015, equations 1-4]. The entrainment rate of ocean water into the plume (u_e) is parameterized as:

$$u_e = \alpha w,$$

where α is equal to 0.1 [Morton et al., 1956] and w is the vertical velocity of the plume. All plume properties have a uniform top-hat profile along the cross section of the plume. We define the terminal level as the depth where the plume reaches neutral buoyancy and intrudes horizontally into the fjord, consistent with results from high-resolution ocean models [Cowton et al., 2015; Carroll et al., 2015]. Following Cowton et al., [2015], the initial velocity of the plume (w_0) is fixed to 1 m s^{-1} and the initial plume radius (r_0) is given by:

$$r_0 = \sqrt{\frac{2Q_{sg}}{\pi w_0}},$$

where Q_{sg} is the initial subglacial discharge flux. The initial plume temperature and salinity are set to the pressure-dependent melting point and 0, respectively. As the plume rises along the terminus, its volume increases due to entrainment of fjord waters and

41

submarine melt. We calculate the plume dilution (D_{plume}), the ratio of vertical flux across a semi-circular plume cross section of radius r compared to the initial subglacial discharge, as:

$$D_{plume}(z) = \frac{\pi r(z)^2 w(z)}{2Q_{sg}},$$

where z is the depth and w is the vertical velocity of the plume.

2.2 Submarine Melt Rate

To estimate the submarine melt of ice from the subglacial plume, we solve a three-equation model [Holland and Jenkins, 1999] describing conservation of heat and salt at the ocean-ice boundary, combined with a liquidus constraint at the interface:

$$\dot{m}(c_i(T_b - T_{ice}) + L) = \Gamma_T C_d^{1/2} c_p w(T_{plume} - T_b),$$

$$\dot{m}S_b = \Gamma_s C_d^{1/2} w(S_{plume} - S_b),$$

$$T_b = \lambda_1 S_b + \lambda_2 + \lambda_3 z,$$

where $\dot{m}$ is the melt rate, L is the latent heat of fusion, c_i and c_p are the specific heat capacities of ice and water, T_b and T_{ice} are the ocean-ice boundary and ice temperature, S_b and S_{plume} and are ocean-ice boundary and plume salinity, $C_d^{1/2}\Gamma_T$ and $C_d^{1/2}\Gamma_S$ are the thermal and haline Stanton numbers, λ_{1-3} are constants that describe the dependence of freezing point on salinity and pressure, and z is the depth. All parameters follow values given in Jenkins [2011]. We note that the plume model does not capture the potential inertial rebound of the plume to the level of neutral buoyancy [Morton et al., 1956; Carroll et al., 2015]; this flow may contribute to additional melt above the terminal level.

2.3 Fjord Hydrography

We use a compilation of shipboard surveys across Greenland fjords to provide temperature and salinity boundary conditions for the subglacial plume model (Table 1

and Table S1). All profiles are depth-averaged into 2 m bins. We assume that each survey

is representative of typical hydrographic conditions during the summer. Systems with

hydrographic profiles that do not extend to the grounding line depth are extrapolated

assuming constant values below the depth of measurements. We calculate ocean heat

content (*OHC*) as:

$$OHC = \int_{-gl}^{0} \rho_0 \, c_p T \, dz,$$

where *gl* is the grounding line depth, ρ_0 is a reference density, and *T* is the ocean

temperature.

2.4 Subglacial Discharge

To estimate subglacial discharge we integrate daily surface runoff from the

Regional Atmospheric Climate Model (RACMO2.3) downscaled to 1 km using elevation

dependence (version v0.2) over each outlet glacier catchment [Noël et al., 2015]. We

assume that all surface runoff drains immediately to the glacier bed, with no water

storage. To create probability-based catchments, we apply a Monte Carlo based approach

to calculate each outlet's catchment over a range of bed topographic maps varied within

published error ranges. We randomly vary the bed topography [Morlighem et al., 2015]

by multiplying the published error range by a random, uniformly distributed number

between -1 and 1, and add it to the published bed topography. For each iteration of the

bed topography, we then calculate the hydraulic potentiometric surface, φ, using basal

topography, z_{bed}, and ice surface topography data, z_{ice} [Morlighem et al., 2014].

Following the standard procedure of Lewis and Smith [2009] and Cuffey and Patterson

[2010], we calculate, φ as:

$$\varphi = \rho_{ice} g \left(z_{ice} + \frac{(\rho_w - \rho_i)}{\rho_i} z_{bed} \right),$$

where ρ_{ice} is the density of ice, ρ_w is the density of freshwater, and g is acceleration due to gravity. Next we determine the flow path of water along this hydraulic potentiometric surface using a simple D8 approach implemented in the TauDEM C++ software package [Tarboton, 1997]. The D8 method assigns flow from each pixel to one of its eight neighbors (adjacent or diagonal) in the direction of steepest downslope [O'Callaghan and Mark, 1984]. We then use ESRI's ArcPy Basin function to delineate catchments from the D8 direction grid. This algorithm starts at a given outlet location and recursively searches upstream from the outlet for cells that contributed to it. We flag all cells found by this recursive search as within the hydrologic catchment. After all iterations of catchment boundaries are found, we sum the number of times the pixel was in the catchment, x and divide it by the number of times the bed was varied, n.

$$\text{For pixel } (i,j) = \frac{\left(\Sigma\, x(\text{i},\text{j})\right)}{n(i,j)},$$

This provides the per outlet probability that a part of the ice sheet contributes runoff to it. We use the 95% probability area as the catchment boundary for all outlet glacier systems in this study.

3. Results

We first examine the sensitivity of all systems to variability in subglacial discharge and fjord hydrography (Figure 2). Shallow systems (defined as grounding line depth <= 500 m) produce plumes with terminal levels (depth where plume intrudes

44
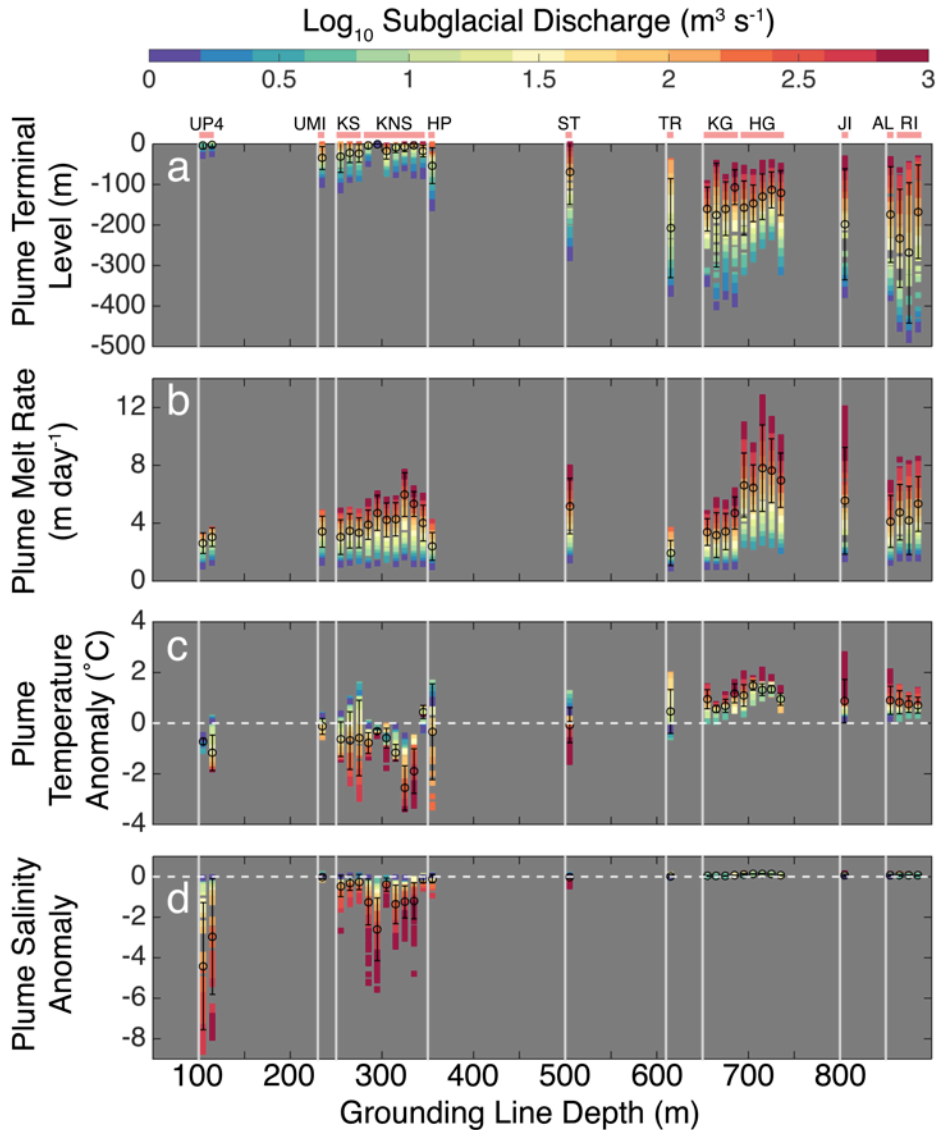
Figure 2. Subglacial plume properties for all 12 fjord-glacier systems. Sensitivity of plume terminal level **(a)**, depth-averaged melt rate **(b)**, temperature anomaly **(c)**, and salinity anomaly **(d)** to subglacial discharge. Vertical lines represent grounding line depths for the glaciers examined in this study. Vertical bars to the right of the each line show plume properties in chronological order for each glacier with that grounding line depth. Vertical bars are spaced at 10 m intervals for visibility; colors show the rate of subglacial discharge. Circles are mean summer values, error bars represent uncertainty (one standard deviation) due to temporal variability in subglacial discharge. Hydrographic profiles are averaged across each summer. Plume temperature and salinity anomaly are taken with respect to ambient fjord waters at the terminal level, salinity is expressed in Practical Salinity Scale.

horizontally into the fjord) that are confined to the upper 100 m during mean summer discharge levels, becoming surface-trapped at peak discharge (Figure 2a). In deeper systems (> 500 m), plumes are unable to penetrate into the buoyant surface water layer, resulting in deep, subsurface plumes (100 - 250 m depth). Regional variability in ocean heat content at depth drives marked differences in plume melt rate. For example, mean plume melt rate is 93% larger in Helheim (HG) than Kangerdlugssuaq (KG) despite similar grounding line depths (Figure 2b).

For adjacent fjords exposed to similar hydrographic properties, such as Kangerdlugssup Sermerssua (KS) and Rink Isbræ (RI), increasing the grounding line depth (250 vs. 850 m) results in a deepening of the mean plume terminal level from 25 to 223 m, respectively, and a 45% increase in mean plume melt rate. Increasing subglacial discharge in shallow systems (grounding line depth <= 500) generally produces plumes with progressively larger negative temperature and salinity anomalies, i.e. plumes become colder and fresher as discharge increases (Figure 2c,d and S1 in supplemental information). Increasing subglacial discharge in deeper systems results in plumes with positive temperature and salinity anomalies that equilibrate within the Polar Water layer.

For fixed subglacial discharge, plume melt rate depends on ocean heat content and grounding line depth, with grounding line depth providing a first-order control on how efficiently the plume can transfer ocean heat to the ice to allow for melting (Figure 3a). All systems collapse into characteristic lines based on their grounding line depth; synoptic and interannual variability in ocean heat content determines the plume melt rate along each line. The depth-dependent grouping of the systems is robust for a range of selected subglacial discharges (50 – 500 m^3 s^{-1}); larger discharges result in steeper slopes
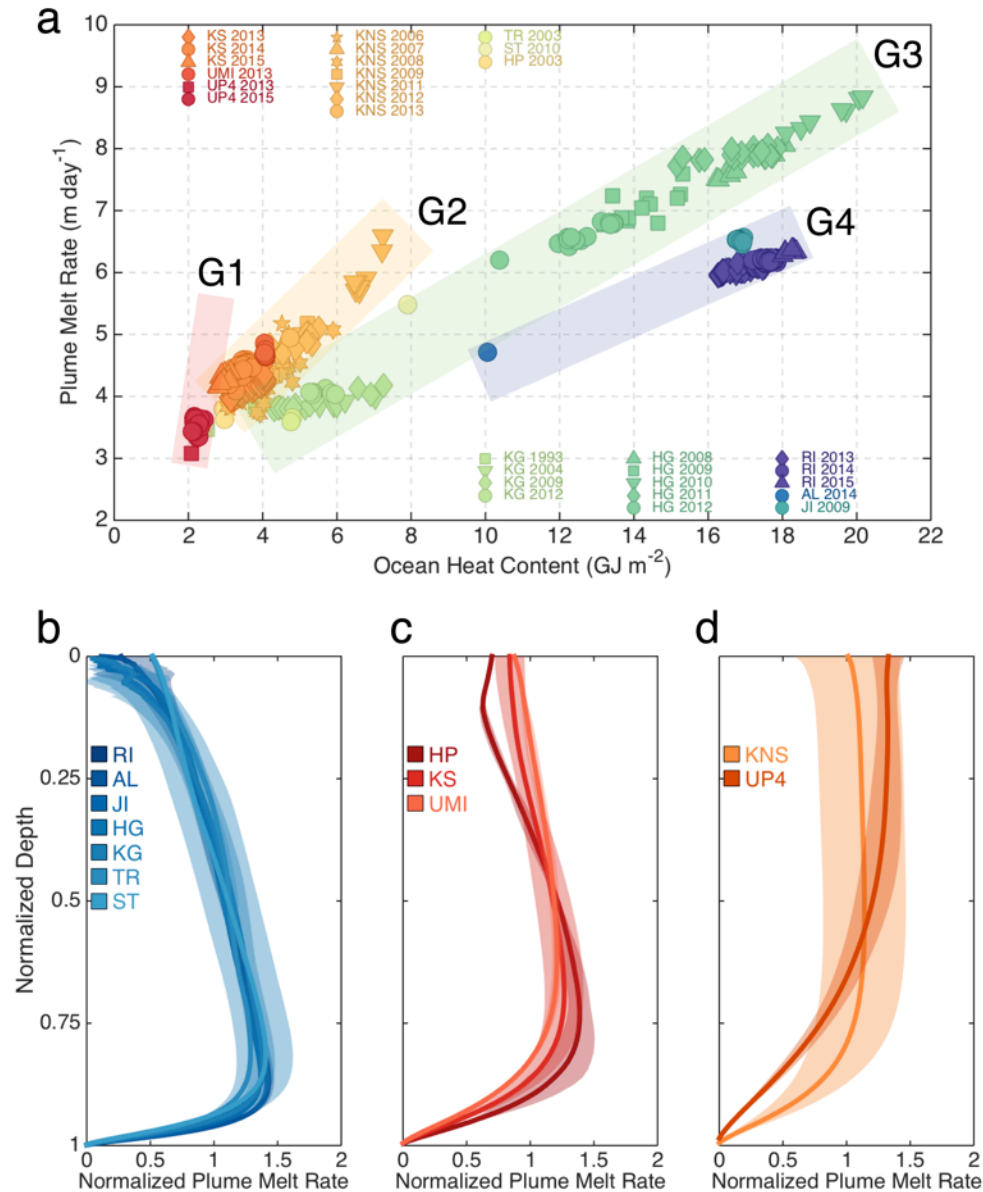
Figure 3. Sensitivity of plume melt rate to ocean heat content and corresponding vertical structure. Subglacial discharge is fixed at 250 m^3 s^{-1}, all available profiles for each system are used. **(a)**, Sensitivity of depth-averaged plume melt rate to ocean heat content. All systems collapse along characteristic lines due to their grounding line depth (G1 = 100 m, G2 = 230 - 250 m, G3 = 650 m, G4 = 800 - 850 m). Profiles of plume melt rate for all systems, with undercut **(b)** (500 - 850 m), semi-uniform **(c)** (230 – 350 m), and overcut **(d)** (100 – 250 m) melt distribution. Plume melt rate and depth are normalized by their their depth-average and maximum value, respectively. Shaded error bars represent uncertainty (two standard deviations) due to spatial and temporal variability in fjord stratification.

due to increased plume melt rate (Table S3 in supplemental information). Shallow

systems (G1 and G2) have steeper slopes (larger depth-averaged melt rate change per

ocean heat content) because surface-reaching plumes retain large velocities along the

entire terminus (Figure S2 in supplemental information). For equivalent ocean heat

content, deeper systems (G3 and G4) have shallower slopes due to dilution of the plume

at depth by entrainment, resulting in weaker depth-averaged plume velocities. Increasing

the grounding line depth from 100 to 850 m (UP4 vs. RI) results in a 30% decrease in

depth-averaged plume vertical velocity. Additionally, shallow and deep systems (such as

Kangiata Nunata Sermia (KNS) and KG, respectively) can have equivalent depth-

averaged plume melt rates, due to the dependence of submarine melt on both vertical

velocity and temperature.

Grounding line depth strongly modulates the vertical distribution of submarine

melt (Figure 3b,c,d and S3 in supplemental information). In deep systems (500 - 850 m

grounding line depth), the subglacial plume is rapidly decelerated by entrainment of

warm Atlantic Water at depth, increasing the plume temperature and leading to maximum

melt rates in the lower water column, suggestive of glacial undercutting (Figure 3b).

Directly above the grounding line, the plume consists of relatively undiluted, cold

subglacial discharge – resulting in a region of low melt and indicative of a protruding ice

"toe". As the grounding line depth is decreased (230 – 350 m), plumes entrain a larger

percentage of cold Polar Water, resulting in semi-uniform melt profiles with maxima

higher in the water column (Figure 3c). Systems with shallow grounding lines (100 – 250

m) and warm Surface Water temperatures result in overcut melt profiles with maxima in

the upper half of the water column (Figure 3d). For low subglacial discharge ($<= 50$ m^3 s$^-$

[1]), shallow systems relax towards undercut melt profiles (as shown in Figure 3b), as weakly buoyant plumes reach their terminal level at greater depth.

4. Discussion

Our results emphasize the important connection between the terrestrial ice sheet runoff signal and plume-induced circulation. Given basic observations, our results provide first-order rules of thumb for estimating the impact of plume melting on a glacier terminus. As new bathymetric and hydrographic observations become available, we anticipate that this study will aid in predictions of plume properties across Greenland fjords. Based on a realistic range of subglacial discharge, grounding line depth, and ocean heat content, we have several critical findings: i) grounding line depth and large-scale regional changes in ocean heat content exert a strong control on subglacial plumes, ii) cold, fast plumes in shallow systems and warm, slow plumes in deep systems can induce equivalent localized depth-averaged melt rates, and iii) deeply-grounded glaciers result in undercut termini, shallow glaciers support semi-uniform or overcut termini.

These two glacier geometries (deep vs. shallow) produce marked differences in fjord temperature and salinity at the plume terminal level, present across a variety of subglacial discharge rates and conduit configurations (Figure S4 in supplemental information). Our results exhibit similar qualitative trends to the scalings obtained by Slater et al., [2016]; however, future work is needed to determine if these scalings hold quantitatively for the realistic stratification observed in Greenland fjords. This study, consistent with observations and idealized ocean models [Straneo et al., 2011; Xu et al, 2012,2013; Sciascia et al., 2013; Carroll et al., 2015], demonstrates that deep fjords act as subsurface pathways for mixing and export of ice sheet runoff. These results call into

question surface-injected parameterizations of runoff in current climate models where the vertical ocean grid resolution is sufficiently fine to incorporate subsurface runoff fluxes [Lenaerts et al., 2015]. Additionally, the increase of plume dilution with grounding line depth suggests that deep systems drive more vigorous depth-integrated exchange within the fjord, implying faster replenishment of fjord waters (Figure S5 in supplemental information).

Our results suggest that regions near subglacial conduits can support a variety of terminus geometries, potentially leading to a complex calving front evolution during the meltwater season. Recent observations of the KS terminus add support to this hypothesis, showing a diverse spatial distribution of undercut and overcut regions [Fried et al., 2015]. We acknowledge that our model does not couple the ice front profile and plume, which may neglect important plume-ice feedbacks. In regions where the terminus becomes overcut or near a protruding ice "toe", the plume may detach – decreasing melt rates and the level of overcutting until the plume regains contact with the ice. The plume model results in localized melt rates on the order of meters per day, in general agreement with direct observations [Fried et al., 2015] and bulk estimates based on conservation of heat, salt, and mass [Rignot et al., 2010; Sutherland and Straneo, 2012; Xu et al., 2013]. However, our estimated melt rates are limited to a localized area (~100 m wide) on either side of the plume. Spatially-averaging melt across the terminus from a single plume results in melt rates biased ~2 orders of magnitude low compared to observations (2.0 m day^{-1} observed for KS) [Fried et al., 2015] (Text S1 and Figure S6 in supplemental information). These results imply that while a single plume may induce significant localized submarine melt, a distributed subglacial drainage system may be needed to

50

influence calving and produce terminus retreat driven by undercutting [Slater et al., 2015; Rignot et al., 2016b]. We stress that our parameterized melt rates are sensitive to the choice of turbulent transfer coefficients, developed for sloping ice shelves [Holland et al., 1999; Jenkins et al., 2010] and yet to be validated for Greenland's near vertical termini [Rignot et al., 2015; Fried et al, 2015]. Ultimately, coincident ocean and terminus ablation measurements are needed to constrain turbulent transfer coefficients and determine if submarine melt can exceed typical calving rates observed at large marine-terminating glaciers in Greenland.

To guide future observational programs, we find that plume melt rate is generally insensitive to the distance hydrographic measurements are made from the glacier (largest relative change from near-glacier to mouth was 16% for HG), as long as observations are made near the fjord where variability in ambient temperature is small and not on the shelf (Figure S7 in supplemental information). However, plume terminal level is more sensitive to measurement location, deepening by 31% in RI when using profiles from the mouth compared to near-glacier, due to stronger stratification down-fjord. For fjords with shallow sills, we would expect large variability in stratification landward and seaward of the sill, suggesting that near-glacier measurements may be necessary in systems with isolated basins.

We note that our results only apply to subglacial plume dynamics at the terminus. We have neglected potentially important external forcing such as wind, tides, and shelf-forced circulation [Straneo et al., 2010; Mortensen et al., 2013; Jackson et al., 2014]. While we anticipate the interaction of plume- and externally-forced circulation to drive variability in fjord stratification and heat content, the exchange of heat and salt at the

51

ocean-ice boundary will be largely dominated by subglacial plumes during the meltwater season because these are what drive the deep, net flows toward the glacier.

5. Conclusion

We have produced the first systematic characterization of subglacial plumes in Greenland outlet glacier fjords with grounding line depths that range from 100 to 850 m. We propose that subglacial plumes can drive substantial localized terminus melt, representing an important ocean-ice feedback that strongly depends on glacier geometry and can affect the ice sheet mass balance. This work stresses the need for realistic termini morphology in high-resolution ocean models and subsurface parameterizations of ice sheet runoff in large-scale climate models. Ultimately, a detailed understanding of plume-glacier interactions allows for improved constraints on sea level rise from the Greenland Ice Sheet.

6. Bridge

In Chapter III, I used buoyant plume theory to show that grounding line depth and fjord stratification are strong controls on meltwater plume structure and submarine melt rates in Greenland fjords. To extend this work from the terminus to the larger-scale fjord system, in Chapter IV, I use regional-scale ocean simulations to evaluate how fjord circulation forced by subglacial plumes, tides, and wind stress depends on fjord-glacier geometry.

CHAPTER IV

SUBGLACIAL DISCHARGE-DRIVEN RENEWAL OF TIDEWATER GLACIER FJORDS

This chapter was submitted to *Journal of Geophysical Research: Oceans* in April 2017. I was lead author on the paper, developing the methodology, analyzing the data, and writing the manuscript. David Sutherland (University of Oregon) served as advisor, aiding in data interpretation and manuscript editing. Emily Shroyer (Oregon State University), Jonathan Nash (Oregon State University), Ginny Catania (University of Texas in Austin), and Leigh Stearns (University of Kansas) provided feedback on manuscript drafts and aided in manuscript editing.

1. Introduction

Fjords act as deep, highly-stratified estuaries [*Geyer and Ralston*, 2011], with potential for continuous exchange between the fjord and adjacent coastal waters. In the classic model of fjord circulation [*Farmer and Freeland*, 1983], freshwater input at the head of the fjord, along with down-fjord wind stress [*Svendsen and Thompson*, 1978], drives a brackish outflow in the surface layer. Shear-driven entrainment in the outflow results in a compensating up-fjord flow of seawater to balance the loss of salt and mass. For fjords constrained by a shallow sill at the mouth, stratification below the brackish outflow consists of intermediary waters at the sill level, with deep basin waters found at depth [*Stigebrandt*, 2012].

In typical fjords, the width of the mouth and the sill depth act as first-order controls on fjord-shelf exchange. In narrow (i.e., nonrotating), shallow-silled fjords, exchange is typically regulated by hydraulic control [*Farmer and Denton*, 1985]. For

fjords with wider mouths, and or, deeper sills, exchange above the sill level can be driven by fjord-shelf density gradients [*Aure and Stigebrandt*, 1990; *Aure et al.*, 1996; *Arneborg et al.*, 2004], resulting in a baroclinic "intermediary circulation" that is gradually damped as it propagates up-fjord. Additionally, the presence of a strong geostrophic coastal current can act to restrict exchange [*Klinck et al.*, 1981], which can isolate intermediary waters [*Svendsen et al.*, 2002; *Cottier et al.*, 2005; *Nilsen et al.*, 2008]. Previous work has shown that renewal of waters below sill depth is driven primarily by two processes: 1) high-density waters sink and replace the existing basin waters [*Geyer and Cannon*, 1982; *Stigebrandt*, 1987], and 2) diapycnal mixing [*Stigebrandt and Aure*, 1989]. Tidal flow over steep sill topography provides an important mechanism for transferring energy from barotropic to baroclinic processes [*Inall et al.*, 2004] and henceforth to turbulence and mixing. Supercritical tidal flow can produce jets [*Stashchuk et al.*, 2007], bores, and hydraulic jumps [*Staalstrøm et al.*, 2015] that elevate local turbulence near the sill; subcritical tidal flow can generate internal tides that radiate into the fjord and induce remote mixing [*Arneborg and Liljebladh*, 2009].

This paradigm of fjord circulation and renewal provides valuable insight into many fjord systems; however, it is complicated by tidewater glacier fjords, where submarine melt of the terminus [*Slater et al.*, 2015] and icebergs [*Enderlin et al.*, 2016] and subglacial discharge [*Chauché et al.*, 2014; *Carroll et al.*, 2015, 2016; *Stevens et al.*, 2016; *Mankoff et al.*, 2016] can provide substantial buoyancy forcing at depth [*Straneo et al.*, 2011; *Jackson and Straneo*, 2016]. Tidewater glacier fjords provide a critical pathway by which glacially-modified waters are discharged to the coastal ocean [*Bamber et al.*, 2012] and warm ocean waters are transmitted to ice sheet margins [*Straneo and*

Heimbach, 2013]. Recent dynamic mass loss from the Greenland Ice Sheet [*van den Broeke et al.*, 2009; *Enderlin et al.*, 2014], which is driven by frontal ablation (calving and submarine melt) of tidewater glacier termini, has motivated numerous observational studies of hydrography and circulation in Greenland fjords (for a review see *Straneo and Cenedese* [2015]).

However, we still lack a precise understanding of how circulation in tidewater glacier fjords is modulated by fjord-glacier geometry (i.e., fjord width, topographic constrictions, and glacier depth) [*Beaird et al.*, 2015; *Rignot et al.*, 2016], due to a lack of sustained, full-depth ocean measurements across various Greenland fjords. Although observations are sparse, progress has been made on characterizing fjord circulation using numerical ocean models [*Cowton et al.*, 2015; *Carroll et al.*, 2015]. While these previous modeling efforts have been useful, they are two-dimensional [*Sciascia et al.*, 2014; *Gladish et al.*, 2015], focus on systems without sills [*Cowton et al.*, 2016], neglect tidal forcing, and often lack the horizontal resolution [*Bendtsen et al.*, 2015] to resolve cross-fjord gradients in the exchange flow.

Here we use a suite of idealized high-resolution ocean simulations to systematically evaluate how subglacial discharge-driven exchange flow and renewal of basin waters is influenced by fjord, sill, and glacier geometry. Additionally, we include simulations with tides and wind stress to determine how external forcing modulates the background exchange flow. While our model is idealized and neglects additional sources of buoyancy such as terrestrial runoff and sea ice/iceberg melt, our results provide valuable insight for future parameterizations of tidewater glacier fjords in large-scale climate models. This work demonstrates that subglacial

discharge emerging from glaciers grounded below the sill depth can draw shelf

waters over a sill and into fjord basins, providing an ice sheet forced mechanism for

seasonal renewal that occurs independently of external shelf forcing

2. Model Setup

2.1. MITgcm Configuration

To investigate the sensitivity of tidewater glacier fjord circulation to variations

in forcing and fjord-glacier geometry (Table 1),

Simulation Name	*W* (km)	H_s / H	H_{gl} / H	Q_{sg} (m³ s⁻¹)	*Tides*	τ_x / duration (N m⁻² / days)	τ_y / duration (N m⁻² / days)	# of simulations
Vertical plume only runs								
plumeShallowSill	2, 5, 10, 20	0.1	1	50, 250	No	0	0	8
plumeW2	2	0.25, 0.5, 1	0.25, 0.5, 1	250	No	0	0	9
plumeW5	5	0.25, 0.5, 1	0.25, 0.5, 1	250	No	0	0	9
plumeW10	10	0.25, 0.5, 1	0.25, 0.5, 1	250	No	0	0	9
plumeW20	20	0.25, 0.5, 1	0.25, 0.5, 1	250	No	0	0	9
Tide runs								
tideOnly	2, 5, 10, 20	0.25, 0.5, 1	0.25	0	Yes	0	0	12
plumeTide	2, 5, 10, 20	0.25	0.25, 0.5, 1	250	Yes	0	0	12
plumeTideNoSill	2, 5, 10, 20	1	0.25	250	Yes	0	0	4
Wind runs								
zonalWind3Day	2, 10	0.25	0.25	0	No	-0.4/3	0	2
meridWind3Day	2, 10	0.25	0.25	0	No	0	-0.4/3	2
plumeZonalWind3Day	2, 10	0.25	0.25, 0.5, 1	250	No	-0.4/3	0	6
plumeMeridWind3Day	2, 10	0.25	0.25, 0.5, 1	250	No	0	-0.4/3	6
plumeZonalWind3DayNoSill	2, 10	1	0.25	250	No	-0.4/3	0	2
plumeMeridWind3DayNoSill	2, 10	1	0.25	250	No	0	-0.4/3	2
plumeZonalWind12Day	2, 10	0.25	0.25	250	No	-0.4/12	0	2
plumeMeridWind12Day	2, 10	0.25	0.25	250	No	0	-0.4/12	2

Table 1. List of MITgcm simulations (see section 2 for details, 96 simulations total).

we use the Massachusetts Institute of Technology general circulation model (MITgcm) in a three-dimensional, hydrostatic configuration. The MITgcm is a developed version of *Marshall et al.* [1997], which integrates the primitive Boussinesq equations on a Arakawa staggered C-grid [*Arakawa and Lamb*, 1977]. The fjord is represented as a 60 km long channel, with width W and maximum basin depth H of 800 m (Figure 1a,b).
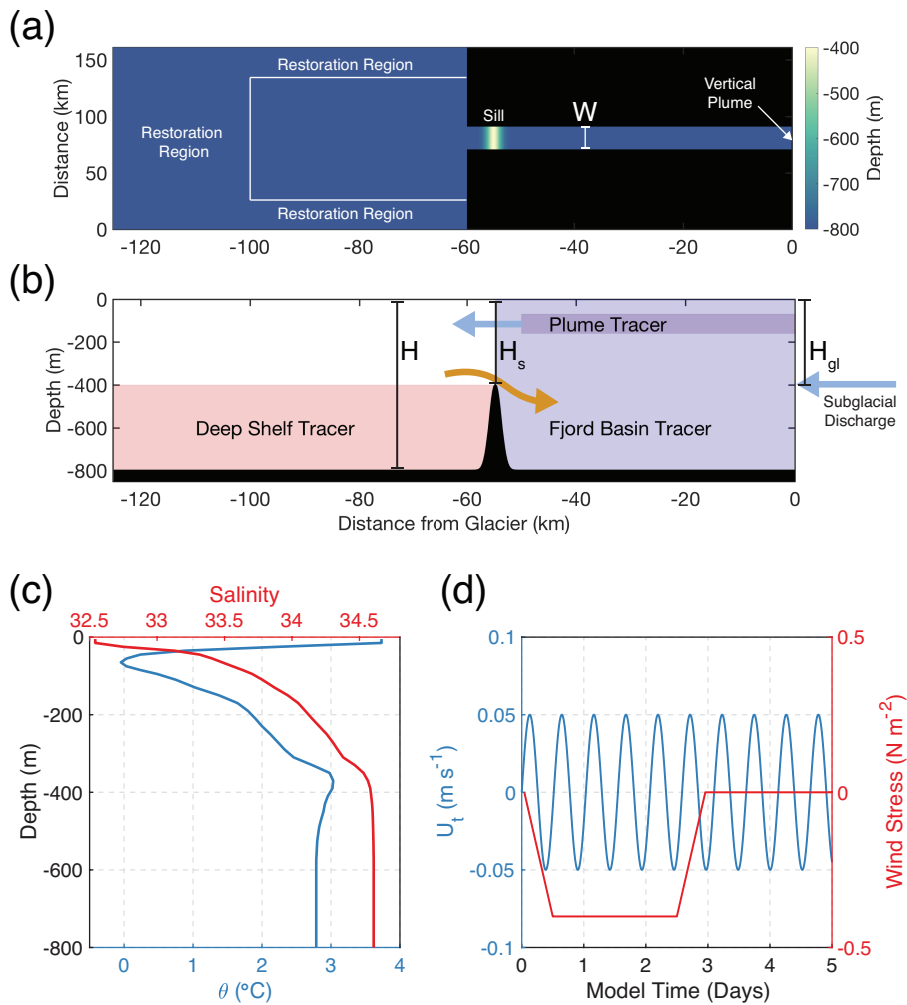
Figure 2. MITgcm model domain and forcing. (a) plan view of model domain ($W = 20$ km, $H_s / H = 0.5$, and $H_{gl} / H = 0.5$ case is shown); vertical plume is located at the centerline of the fjord head ($x = 0$ km, $y = 80$ km). (b) Centerline fjord bathymetry and passive tracers used in this study. (c) Initial model potential temperature and salinity profiles from Rink fjord, west Greenland. (d) Idealized tidal and wind stress forcing.

The glacier terminus is treated as a vertical wall at the fjord head, grounded at depth

H_{gl}. The western portion of the model domain contains a uniform shelf with a width

of 65 km and depth of 800 m. The model domain is treated as an *f*-plane with a non-

linear free surface. No-slip conditions are enforced at solid boundaries, with drag

parameterized by a quadratic drag law coefficient C_D of 2.5×10^{-3}. The fjord mouth

contains a topographic sill (Figure 1b), with the analytic form

$$h(x) = -H + (H_s - H) \exp\left[\frac{-x^2}{2L^2}\right], \qquad (1)$$

where H_s is the sill depth, and L is the width of the slope (L is set to 5 km in all

simulations). Partial grid cells are used represent the steep-sided sill topography, with

a minimum non-dimensional fraction of 0.2 [*Adcroft et al.*, 1997]. The horizontal grid

resolution (Δx, Δy) is 200 m inside the fjord, linearly telescoping to 2 km at open

boundaries on the shelf. Vertical resolution (Δz) ranges from 10 m at the free surface

to a maximum of 50 m at depth. The total number of grid cells, $nx \times ny \times nz$, is

360 × 270 × 28.

Initial temperature and salinity fields are prescribed from mean 2014 summer

hydrographic observations from Rink fjord, west Greenland [*Bartholomaus et al.*,

2016]. Stratification in Rink fjord is typical of deep Greenland fjords, consisting of

warm salty Atlantic-origin water at depth overlain by cold, fresh polar water and a

seasonal layer of warm surface water (Figure 1c). The mode-1 internal wave phase

speed computed from initial model hydrography is ~0.8 m s^{-1}, corresponding to an

internal deformation radius L_R of ~6 km for the latitude simulated (70°, $f = 1.367$ s^{-1}

). We note that simulations with shallow sills can locally reduce the initial

deformation radius in the basin (where $H = -800$ m) by roughly a factor of two, due

to destratification of ambient waters by sill-driven mixing. The equation of state (JMD95Z) follows *Jackett and Mcdougall* [1995]. The shelf region contains open boundaries at the north, south, and west edges; temperature and salinity at the boundaries are restored to prescribed initial conditions. Each open boundary contains a 20 km restoration region to prevent internal waves from reflecting back into the fjord, with an inner (outer) relaxation timescale of 1 hour (1 day). We use a grid-scaled Laplacian horizontal viscosity, combined with a horizontal biharmonic viscosity of 10^{-3} m^4 s^{-1} to suppress grid-scale noise; the minimum horizontal viscosity ($A_h = 2$ m^2 s^{-1}) is chosen so that the grid-scale Reynolds number is $O(1)$. Vertical mixing is parameterized using the nonlocal K-Profile Parameterization (KPP) scheme [*Large et al.*, 1994], with a background viscosity set to 10^{-5} m^2 s^{-1}. A 3rd order, direct-space-time flux-limited advection scheme is used to eliminate extrema in the tracer field; explicit diffusivities are set to zero.

Passive tracers, initialized with a concentration of unity, are injected into deep shelf (referred henceforth as Deep Shelf Tracer (DST)), fjord basin, and subglacial plume waters to visualize flow and estimate renewal timescales (Figure 1b). DST concentrations to the left of the sill crest (x < -55 km) are continually relaxed toward unity with a relaxation timescale of 1 hour. We use neutrally-buoyant Lagrangian floats (MITgcm FLT package) initialized at the fjord mouth and near-glacier region to visualize particle trajectories and estimate mean properties in the plume and deep return flow toward the glacier. Three-dimensional float trajectories and tracer properties are integrated hourly with a fourth-order Runge-Kutta scheme; velocities and positions are bilinearly interpolated between grid cells.

2.1. Subglacial Plume Forcing

The fjord-scale model described in this study lacks the grid resolution to resolve non-hydrostatic plume dynamics at the glacier terminus [*Xu et al.*, 2012, 2013; *Sciascia et al.*, 2013; *Slater et al.*, 2015; *Carroll et al.*, 2015]. Therefore, we use a theoretical plume model [*Morton et al.*, 1956; *Jenkins*, 2011] coupled to the MITgcm [*Cowton et al.*, 2015] to parameterize vertical convection in a half-conical, point source vertical plume adjacent to the glacier terminus. For the remainder of the paper, we use the term "vertical plume" to describe the parameterized convective plume adjacent to the glacier terminus and "plume" to describe the resultant out-fjord buoyancy-driven current. At each grid cell where the vertical plume is entraining, ambient fluid and tracers are removed, diluted according to plume theory, and placed into the cell where the vertical plume reaches neutral buoyancy. The vertical plume is located at the glacier centerline (y = 80 km); the initial subglacial discharge flux (Q_{sg}) is held constant during all model simulations. Mass is conserved in the vertical plume, which results in a small decrease (< 2%) in volume flux at the neutral buoyancy depth. Submarine melt in the vertical plume is calculated using the three-equation formulation of *Holland and Jenkins* [1999]; cooling and freshening of adjacent grid cells is implemented as a virtual salt and heat flux [*Huang*, 1993]. For a terminus depth of 800 m and width of 10 km, including ambient melt results in a <1% increase in exchange-flow transport and a slight cooling and freshening of fjord waters, therefore we neglect ambient melt outside the vertical plume region. Simulations with vertical plume forcing only are run for 120 days (Table 1, blue cells).

2.3. Tidal and Wind Forcing

Tidal forcing $U_t = U_0 \sin(\omega t)$ is applied as a uniform, barotropic zonal velocity at the M2 tidal frequency ($\omega = 1.4 \times 10^{-4}$ s^{-1}) along the western boundary of the model domain (Figure 1d). The velocity amplitude U_0 is set to 5×10^{-2} m s^{-1}, typical of predicted Arctic Ocean inverse barotropic tidal model (AOTIM) velocities on the west Greenland shelf [*Padman and Erofeeva*, 2004]. Model output for tidal simulations is stored hourly, subtidal fields are generated with a Godin filter of consecutive 24-24-25 hour moving averages [*Godin*, 1991]. Simulations with tidal forcing only and vertical plume and tidal forcing are run for 120 days (Table 1, green cells).

To investigate the response of the buoyancy-driven exchange flow to synoptic wind events, we force the model with negative along-shelf and along-fjord wind stress (down-coast and down-fjord winds, respectively). Wind stress is applied as a "top-hat" forcing, with a linear ramp-up and ramp-down period (Figure 1d). The forcing time (3 days) is the sum of the ramp-up and ramp-down time (1 day), and the time in which the wind stress is held constant (2 days). We conduct simulations with single (1 top-hat, 3 days total) and repeated (4 consecutive top-hats, 12 days total) wind events. Maximum wind stress magnitude is set to 0.4 N m^{-2}, consistent with reanalysis of storm events on the southeast Greenland shelf [*Harden et al.*, 2011; *Jackson et al.*, 2014]. Along-shelf and along-fjord wind stress relax linearly to zero in a 12 km wide region adjacent to the fjord-shelf boundary. Wind stress is applied at the end of the subglacial plume simulations (day 120); the model is then run for an additional 40 days to examine the transient response of the fjord (Table 1, red cells).

3. Results

3.1. Base Case: Vertical Plume Forcing

3.1.1. Transient Evolution

We first examine the influence of grounding line depth on the transient evolution of the exchange flow in a rapidly rotating, mid-width fjord ($W = 10$ km) with no sill (Figure 2 and 3; Table 1, blue cells). Discharge emerging from a shallow grounding line ($H_{gl} / H = 0.25$) produces a cold, fresh surface-confined plume (Figure 2).
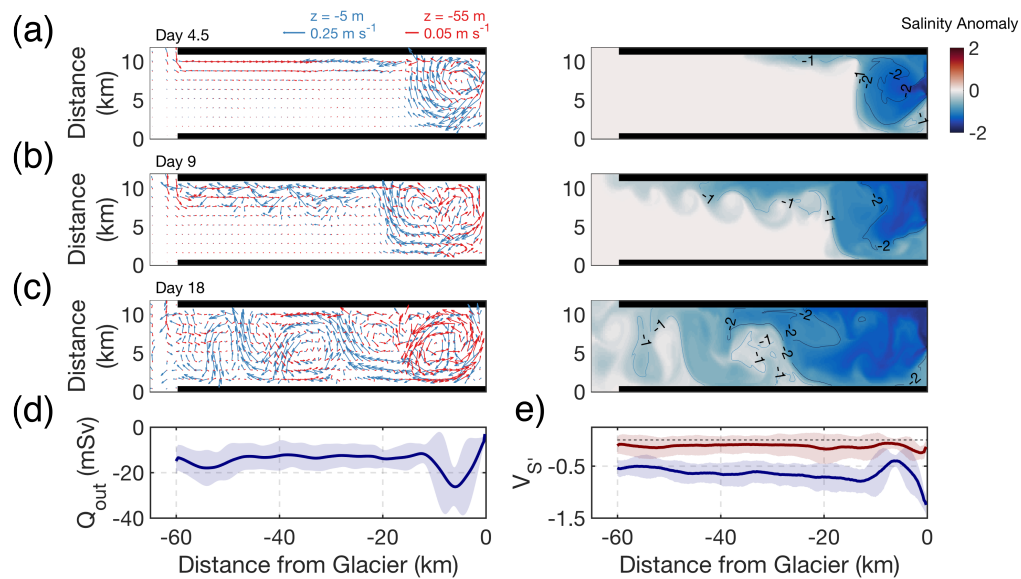
Figure 2: Transient evolution of the exchange flow at day 4.5 (a), day 9 (b), and day 18 (c) for a shallow grounding line with no sill ($H_{gl} / H = 0.25$, $H_s / H = 1$). Fjord width is 10 km; subglacial discharge flux is 250 m^3 s^{-1}. Blue and red arrows show velocity vectors in the plume and return flow ($z = -5$ m and $z = -55$ m), respectively. Shaded contours represent salinity anomaly at the plume depth; black contours are potential temperature anomaly. Anomalies are taken with respect to initial model conditions. (d) Out-fjord volume transport as a function of distance from glacier. (e) Out-fjord (blue) and in-fjord (red) volume-weighted salinity anomaly ($V_{S'}$) as a function of distance from glacier. Volume transports and volume-weighted salinity anomalies are averaged over day 30 to 120; shaded error bars show temporal variability in the exchange flow (two standard deviations).

During the initial model state the near-glacier plume develops into an anticyclonic bolus with a cyclonic return flow at depth (Figure 2a). Down-fjord from the glacier, a thin

outflowing boundary current grows uniformly in the cross-fjord direction along the north

wall. The near-glacier plume has a maximum velocity of 0.45 m s^{-1}, with minimum

potential temperature and salinity anomalies of -2.68 °C and -2.10, respectively. At day 9,

an anticyclonic vortex detaches from the near-glacier bolus and begins to propagate

down-fjord (Figure 2b). In the outflowing boundary current, unstable waves develop with

a wavelength of ~10 km and maximum amplitude of ~5 km. By day 18 and thereafter,

wave patterns become obscure and salinity gradients begin to weaken (Figure 2c). We

note that model spin-up time generally increases with fjord width, due to the influence of

unsteady eddies and recirculation (Figure S1; see Appendix B for all supplemental

figures for this Chapter). Out-fjord volume transport (Q_{out}) increases most rapidly in the

near-glacier region (-12 km $\leq$ x $\leq$ 0 km) due to vigorous lateral and vertical mixing of

ambient waters into the plume (Figure 2d). For all plume simulations, net flow across

open boundaries is balanced (i.e., $Q_{out} = Q_{in}$). Entrainment in the plume increases

outflowing volume transport as the plume transits down-fjord, with a ~26% increase in

Q_{out} from 12 km down-glacier to the fjord mouth. We emphasize that these results focus

on the relative change between simulations; caution should be used in interpreting

volume transport magnitudes as plume entrainment is dependent on the choice of model

eddy viscosity/diffusivity.

To estimate bulk tracer properties in the outflowing plume and return flow toward

the glacier, we compute out- and in-fjord volume weighted salinity anomalies VS'_{out} and

VS'_{in} as

$$VS'_{out} = \iint_A u_{out}(S_{out} - S_0)\, dA \Big/ \iint_A u_{out}\, dA, \qquad (2)$$

$$VS'_{in} = \iint_A u_{in}(S_{in} - S_0)\, dA \Big/ \iint_A u_{in}\, dA, \tag{3}$$

where u_{out} (u_{in}) and S_{out} (S_{in}) are the out-fjord (in-fjord) velocity and salinity anomalies and S_0 is the initial model salinity profile (i.e., ambient conditions). The shallow grounding line results in a negative mean VS'_{out} that is diluted toward ambient fjord properties as the plume transits down-fjord (~44% increase from 12 km down-glacier to mouth) (Figure 2e). Mean VS'_{in} is slightly negative at the mouth (-0.11), decreasing to -0.14 at 12 km down-glacier due to entrainment of fresh plume waters into the return flow beneath the plume.

In contrast, the deep grounding line ($H_{gl} / H = 1$) results in a warm, salty subsurface plume with maximum potential temperature and salinity anomalies at day 4 of 2.48 °C and 0.37, respectively (Figure 3a).
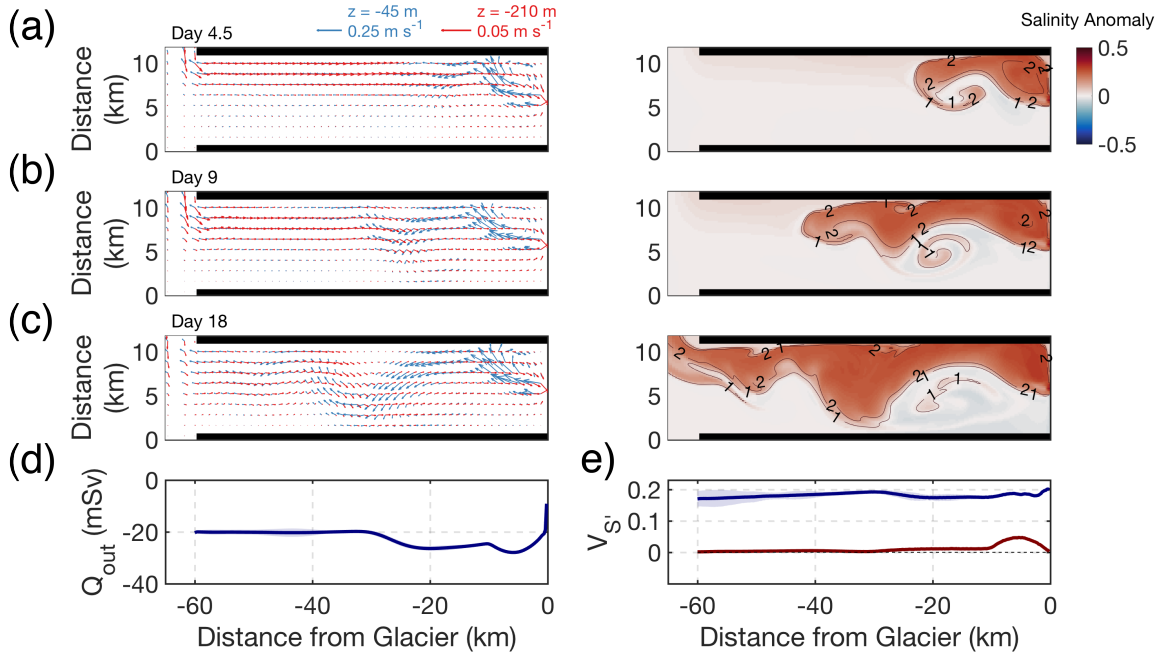
Figure 3: Transient evolution of the exchange flow at day 4.5 (a), day 9 (b), and day 18 (c) for a deep grounding line with no sill ($H_{gl} / H = 1$, $H_s / H = 1$). Fjord width is 10 km; subglacial discharge flux is 250 m³ s⁻¹. Blue and red arrows show velocity vectors in the plume and return flow (z = -5 m and z = -55 m), respectively. Shaded contours represent salinity anomaly at the plume depth; black contours are potential temperature anomaly.

Anomalies are taken with respect to initial model conditions. (d) Out-fjord volume transport as a function of distance from glacier. (e) Out-fjord (blue) and in-fjord (red) volume-weighted salinity anomaly ($V_{S'}$) as a function of distance from glacier. Volume transports and volume-weighted salinity anomalies are averaged over day 30 to 120; shaded error bars show temporal variability in the exchange flow (two standard deviations).

Similar to the shallow grounding line case, the near-glacier plume develops an anticyclonic rotation that is offset toward the north wall of the fjord, with a weak cyclonic return flow. By day 9, a southward flowing meander develops in the exchange flow approximately 25 km down-glacier (Figure 3b). At day 18 and thereafter, the meander develops into a quasi-steady feature located 30 km down-glacier, resulting in weak recirculation toward the glacier at the south wall (Figure 3c) that intensifies as the model reaches quasi-steady state. For equivalent subglacial discharge, the deep glacier results in larger out-fjord volume transport, due to increased entrainment of ambient waters in the coupled plume model (Figure 3d). Outflowing volume transport increases rapidly in the near-glacier field (maximum Q_{out} of 27.9 mSv at x $=$ -5.8 km) and subsequently decreases toward the recirculation cell at x $=$ -30 km (Figure 3d), indicative of along-fjord divergence in the flow. From the recirculation cell to the fjord mouth, entrainment in the subsurface plume increases outflowing volume transport by ~16%. The deep grounding line results in a positive mean VS'_{out} of 0.19 at x $=$ -5.8 km, decreasing to 0.17 at the fjord mouth due to dilution of the plume. Mean VS'_{in} is negligible at the fjord mouth (<0.15% increase from ambient conditions), reaching a maximum value of 0.05 at x $=$ -5.5 km.

3.1.2. Along-fjord Structure and Transport

We next examine how grounding line depth influences the along-fjord exchange flow structure and basin renewal. Simulations with a range of sill depths demonstrate that the depth of the grounding line relative to the sill (i.e., H_{gl} / H_s) is a primary control on the exchange flow-driven renewal of deep basin waters (Figure 4).
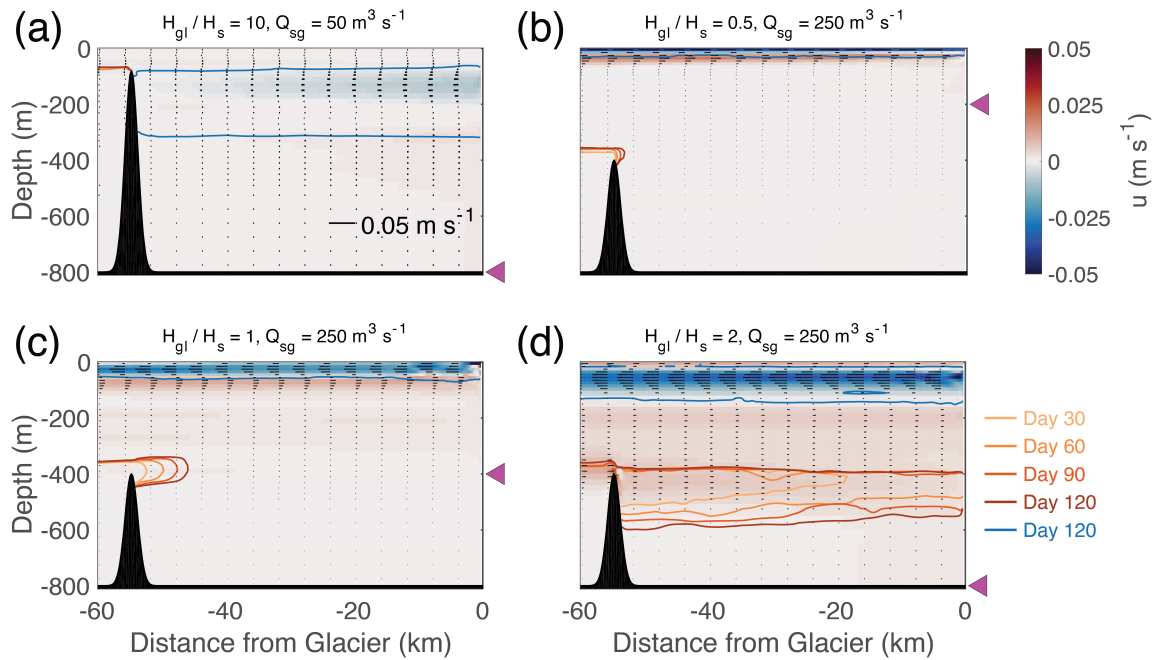
Figure 4. Along-fjord velocity and tracer evolution for varying sill-glacier geometry and subglacial discharge flux. Fjord width is 10 km. Shaded colors show mean along-fjord velocity; black arrows represent velocity vectors. Along-fjord velocity is averaged over model day 30 to 120; both velocity and tracers are averaged in the cross-fjord direction. Contours represent tracer concentrations of 0.1 for the plume at day 120 (blue) and deep shelf tracer at day 30, 60, 90, and 120 (orange to red colors). Left-pointing triangles represent grounding line depth.

For weak subglacial discharge emerging from a deeply-grounded glacier, the presence of a shallow sill traps a weak outflowing plume in the fjord basin (peak along-fjord velocity of -0.01 m s-1 at z = -135 m), with a small overflow above the sill depth (Figure 4a). In systems with glaciers grounded above, and or, at sill

depth, deep fjord waters remain isolated from the exchange flow (Figure 4b,c), inhibiting renewal of basin waters. For this glacier depth ($H_{gl} / H \leq 0.5$) and subglacial discharge flux of 250 m^3 s^{-1}, the plume is confined to near-surface depths, with the strongest return flow in the shear layer directly beneath the outflow. For $H_{gl} / H = 1$, the simulation results in a diffuse subsurface plume that spans ~120 m in the vertical, with a peak along-fjord velocity of -0.05 m s^{-1} at 55 m depth (Figure 4d). In this case, entrainment in the vertical plume exports deep basin waters to shallower depths, enabling the return flow to progressively fill the basin with a weakly-stratified layer fed by waters at the sill depth.

Increasing fjord width results in larger out-fjord volume transport, due to increased lateral and vertical mixing in the plume from recirculation (Figure 5a). This increase in out-fjord volume transport is accompanied by elevated variance in transport, due to temporal variability in the exchange flow driven by recirculation cells. For all fjord widths simulated, deep grounding lines result in the largest out-fjord volume transports due to increased entrainment in the vertical plume. Increased ambient mixing in wide fjords tends to relax out-fjord volume-weighted potential temperature and salinity anomalies toward ambient conditions (Figure 5b,c). Note that out-fjord volume-weighted potential temperature anomaly is computed in the same manner as equation 2. Plume dilution is highest in wide fjords with shallow glaciers, where instability and recirculation in the exchange flow erodes and mixes strong near-surface stratification into the surface-confined plume.
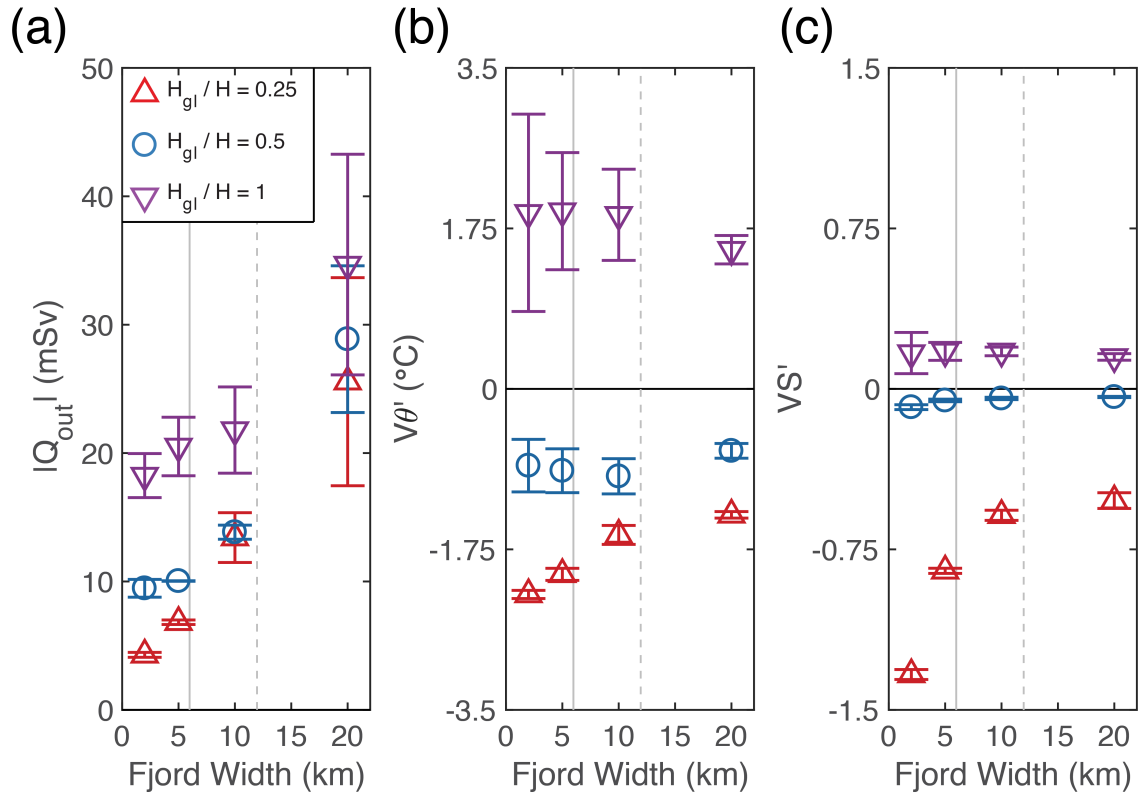
Figure 5. Out-fjord volume transport (a) and volume-weighted potential temperature (b) and salinity anomaly (c) computed at the fjord mouth (x = -60 km) for varying sill, fjord, and glacier geometry. Subglacial discharge flux is 250 m³ s⁻¹. Colors show grounding line depth. Open circles represent mean values averaged over the range of sill depths and over day 90 to 120; error bars show two standard deviations from mean. Solid and dashed vertical lines show the internal deformation radius L_R and $2L_R$, respectively. L_R is computed from initial fjord hydrography. Note the different scales used on the y-axis in (b) and (c).

3.1.3. Passive Tracers

To assess the influence of fjord-glacier geometry on renewal of basin waters we compute the fraction of fjord basin tracer and DST remaining in the basin at model day 120. Tracer fraction is computed by integrating tracer concentrations from the right of the sill crest to the first wet grid cell adjacent to the glacier wall (i.e., x = -55 km to x = -0.2 km) and normalizing by the basin volume over the same region. The fraction of basin tracer remaining at day 120 is most sensitive to grounding

line and sill depth in narrow fjords, where the exchange flow-driven export of

basin waters acts on a smaller basin volume (Figure 6a).
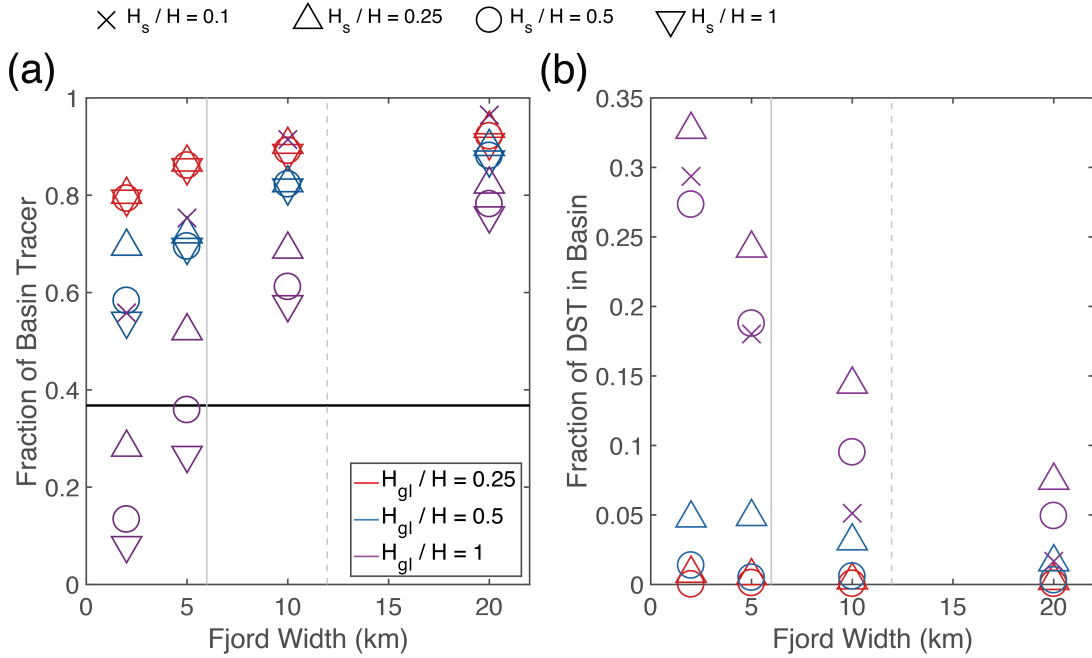
Figure 6. Fraction of fjord basin tracer (a) and DST tracer (b) in basin at model day 120 for varying sill, fjord, and glacier geometry. Subglacial discharge flux is 250 m^3 s^{-1}. Marker shapes show sill depth; colors represent grounding line depth. Solid black line in (a) shows value of e^{-1} (i.e., 37% of fjord basin tracer remaining). Solid and dashed vertical lines show the internal deformation radius L_R and $2L_R$, respectively. L_R is computed from initial fjord hydrography

For the narrowest fjord simulated (W = 2 km), a deep grounding line (purple

markers) results in a drawdown of fjord basin tracer below the e-folding value for

all sill depths tested. For a fjord width of 5 km, drawdown below this level only

occurs when H_s / $H \geq 0.5$. The effect of the sill in limiting basin tracer export is

most pronounced in deeply-grounded glaciers, where the deep return flow

interacts with sill topography. The fraction of basin tracer remaining at day 120

increases sublinearly with fjord width, as recirculation-driven mixing increases

out-fjord volume transport in wide fjords. In the absence of this mechanism, we

would expect renewal timescales to increase linearly with fjord width. For all cases, the addition of a shallow sill ($H_s / H = 0.1$) is roughly equivalent to reducing the grounding line depth by a factor of one half. Narrow fjords with deep grounding lines contain the largest fraction of DST in the basin at model day 120; in these simulations the vertical plume quickly draws down and fills the small basin volume with ambient waters at the sill depth (Figure 6b). Systems with shallow grounding lines ($H_{gl} / H = 0.25$) result in negligible transport of DST into the basin (<0.01 for all fjord widths and sill depths tested). For deep grounding lines with shallow and mid-depth sills ($H_S / H = 0.25$ and 0.5), in-fjord transport is constrained through a smaller cross-sectional area, resulting in increased return flow velocities in the first wet cell above sill depth and elevated transport of DST into the basin. For the shallowest sill simulated ($H_s / H = 0.1$), sill topography partially blocks the exchange flow and diminishes this effect.

3.1.4. Lagrangian Floats

In order to separate the exchange flow from coherent flow structures (such as recirculation cells and eddies) that persist in the fjord, we compute trajectories and statistical properties of time-released Lagrangian floats in the plume and deep return flow (Figures 7-9). For this section, we focus on the case where the glacier is grounded below the sill depth ($H_{gl} / H = 1$ and $H_s / H = 0.5$), generating a return flow that draws shelf waters at the sill depth into the fjord basin.

The spatial distribution of plume and return flow floats reveals the complex circulation that results from interactions between the exchange flow and recirculation cells/eddies (Figure 7a-g). For a fjord width of 2 km, plume and return flow float
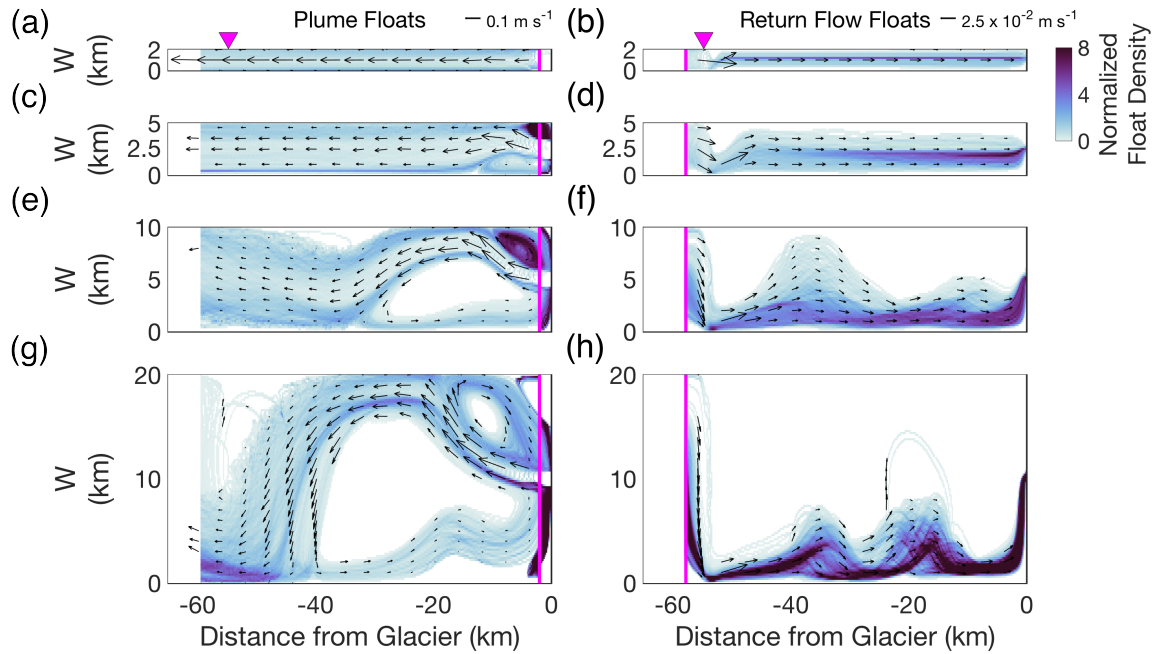
Figure 7. Normalized density for plume (a) and return flow (b) floats. Fjord width is varied from 2 to 20 km. Sill-glacier geometry corresponds to $H_s / H = 0.5$, $H_{gl} / H = 1$; subglacial discharge flux is 250 m^3 s^{-1}. Plume and return flow floats spanning the width of the fjord are time-released daily after day 30 at near-glacier ($x = -2$ km; $z = -45$ m) and fjord mouth ($x = -58$ km; $z = -390$ m) locations, respectively. Dashed magenta line shows the along-fjord location of the float release; downward-pointing triangles show the location of the sill crest. Shaded colors represent integrated float density at day 120, normalized by mean float density in the fjord. Black arrows show mean float velocity vectors, spaced at 1 km intervals in the cross-fjord direction. Float densities are computed from plume and return flow floats that successfully transit to the fjord mouth ($x = -60$ km) and first wet cell adjacent to the glacier ($x = -200$ m), respectively.

velocities are largest slightly above the fjord centerline and decrease toward the fjord

walls due to boundary effects (Figure 7a,b). As the fjord width is increased to 5 km,

the near-glacier plume forms a narrow jet that tends toward the north wall, generating

a pair of small cyclonic and anticyclonic and recirculation cells to the south and north

of the vertical plume, respectively (Figure 7c). As the plume evolves down-fjord, the

largest along-fjord velocities are found near the north wall. Return flow floats are

advected towards the southeast over the sill, with maximum float densities

71

concentrated slightly below the fjord centerline in the slow return flow (Figure 7d).

For fjord widths of 10 and 20 km, the near-glacier jet transitions into a boundary

current over a ~10 and ~20 km horizontal length scale, respectively (Figure 7e,g). As

the boundary current flows down-fjord along the north wall it then veers southward,

generating a large geostrophically-balanced cyclonic recirculation cell (Text S1 and

Figure S2 in the supplemental information). Plume float densities are largest in the

north stagnation cell above the vertical plume, the near-terminus region behind the

float release location, and in the shear margins of the plume where vorticity is

elevated. For these wide fjords, the return flow toward the glacier forms a slow,

narrow boundary current that is constrained to the south wall (Figure 7f,h).

Plume float residence time (the time required for the float to transit the length

of the fjord) generally increases with fjord width, with distributions exhibiting higher

positive skew in wide fjords (Figure 8a). Median plume float residence times are

6.79, 14.7, 24.2, and 18.3 days for corresponding fjord widths of 2, 5, 10, and 20 km.

Plume floats are freshened and cooled as the fjord widens, due to increased

recirculation-driven mixing of ambient waters into the outflowing plume. For the

narrowest fjord examined ($W = 2$ km), plume float cross-fjord position is fairly

uniform across the width of the fjord, with a median value of ~0.61 (cross-fjord

position of 1 is at the north wall). As the fjord width is increased to 5 km, the median

cross-fjord position shifts to ~0.73, with plume float position biased toward the north
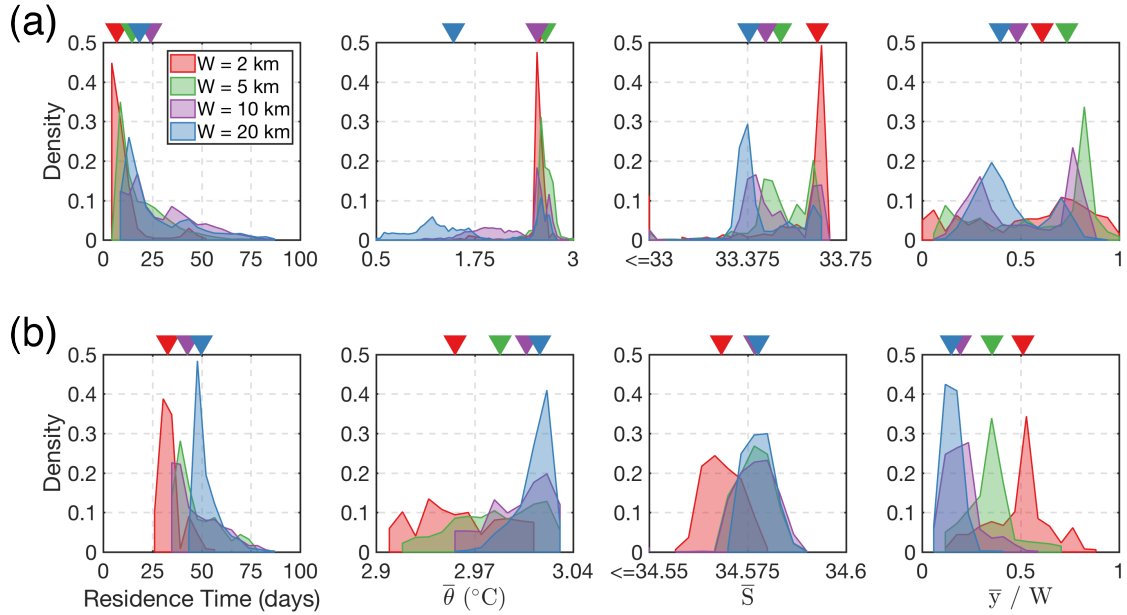
Figure 8. Normalized histogram of plume (a) and deep return float (b) residence time, potential temperature, salinity, and normalized cross-fjord position for varied fjord width. Sill-glacier geometry corresponds to $H_s / H = 0.5$, $H_{gl} / H = 1$; subglacial discharge flux is 250 m^3 s^{-1}. Plume and return flow floats spanning the width of the fjord are time-released daily after day 30 at near-glacier ($x = -2$ km; $z = -45$ m) and fjord mouth ($x = -58$ km; $z = -390$ m) locations. Histograms are computed from mean plume and return flow float properties, averaged over the transit to the fjord mouth ($x = -60$ km) and first wet cell adjacent to the glacier ($x = -200$ m), respectively. Colors represent fjord width; downward-pointing triangles show median values.

wall. For larger fjord widths ($W = 10$ and 20 km), cross-fjord position distributions become bimodal, as the plume bifurcates into a outflow on the northern wall and recirculation cells that span the fjord width. For the widest fjord simulated ($W = 20$ km), recirculation dominates the distribution, shifting the median cross-fjord position southward to ~0.40. Residence time for return flow floats also increase with fjord width (Figure 8b), with median plume float residence times of 32.7, 42.6, 42.8, and 49.7 days for fjord widths of 2, 5, 10, and 20 km, respectively. Return flow floats become warmer and saltier (less diluted) as the fjord widens, with reduced spread in potential temperature and salinity distributions. For the widest fjord simulated ($W =$

20 km), return flow float cross-fjord position converges to a narrow distribution

slightly above the south wall of the fjord, with a median value of ~0.15.

Examination of return flow float trajectories demonstrates that rapid

drawdown of basin waters by the vertical plume in narrow fjords allows for the

return flow to cascade deep into the fjord basin. (Figure 9a).
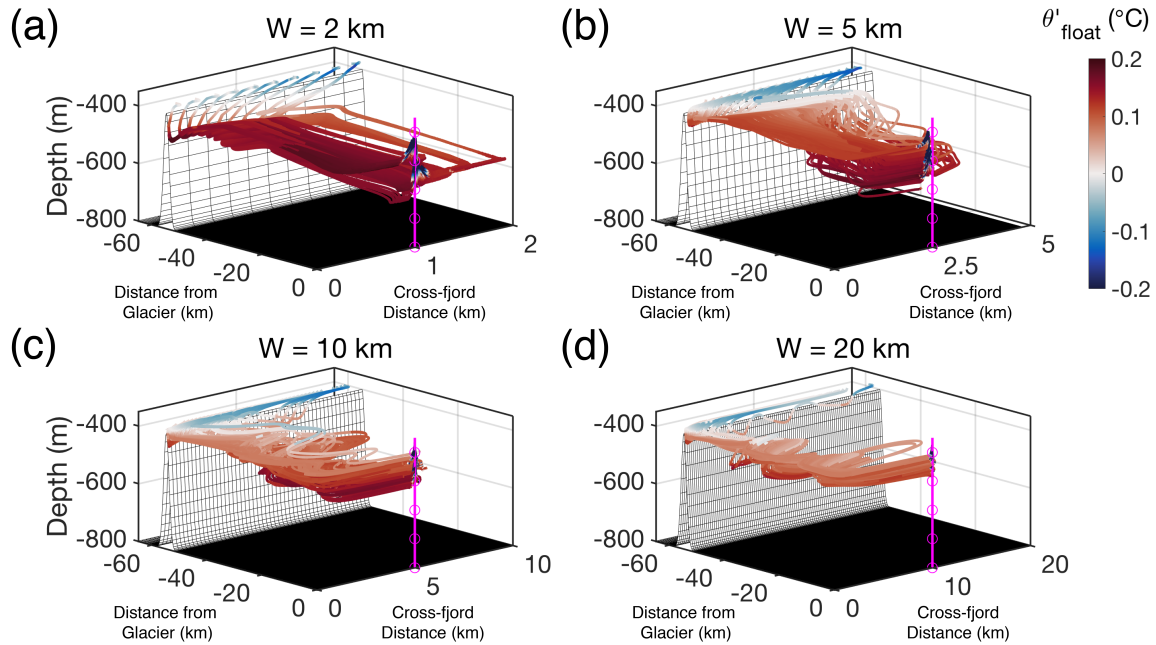
Figure 9. Return flow float trajectory and potential temperature anomaly for varying fjord width. Sill-glacier geometry corresponds to $H_s / H = 0.5$, $H_{gl} / H = 1$; subglacial discharge flux is 250 m^3 s^{-1}. Return flow floats spanning the width of the fjord are time-released daily after day 30 near the fjord mouth slightly below sill depth (x = -58 km; z = -390 m). The final 200 floats to successfully transit from the fjord mouth to the first wet cell adjacent to the glacier (x = -200 m) are shown. Vertical magenta line represents the vertical plume centerline; circles show 100 m depth intervals. Potential temperature anomaly is taken with respect to the initial model conditions at the float depth.

For the initial fjord hydrography used in this study (i.e., ambient conditions),

potential temperature below the near-surface layer reaches a maximum slightly

above the sill and progressively cools at depth (e.g., Figure 1c). This temperature

stratification results in return flow floats that exhibit negative potential temperature

anomalies as they are advected over the sill and shoal. Potential temperature anomalies then become increasingly positive as the return flow floats cascade into the cooler basin; this effect is most pronounced in narrow fjords. As the fjord widens, the vertical plume becomes less efficient at drawing down basin waters, resulting in a shallower return flow of sill depth water toward the glacier (Figure 9b,c). For the widest fjord simulated, the return flow is located along the south wall slightly below sill depth (Figure 9d).

3.2. Tidal Forcing

To investigate how tidal forcing modulates the inflow of deep shelf waters in narrow and wide fjords, we first focus on simulations with a shallow sill ($H_s / H =$ 0.25) and tidal forcing only (i.e., no subglacial discharge; Table 1, green cells). For all tidal simulations, baroclinic tidal velocities over the sill are less than the mode-1 internal wave phase speed, implying a subcritical flow regime (i.e., Froude number < 1). For a fjord width of 2 km, the interaction of the barotropic tide with a shallow sill generates internal tides that reflect off the glacier wall, leading to a two dimensional partially-standing wave response in the fjord and resulting in an intrusion of DST that extends to within ~20 km of the glacier (Figure 10a). As the fjord width is increased to 10 km, the internal tide propagates cyclonically around the fjord basin as a internal Kelvin wave, producing an intrusion of DST that spans the horizontal extent of the fjord and reaches the glacier face. (Figure 10b and Movie S1 and S2 in supplemental information). For both fjord widths, maximum DST concentrations are located slightly below sill depth, with concentrations of 0.5 confined to depths between -100 and -100 m.
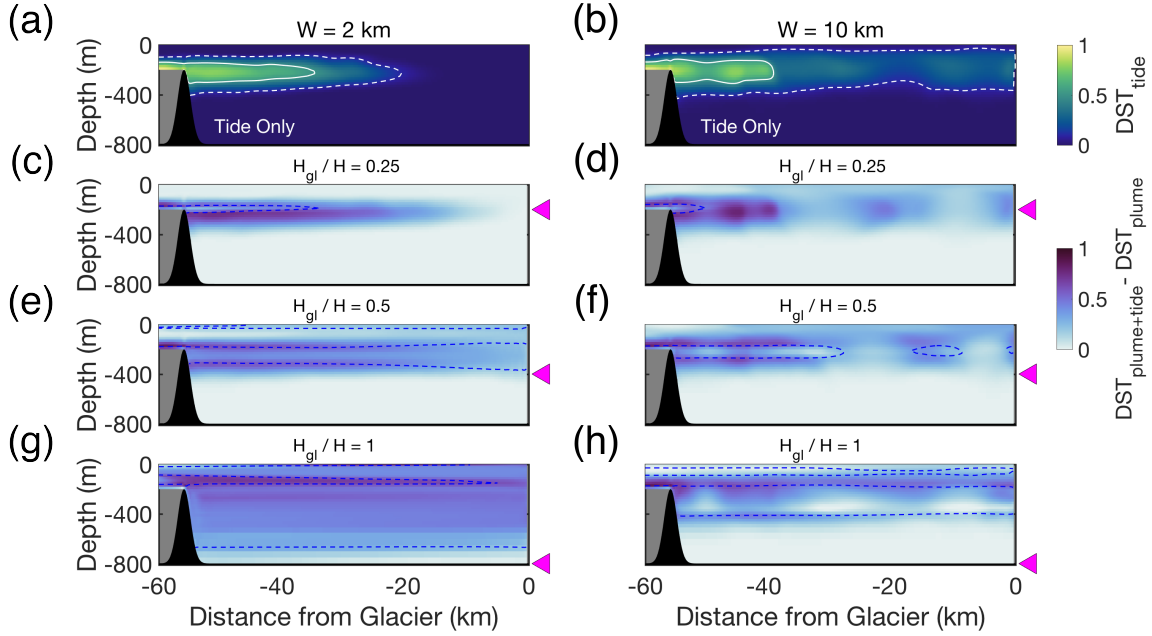
Figure 9. Along-fjord DST concentration for varying fjord-glacier geometry and forcing. Sill geometry corresponds to $H_s / H = 0.25$; subglacial discharge flux is 250 m^3 s^{-1}. Shaded colors in (a) and (b) represent DST concentration for simulations with tidal forcing only (DSTt$_{ide}$); dashed and solid white contours show tracer concentration of 0.1 and 0.5, respectively. Shaded colors in (c) through (h) show the difference in DST concentration between vertical plume + tidal forcing and vertical plume only simulations (DST$_{plume+tide}$ - DST$_{plume}$). Dashed blue contours show tracer concentration of 0.1 for the vertical plume only case; gray colors show region where DST tracer is restored. Simulations with tidal forcing are filtered with a Godin filter. DST concentrations are averaged in the cross-fjord direction and over day 84 to 114 (to account for filter window edge effects); left-pointing triangles in (c) through (h) represent grounding line depth. confined to depths between -100 and -300 m.

For a fjord width of 2 km, DST concentrations of 0.5 intrude ~21 km into the fjord basin and exhibit a diffuse frontal structure (Figure 10a). Using the maximum tidal velocity observed over the sill (0.39 m s^{-1}) yields a tidal excursion of ~8.7 km. As the fjord width increases to 10 km, the front sharpens and the modeled intrusion reaches a smaller distance of only ~16 km (Figure 10b). In this wider fjord, maximum tidal velocities at the sill increase to 0.57 m s^{-1}, with a corresponding tidal excursion of ~12.5 km.

Simulations with both vertical plume and tidal forcing reveal how tide-sill interactions modify the vertical structure of DST in the basin (Figure 10c-h). For systems grounded above sill depth (H_{gl} / H = 0.25), the addition of tidal forcing primarily increases DST concentrations directly below the sill depth, with equivalent intrusion lengths compared to the simulations with tidal forcing alone (Figure 10c,d). For glaciers grounded below sill depth (H_{gl} / H = 0.5), the largest increase in DST concentration occurs directly above the sill and at the maximum depth of the internal wave vertical excursion (~-280 m) (Figure 10e,f). For a deep glacier in a 2 km wide fjord (H_{gl} / H = 1), DST concentrations increase most substantially in a thin layer above the sill depth (Figure 10g). In the 10 km-wide fjord, this increase is distributed across a greater vertical extent (Figure 10h). For all fjord widths examined, the addition of tidal forcing has a limited impact on the export of basin water (<10% decrease in fjord basin fraction at day 120); however, the composition of basin waters is substantially modified by tides (Figure S3 in the supplemental information). Simulations with tidal forcing only in 2 and 10 km-wide fjords result in DST fractions of 0.09 and 0.14 at day 120, respectively. Combining vertical plume forcing and tides in a 2 km (10 km) wide fjord increases DST fraction at day 120 by ~1476 (5060), 160 (410), and 126 (141)% for a corresponding H_{gl} / H of 0.25, 5, and 1. We note that including ambient melt in the tidal simulations has a negligible effect on DST fractions (<1% change.

3.2. Wind Forcing

We next consider the influence of along-fjord and along-shelf wind stress on fjord circulation (Figure 11; Table 1, red cells). For a 2 km-wide fjord, 3-day along-fjord wind

forcing (black line) drives a strong outflow in the upper layer, resulting in a maximum

out-fjord volume transport of -32.87 mSv during peak wind stress at day 121.5

(Figure 11a). During the wind event, isopycnals in the upper 50 m of the water

column at the sill crest are heaved ~50 m in the vertical and outcrop (not shown). The
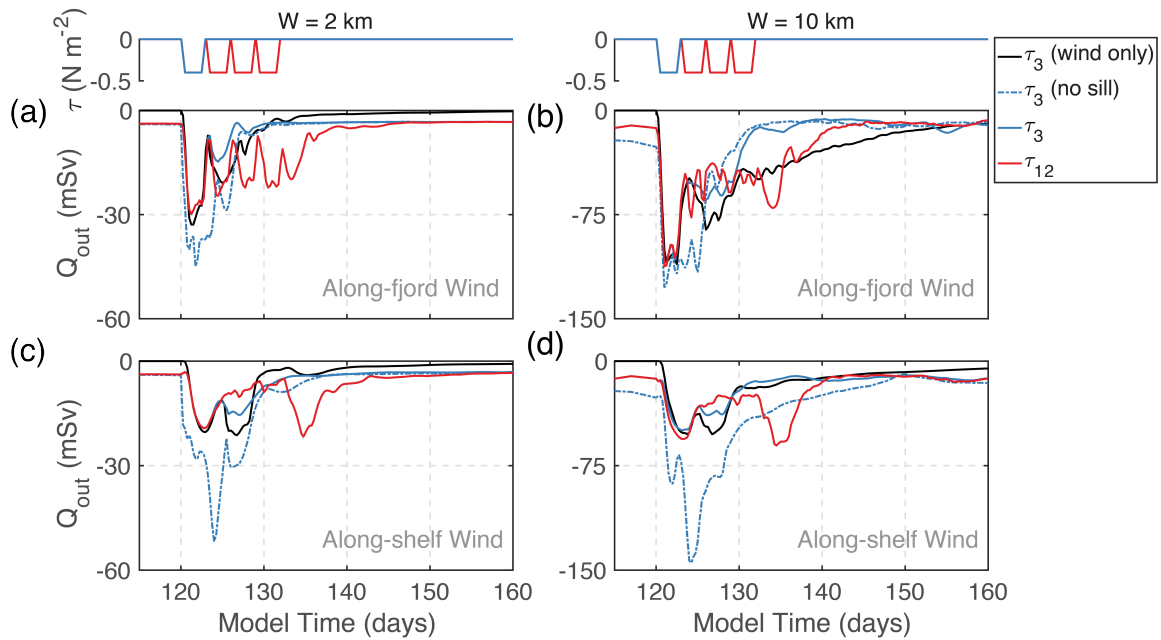
Figure 11. Time-varying out-fjord volume transport computed at the sill crest for varying fjord geometry and wind forcing. Sill-glacier geometry corresponds to $H_s / H = 0.25$, $H_{gl} / H = 0.25$; subglacial discharge flux is 250 m^3 s^{-1}. Solid black lines show simulations with wind stress forcing only. Solid blue and red lines show vertical plume and 3 and 12 day wind forcing, respectively. Dashed blue lines show vertical plume and 3 day wind forcing with no sill. Note the different scales used on the y-axis.

wind-driven flow is primarily baroclinic, with a small net inflow of ~30 m^3 s^{-1}

during peak wind forcing. As wind stress is reduced, out-fjord volume transport

decreases to -7.23 mSv (day 123.25). During relaxation, flow in the upper layer

reverses direction toward the glacier (Figure S5 in supplemental information), with

an compensating out-fjord transport in the lower layer of -20.87 mSv (day 125).

Several small oscillations occur during spin-down, with out-fjord volume transport

diminishing to -0.25 mSv by day 160. For the 10 km-wide fjord, maximum volume transports are increased by roughly a factor of 4 (Figure 11b). In this wide fjord, along-fjord winds produce an Ekman transport-driven convergence along the north wall, depressing isopycnals and resulting in a geostrophic flow that persists during spin-down (not shown). Along-shelf winds in a 2km wide fjord result in a smaller peak out-fjord volume transport of -21.27, increasing to -52.49 mSv for a 10km-wide fjord (Figure 11c,d). We note that along-shelf winds have a limited influence on cross-fjord density structure, reducing the timescale for spin-down compared to the along-fjord wind case shown in Figure 11b.

Simulations with both vertical plume and wind forcing (blue and red lines) show that wind-driven circulation dominates over the buoyancy-driven exchange flow. For a fjord width of 2 (10) km, 3-day along-fjord winds amplify the exchange flow by a factor of ~7.5 (8.6). Maximum volume transports are comparable to simulations with wind forcing only (Figure 11a,b); transports in simulations with mid-depth and deep grounding lines also converge to wind only values (not shown). For 3-day along-shelf winds, the exchange flow in the 2 km (10 km) wide fjord is amplified by a factor of ~5.2 (2.3) (Figure 11c,d). For all fjord widths examined, exclusion of the shallow sill (i.e., no sill; dashed blue line) elevates volume transport; the largest increases are observed in the along-shelf wind simulations. For 12-day along-fjord winds (red line), volume transports reach maximum values during the first "top hat" forcing event (Figure 11a,b). In contrast, 12-day along-shelf wind simulations have comparable volume transports during peak wind forcing and relaxation (day 134) (Figure 11c,d). Integrating out-fjord volume transports over the

12-day along-fjord wind forcing period in the 10 km-wide fjord (Figure 11b) yields a cumulative transport of -6.14×10^{10} m^3, approximately 14% of the basin volume.

4. Discussion

4.1 Overview

In contrast to typical fjord systems, tidewater glacier fjords can have substantial fluxes of meltwater and subglacial runoff at depth; this subsurface buoyancy forcing provides a mechanism for renewal that is independent of external shelf forcing. Our results demonstrate that, for these systems, fjord-glacier geometry is a first order control on subglacial discharge-driven circulation and renewal of basin waters. While our simulations are idealized and focus on steady buoyancy forcing from subglacial discharge, we have several key results: 1) glaciers grounded below sill depth can renew basin waters with subglacial discharge plumes, 2) rotational effects in wide fjords generate vigorous recirculation and dilution in the outflowing plume and constrains the return flow to a narrow boundary current along the south wall, and 3) tidal mixing over the sill increases plume-drive transport of deep shelf waters into the basin. We stress that varying the geometric parameters examined in this study (fjord width, sill depth, and grounding line depth) can produce marked differences in fjord circulation and hydrography, which may contribute to significant contrasts among adjacent fjord/glacier systems [*Bartholomaus et al.*, 2016]. As new bathymetric and glacier bed elevation surveys become available in the future [*Morlighem et al.*, 2016], we expect these results to guide future estuarine box model parameterizations [*Garvine and Whitney*, 2006; *Gillibrand et al.*, 2013; *Tseng et al.*, 2016] of tidewater glacier fjords in large-scale climate models.

4.2 Renewal of Basin Waters

Previous work in Fennoscandia and Greenland fjords has focused on renewal of basin waters below the sill depth driven primarily by fjord-shelf density gradients [*Aure and Stigebrandt*, 1990; *Aure et al.*, 1996; *Mortensen et al.*, 2011, 2013, 2014; *Jackson et al.*, 2014] and diapycnal mixing [*Stigebrandt and Aure* , 1989]. Our results, consistent with previous two-dimensional modeling efforts [*Gladish et al.*, 2015], suggest that subglacial discharge emerging from glaciers grounded below the sill depth can be an efficient, seasonal mechanism for renewal. We note that depending on the sill depth and terminal level of the plume, subglacial discharge-driven renewal of basin waters may transition between distinct seasonal modes. During winter, and or, during the onset/end of the meltwater season when discharge is weak, fjord basins with shallow sills may act as a weakly-ventilated or closed control volumes. In this mode, the basin may act as a "filling box" [*Baines and Turner* , 1969], where the outflowing plume is blocked by the sill and progressively fills the basin downward from the initial level of neutral buoyancy (Figure 4a). For this closed system, glacially-modified waters from the plume will, at some later time, be re-entrained in the vertical plume at the terminus [*Killworth and Turner*, 1982], which may cool vertical plume waters and decrease melt rates. As discharge increases during the meltwater season, the plume's terminal level may shoal above sill depth, transitioning the basin to an open control volume and allowing for plume-driven exchange with the shelf (Figure 4b-d). We acknowledge that our choice of steady subglacial dis- charge from a single point source vertical plume is highly idealized; we would expect significant temporal variability in the subglacial hydrologic network over the duration of the

81

meltwater season [*Slater et al.*, 2017]. For equivalent subglacial discharge, an increase in the number of subglacial conduits would decrease the terminal level of the plume and amplify the strength of the exchange flow [*Carroll et al.*, 2015; *Cowton et al.*, 2015]. Additionally, interactions between the plume, subsurface buoyancy fluxes from iceberg melt [*Sulak* , 2016; *Enderlin et al.*, 2016], and episodic shelf-driven dense inflows [*Mortensen et al.*, 2011, 2013, 2014] may significantly modulate these renewal processes; assessment of potential feedbacks between these mechanism requires additional simulations beyond the scope of this paper.

4.3 Rotational Effects

Our simulations also suggest that the plume may be susceptible to instability as it flows out-fjord, resulting in larger volume transports and dilution than predicted by buoyant plume theory [*Carroll et al.*, 2015; *Slater et al.*, 2016]. In the near-glacier field, the outflowing plume develops into a anticyclonic vortex, with cyclonic rotation in the deep return flow (Figures 2 and 3), similar to previous theoretical [*Speer*, 1989; *Speer and Marshall*, 1995a], laboratory [*Fernando et al.*, 1998], and numerical modeling studies [*Deremble*, 2016] of convective point source plumes in rotating systems. For the shallow grounding line case, the surface-confined plume exhibits instability in both the near-glacier region and along the north wall of the fjord (Figure 2b-d). The shedding of anticyclonic vortices in the near-glacier plume and development of finite amplitude waves in the outflowing boundary current is consistent with previous studies of baroclinic instability in rotating, convective plumes [*Helfrich and Battisti*, 1991; *Speer and Marshall*, 1995b] and buoyancy-driven costal density currents [*Qiu et al.*, 1988]. Diagnosing the Ertel potential vorticity

reveals that the cross-fjord potential vorticity changes sign in both the near-glacier region and along the north wall (not shown), a necessary condition for baroclinic instability [*Pedlosky*, 2013; *Pickart et al.*, 2005]. We note that the instability present in our simulations is sensitive to the choice of eddy viscosity; increasing the horizontal eddy viscosity by an order of magnitude suppresses instability in the plume. These results, along with recent work detailing instability in meltwater outflows from Antarctic ice shelves [*Garabato et al.*, 2017], motivate the need for further high-resolution modeling studies of subglacial plumes in rapidly rotating systems.

Additionally, this work shows that rotational effects are an important control on the lateral structure of the exchange flow in wide, high-latitude fjords. For a fjord width of 10 km (slightly below twice the internal deformation radius computed from initial model hydrography), the plume develops geostrophically-balanced recirculation cells downstream of the glacier (Figure 7 and Figure S2 in supplemental information), increasing entrainment of ambient waters in the plume and significantly diluting the outflow of glacially-modified waters (Figure 5b,c). Observations of iceberg trajectories from west and southeast Greenland [*Sutherland et al.*, 2014; *Sulak et al.*, 2017] support these modeling results, showing significant recirculation and cross-fjord velocity gradients in the wider regions of the fjord. Additionally, the smaller stagnation cells to the north of the vertical plume (Figure 7c,e) suggest that plume waters and glacial sediment may be distributed unevenly along glacier termini. Our simulations also demonstrate that rotational effects can significantly con- strain the cross-fjord structure of shelf waters intruding into the fjord. For wide fjords, the

return flow consists of a slow, narrow boundary current that flows along the south wall (Figure 7f,h). These results imply that wide fjords may exhibit significant cross-fjord gradients in heat transport, which could contribute to spatial heterogeneity in submarine melt rates along the terminus. We anticipate that slow, rotationally-influenced outflows driven by ambient terminus melt may form similar boundary currents along the north wall. Recent observations from Petermann Glacier in northwest Greenland support this hypothesis, showing that meltwater is exported in a boundary current that is constrained along the northeast side of the fjord [*Heuzé et al.*, 2016].

4.4 External Forcing

For our choice of peak wind stress magnitude, we find that synoptic wind significantly amplifies the subglacial discharge-driven exchange flow. *Moffat* [2014] also shows that along-fjord wind forcing can be an important mechanism for modulating buoyancy-driven circulation in tidewater glacier fjords, with in-fjord transport increasing by a factor of 2.5 for a wind stress magnitude of ~0.1 N m^{-2}. Our simulations are in general agreement with these results; the subglacial discharge-driven exchange flow can be increased by roughly a factor of 8 for our maximum along-fjord wind stress of -0.4 N m^{-2}. While wind stress may be an important mechanism for amplifying the exchange flow, strong near-surface stratification limits wind-induced vertical mixing to the upper water column (Text S2 and Figure S4 in the supplemental information). In contrast, tides result in significant mixing of basin waters above the sill depth and increase the inflow of deep shelf waters in the basin. Observations from Godthåbsfjord in west Greenland also highlight the importance of

84

tidal mixing in shallow-silled tidewater glacier fjords [*Mortensen et al.*, 2011]. In Godthåbsfjord, tidal mixing of warm, fresh near-surface waters over the sill drives a baroclinic circulation in the fjord, providing an important source of local heat for submarine melt during summer and early winter. We note that our vertical plume parameterization does not provide an adequate buoyancy flux to restratify tidally-mixed waters, stressing the need for parameterizations of subsurface iceberg melt [*Enderlin et al.*, 2016] in future modeling efforts.

Our simulations, in agreement with previous models of Arctic fjords [*Støylen and Fer*, 2014], also demonstrate that tide-sill interactions in wide fjords can generate internal Kelvin waves. Propagating internal Kelvin waves can result in a wave-induced mass flux [*Støylen and Weber*, 2010], which could be responsible for the elevated transport of deep shelf waters in our tidal simulations with wide fjords (Figure S2b in supporting information). It should be noted that for our choice of baroclinic tidal velocities (<0.6 m s^{-1}), the flow regime at the sill is subcritical, limiting our parameter space to "wave type" fjords [*Stigebrandt and Aure*, 1989]. For model simulations with larger tidal amplitudes or severely-constricted sills, fjord-shelf exchange may be determined by hydraulic control [*Farmer and Freeland*, 1983; *Farmer and Denton*, 1985]. Additionally, we have neglected spring-neap variability in our idealized tidal forcing, which could lead to supercritical conditions during spring tides and the development of tidal jets [*Stashchuk et al.*, 2007]. For the grid size aspect ratio used in this study ($\Delta z / \Delta x$ of 0.1 at sill crest) a hydrostatic model is justified as nonhydrostatic pressure effects are small [*Berntsen et al.*, 2009]. However,

we acknowledge that hydraulics and exchange processes at the sill are not explicitly resolved in our simulations.

4.4 Implications for High-latitude Fjords

      This work demonstrates that the depth of the grounding line compared to the sill (i.e., H_{gl} / H_s) is a key control on subglacial discharge-driven renewal, suggesting that this parameter could be used *a priori* to identify fjords where basin renewal may occur in- dependently of external shelf forcing. A comparison of various high-latitude tidewater glacier fjords (Table 2) reveals significant heterogeneity in the geometric parameters examined in this study.

Tidewater Glacier Name	Location	W [a] (km)	H [b] (m)	H_s / H [c]	H_{gl} / H [d]	H_{gl} / H_s	Reference
LeConte	SE Alaska	1-2	350	0.06	0.71	12.5	*Motyka et al.* [2003, 2013]
Columbia	SE Alaska	2-5	480	0.04	0.88	21.0	*Love et al.* [2016]
Jorge Montt	Patagonia	1.8-5	380	0.12	0.74	6.22	*Moffat* [2014]
Kangerdlugssuaq	SE Greenland	5-20	900	0.5	0.72	1.44	*Cowton et al.* [2016]
Helheim	SE Greenland	5-13	650	0.85	1	1.18	*Sutherland et al.* [2014]
Kangiata Nunata Sermia	W Greenland	4.5-6.5	620	0.27	0.40	1.47	*Mortensen et al.* [2011, 2013, 2014]
Jakobshavn	W Greenland	4.5-9	800	0.25	1	4.00	*Gladish et al.* [2015]
Store	W Greenland	6-7	800	1	0.63	1.60	*Rignot et al.* [2016]
Rink Isbrae	NW Greenland	5-15	1100	0.39	0.77	1.98	*Bartholomaus et al.* [2016]
Kangerlussuup Sermia	NW Greenland	4-6	550	0.75	0.45	0.61	*Bartholomaus et al.* [2016]

[a] Minimum and maximum width of fjord

[b] Maximum depth of fjord

[c] Computed using depth of the shallowest sill in the fjord

[d] Computed using mean grounding line depth

Table 2. Geometric parameters for various tidewater glacier fjords.

Tidewater glacier fjords with shallow sills and grounding lines (e.g., LeConte and Jorge Montt) may act more like typical fjord systems, with a near-surface exchange flow and deep renewal primarily driven by shelf processes or wind stress [*Moffat*,

2014]. For the deeper grounding line in Columbia Glacier fjord, a subsurface plume would be trapped below the shallow sill, which could fill the basin with cold subglacial discharge [*Walters et al.*, 1988]. In deeply-grounded systems without significant sills (e.g., Helheim and Kangerdlugssuaq), we would expect subglacial discharge-driven renewal to be active and rotationally controlled in the wider regions of the fjord; however, this process may be masked by strong shelf-driven intermediary flows [*Straneo et al.*, 2010; *Sutherland and Straneo*, 2012; *Jackson et al.*, 2014]. For deeply-grounded systems in west Greenland where shelf winds are weaker (e.g., Jakobshavn and Rink fjord), we might expect subglacial discharge to be the dominant mechanism for renewal during the meltwater season; systems that are grounded above, or near, the sill depth (e.g., Kangerlussuup Sermia) would rely more on dense coastal inflows for renewal [*Mortensen et al.*, 2011]. We note that glacier retreat along a retrograde bed would deepen the grounding line, increasing the volume flux of the vertical plume and resulting in a stronger depth-integrated exchange (Figure 5). This process may increase ocean heat transport toward the glacier and provide an additional positive feedback to the tidewater glacier cycle. Retreat along seaward-sloping beds could shoal the return flow above sill depth (i.e., $H_{gl} / H_s < 1$), limiting subglacial discharge-driven renewal of basin waters. Ultimately, coupled ocean-glacier models are needed to quantify potential feedbacks between the vertical plume/exchange flow and glacier dynamics.

5. Summary and Conclusions

Tidewater glacier fjords complicate the classic model of fjord circulation and renewal, due to subsurface buoyancy forcing from submarine melt and subglacial

discharge. These systems provide a critical pathway for the export of glacially-modified waters to the coastal ocean and flow of warm ocean waters toward the ice. However, we still lack a precise understanding of how circulation in tidewater glacier fjords is modulated by fjord-glacier geometry. Here we use a suite of high-resolution ocean simulations to investigate how the subglacial plume-driven exchange flow depends on fjord-glacier geometry and external forcing from tides and wind stress. We have several critical results:

1. Glaciers grounded below sill depth can draw shelf waters over a shallow sill and into fjord basins with seasonal subglacial discharge; this process is independent of external shelf forcing.

2. Rotational effects strongly control the cross-fjord structure of the exchange flow; plumes in wide fjords develop geostrophically-balanced recirculation cells that increase the dilution and residence time of glacially-modified waters.

3. In narrow fjords the rapid drawdown of basin waters by the vertical plume allows shelf waters to cascade deep into the basin; in wide fjords the return flow consists of a thin, boundary current that flows toward the terminus slightly below sill depth.

4. Wind stress can significantly amplify the subglacial discharge-driven exchange flow; however, strong near-surface stratification limits wind-induced mixing to the upper water column.

5. Tidal mixing over a sill increases in-fjord transport of deep shelf waters and erodes ambient stratification in the basin.

Our simulations provide key insight for the development of estuarine box model parameterizations of tidewater glacier fjords and stress the need to include sea ice and iceberg melt in future fjord-scale modeling efforts that include external forcing. Ultimately, improved estimates of fjord-glacier bed topography, along with sustained observations of deep basin waters, are critical for understanding spatiotemporal variability in submarine melt rates across Greenland.

CHAPTER V

CONCLUSIONS

5.1 Overview

This dissertation explores controls on ocean-glacier interactions in Greenland fjords using high-resolution numerical ocean modeling, theory, and ocean-glacier observations. The numerical models employed in this study are highly idealized; however, the results from this dissertation provide a framework for understanding how ice sheet meltwater drives circulation, hydrography, and submarine melt in high-latitude fjord-glacier systems. In Chapter II, I use a high-resolution ocean-ice model and buoyant plume theory to investigate how ice sheet meltwater influences near-glacier circulation. In Chapter III, I analyze how meltwater plume structure and submarine melt vary across the available parameter space of Greenland fjords. Finally, in Chapter IV, I use fjord-scale numerical ocean simulations to investigate the role of fjord-glacier geometry in modulating circulation in tidewater glacier fjords. Ultimately, these chapters aid in interpreting Greenland ocean-glacier observations and identify the key parameters needed to develop parameterizations of outlet glacier fjords in large-scale climate models.

5.2 Dissertation Summary

In Chapter II, I use buoyant plume theory and a nonhydrostatic, three-dimensional ocean–ice model of a typical outlet glacier fjord in west Greenland to investigate the sensitivity of meltwater plume dynamics and fjord-scale circulation to subglacial discharge rates, ambient stratification, subglacial conduit geometry, and numerical model parameters. The terminal level of a rising plume depends on the cumulative turbulent entrainment and ambient stratification. Plumes with large vertical velocities penetrate to

the free surface near the ice face; however, midcolumn stratification maxima create a barrier that can trap plumes at depth as they flow down-glacier. Subglacial discharge is varied from 1–750 m^3 s^{-1}; large discharges result in plumes with positive temperature and salinity anomalies in the upper water column. These results demonstrate that plumes intruding into deep, stratified outlet glacier fjords do not always retain the cold, fresh signature of meltwater but may appear as warm, salty anomalies. I find that fjord-scale circulation is sensitive to subglacial conduit geometry; a distributed subglacial network increases plume dilution and drives a stronger fjord-scale exchange flow. Classic plume theory is in general agreement with numerical ocean simulations and provides a useful estimate of plume outflow depth; however, more complex models are needed to resolve the fjord-scale circulation and melt rates at the ice face.

In Chapter III, I produce the first systematic characterization of subglacial plumes in Greenland outlet glacier fjords with grounding line depths that range from 100 to 850 m. These results show that grounding line depth is a strong control on plume-induced submarine melt: I find that deep glaciers produce warm, salty subsurface plumes that undercut termini, and shallow glaciers produce cold, fresh surface-trapped plumes that can overcut termini. Due to sustained upwelling velocities, plumes in cold, shallow fjords can induce equivalent depth-averaged melt rates compared to warm, deep fjords.

Finally, in Chapter IV, I use a suite of idealized, high-resolution numerical ocean simulations to investigate how fjord circulation driven by subglacial plumes, tides, and wind stress depends on fjord width, grounding line depth, and sill height. I find that the depth of the grounding line compared to the sill is a primary control on the plume-driven renewal of basin waters. In wide fjords the plume exhibits strong lateral recirculation,

increasing the dilution and residence time of glacially-modified waters. Rapid drawdown of basin waters by the subglacial plume in narrow fjords allows for shelf waters to cascade deep into the basin; wide fjords result in a thin, boundary current of shelf waters that flow toward the terminus slightly below sill depth. Wind forcing amplifies the plume-driven exchange flow; however, wind-induced vertical mixing is limited to near-surface waters. Tidal mixing over the sill increases in-fjord transport of deep shelf waters and erodes basin stratification above the sill depth.

5.3 Future Work

The results from this dissertation provide a first-order framework for understanding circulation and submarine melt in high-latitude ocean-glacier systems. To move forward towards a unified understanding of the ocean's role in driving frontal ablation of termini, outlet glacier dynamics, and the large-scale behavior of ice sheets, improved cotemporaneous ocean-glacier observations, high-resolution coupled ocean-glacier numerical models, and parameterizations of outlet glacier fjords in large-scale climate models are needed. Several areas of future modeling work should include: 1) The development of high-resolution, eddy-resolving simulations (i.e., large eddy simulations) of the subglacial plume that include a three-dimensional melting terminus that can evolve in time. Model simulations could explore a range of terminus geometries (undercut and overcut), with a focus on identifying feedbacks between plume dynamics, melt rates, and terminus morphology. Additionally, these simulations could explore the influence of rotational effects, ice mélange, submarine sills, and subglacial sediment on plume dynamics.

2) The results from Chapter III could be expanded to include the 200+ outlet glacier

fjords in Greenland, with a focus on comparing modeled submarine melt rates to

observed glacier behavior.

  3.) The development of fjord-scale ocean models that include realistic bathymetry and

forcing (wind, tides, sea ice, and shelf boundary conditions). These realistic ocean models

could be coupled (offline or online) with glacier/ice sheet models to investigate ocean-

glacier feedbacks that may influence glacier retreat/advance.

4.) Simulations that investigate winter conditions, when subglacial discharge is inactive.

This work should build on previous efforts that explore the role of ambient

terminus/iceberg melt and sea ice dynamics in modulating fjord-scale circulation and

hydrography. Additionally, the results from this work could be extended to outlet glacier

systems where discharge is expected to be negligible year-round (i.e., the west Antarctic

Peninsula).

5.) Ocean state models are too coarse to resolve circulation and mixing processes in

fjords. To address this problem, it would be useful to develop new estuarine box model

parameterizations of fjord-glacier systems that can be employed in large-scale ocean/ice

sheet models. Ultimately, this work would connect the large-scale ocean circulation with

small-scale fjord dynamics, providing improved numerical methods for estimating how

ice loss and freshwater discharge from the Greenland Ice Sheet are influenced by changes

in the circulation of the North Atlantic Ocean.

6.) The incorporation of a biogeochemical/ecological model into the fjord-scale

simulations. This work would focus on the influence of glacially-modified waters on

near-shore and coastal nutrient concentrations and ecosystems.

APPENDIX A

SUPPLEMENTAL INFORMATION FOR CHAPTER III

This supplemental material was published in *Geophysical Research Letters* in October 2016.

Text S1. Spatially-averaged Melt Rate

To estimate the spatially-averaged melt rate across the Kangerdlugssup Sermerssua (KS) and Rink Isbræ (RI) termini, we combine the point source subglacial plume model with an ambient line plume model [Jenkins 2011]. The ambient plume model is used to estimate the so-called "background melt" in the region outside of the subglacial plume [Cowton et al., 2015]. The melt rate in the ambient model is calculated using the full three equation model [Holland and Jenkins, 1999] described in section 2. We initialize the ambient plume model with negligible subglacial discharge (10^{-6} m^2 s^{-1}), ensuring that the buoyancy flux of the ambient plume is dominated by submarine melting. We assume that the ambient plume is distributed evenly across the width of the terminus. The initial plume velocity (w_0) and thickness (r_0) are set by assuming a balance between buoyancy and momentum at the grounding line:

$$w_o = \left(\frac{g_0' Q_{sg}}{\alpha + C_d}\right)^{1/3},$$

$$r_o = \frac{Q_{sg}}{w_0},$$

where g_0' is the initial reduced gravity of the plume, Q_{sg} is the initial subglacial discharge flux, α is the entrainment constant, and C_d is the drag coefficient. All parameters follow values given in Jenkins [2011]. The initial plume temperature and salinity are set to the pressure-dependent melting point and 0, respectively.

We calculate total melt in the subglacial plume region (M_{plume}) as:

$$M_{plume} = N \int_{-gl}^{-mh} 2\, r\, smr_{plume}\, dz,$$

where N is the number of plumes, mh is the maximum rise height of the plume, gl is the grounding line depth, r is the plume radius, and smr_{plume} is the plume melt rate. We calculate total melt in the region outside the subglacial plume ($M_{ambient}$) as:

$$M_{ambient} = \int_{tw}^{0} \int_{-gl}^{0} smr_{ambient}\, dx\, dz - N \int_{-gl}^{-mh} 2\, r\, smr_{ambient}\, dz,$$

where tw is the terminus width and $smr_{ambient}$ is the ambient melt rate. The spatially-averaged melt rate across the terminus (M_{total}) is then calculated as:

$$M_{total} = \frac{M_{plume} + M_{ambient}}{A_{glacier}},$$

where $A_{glacier}$ is the surface area of the terminus.

We note that applying this method to Kangerdlugssup Sermerssua for a single plume results in peak spatially-averaged melt rates of 0.06 m day^{-1}, biased two orders of magnitude low compared to observations by Fried et al., [2015] (Figure S6). Increasing the number of subglacial conduits to 5 and 10 (while holding subglacial discharge fixed) results in spatially-averaged melt rates of 0.22 and 0.43 m day^{-1}, respectively, but still an order of magnitude lower than observed. This discrepancy arises because the ambient melt model assumes that the buoyancy flux of the plume is driven entirely by submarine melt, resulting in small vertical velocities and melt rates outside of the plume region. Finally, we use the line plume model of Jenkins [2011] to examine the case where the entire subglacial discharge flux is distributed evenly across the Kangerdlugssup Sermerssua terminus. This results in peak spatially-averaged melt rates of 1.42 m day^{-1}.

However, the line plume model results in a mean summer plume terminal level of 159 m, far deeper than the consistently observed near-surface plume at the Kangerdlugssup Sermerssua terminus [Fried et al., 2015; Bartholomaus et al., 2016).

Fried et al., [2015] hypothesize that along with several discrete conduits, subglacial discharge in Kangerdlugssup Sermerssua is distributed through many small sources along the termini, which could generate a number of weak plumes that increase melt far above ambient levels. This suggests that submarine melt in Kangerdlugssup Sermerssua may be driven by a heterogeneous combination of point source, line, and ambient melt plumes. We note that the submarine melt estimates from Fried et al., [2015] are depth-averaged and include large uncertainties from their data collection method. Increasing the thermal and haline Stanton numbers by an order of magnitude in the ambient melt model yields spatially-averaged melt rates on the same order as observations, however, it is unclear if this tuning is justified for Greenland's near vertical terminus geometry (Figure S6).

Text S2. Estimates of Grounding Line Depth

We show that plume melt rate is sensitive to both grounding line depth and ocean heat content. As such, it is imperative to have accurate estimates of grounding line depths, a quantity which is difficult to measure directly. Estimates used in this paper come from airborne radar, shipboard echosounders, and gravity-inversions (Table S2). The depth we use for Alison Glacier differs from published depths from Boghosian et al., [2015] by nearly 600 m. This much deeper grounding line comes from updated gravity-based bathymetries from D. Porter (pers. comm.) by incorporating additional offshore bathymetric data from Ocean Melting Greenland (OMG) echosounders, as uncertainty in

the inverted bathymetry is reduced when constrained with both offshore and sub-ice

topography. These much greater fjord depths are also supported by CTD data collected

in the region (D. Porter, pers. comm.).
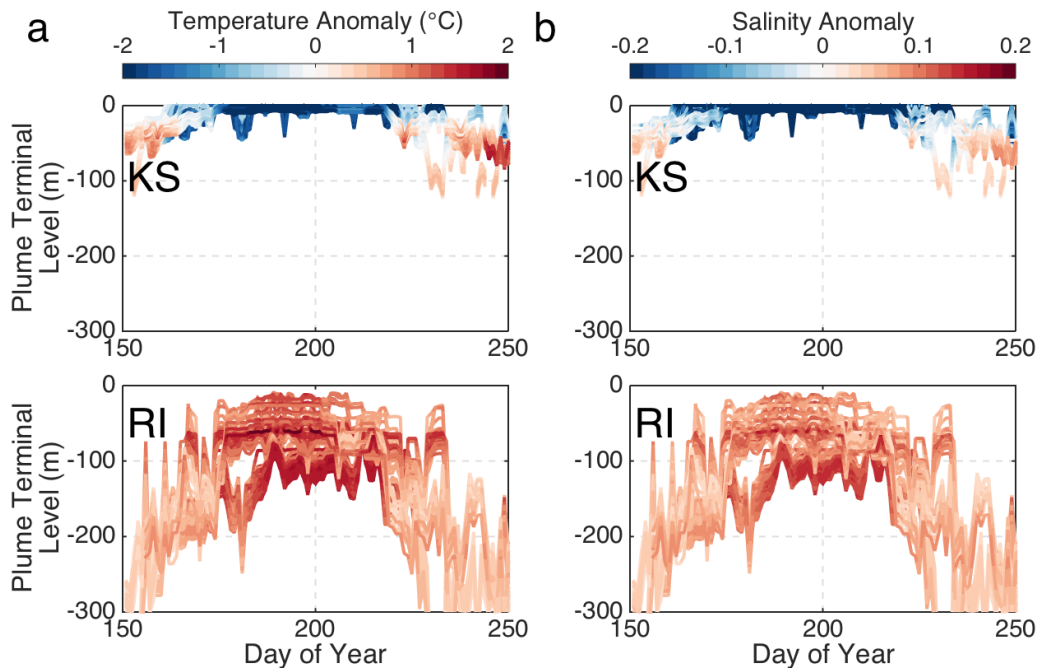
Figure S1. Seasonal modification of fjord waters at the plume terminal level. Time series of plume temperature **(a)** and salinity anomaly **(b)** with respect to ambient fjord waters at the terminal level for Kangerdlugssup Sermerssua (250 m grounding line depth) and Rink Isbræ (850 m grounding line depth) fjords during summer 2013-2015. All available hydrographic profiles are used.
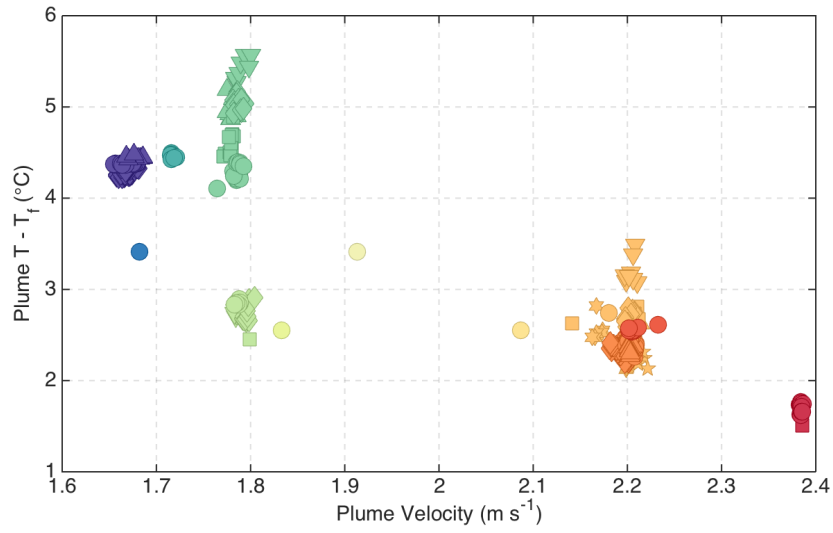
Figure S2. Plume vertical velocity and temperature above freezing point. Colors represent profiles in Figure 3a. Subglacial discharge is fixed at 250 m^3 s^{-1}, all properties are depth-averaged.
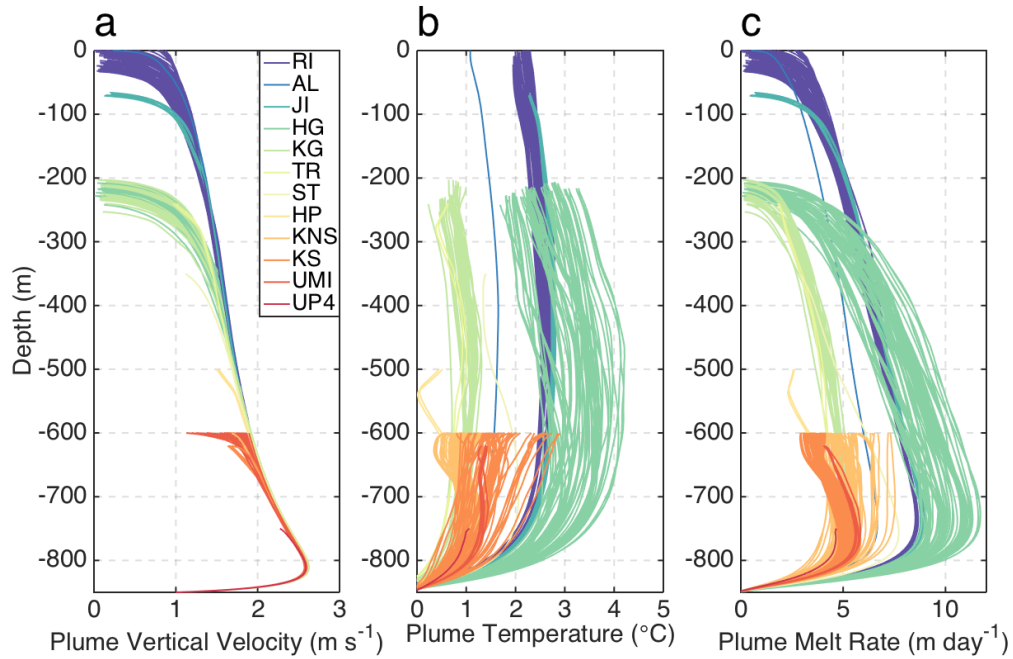
Figure S3. Vertical profiles of plume vertical velocity **(a)**, temperature **(b)** and melt rate **(c)** for all systems. Subglacial discharge is fixed at 250 m^3 s^{-1}, all available hydrographic profiles are used. The plume vertical velocity profile evolves similarly in all cases until the plume reaches its terminal level. However, the melt rate varies due to a combination of regional variability in ambient fjord temperature, plus the grounding line depth controlling which section of the ambient temperature stratification that the velocity profile interacts with.
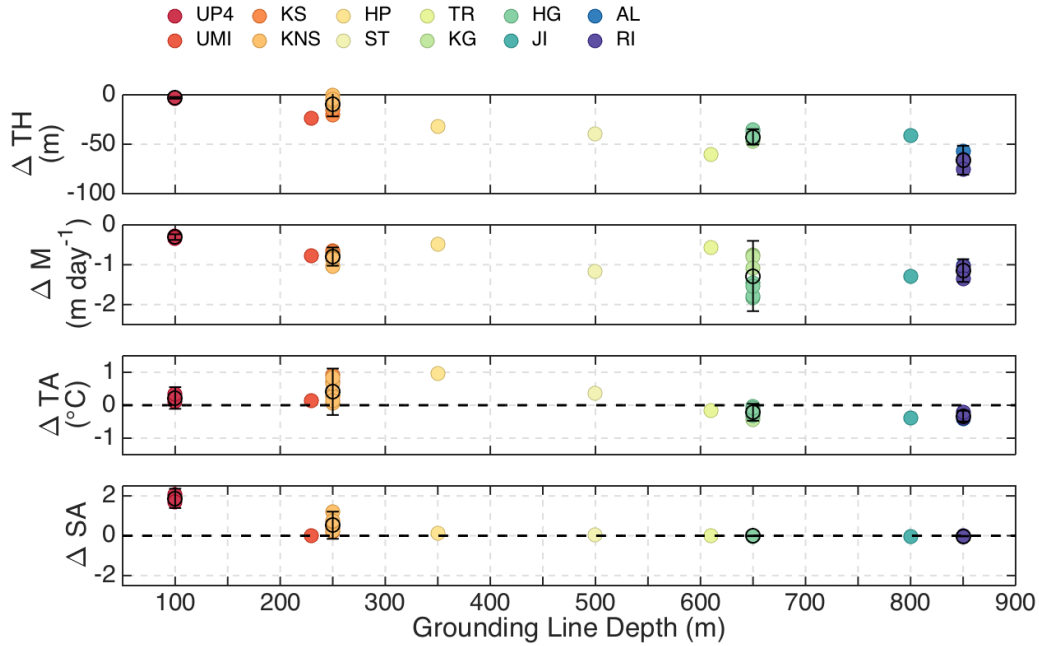
Figure S4. Change in mean summer plume terminal height (TH), depth-averaged melt rate (M), temperature anomaly (TA), and salinity anomaly (SA) when equivalent subglacial discharge is distributed from three conduits instead of a single conduit. We assume that conduits are spaced sufficiently apart so that plumes do not coalesce. Hydrographic profiles are averaged across each summer, temperature and salinity anomaly are taken with respect to ambient fjord waters at the terminal level. Error bars represent uncertainty (two standard deviations) due to variability in mean summer subglacial discharge and fjord stratification.
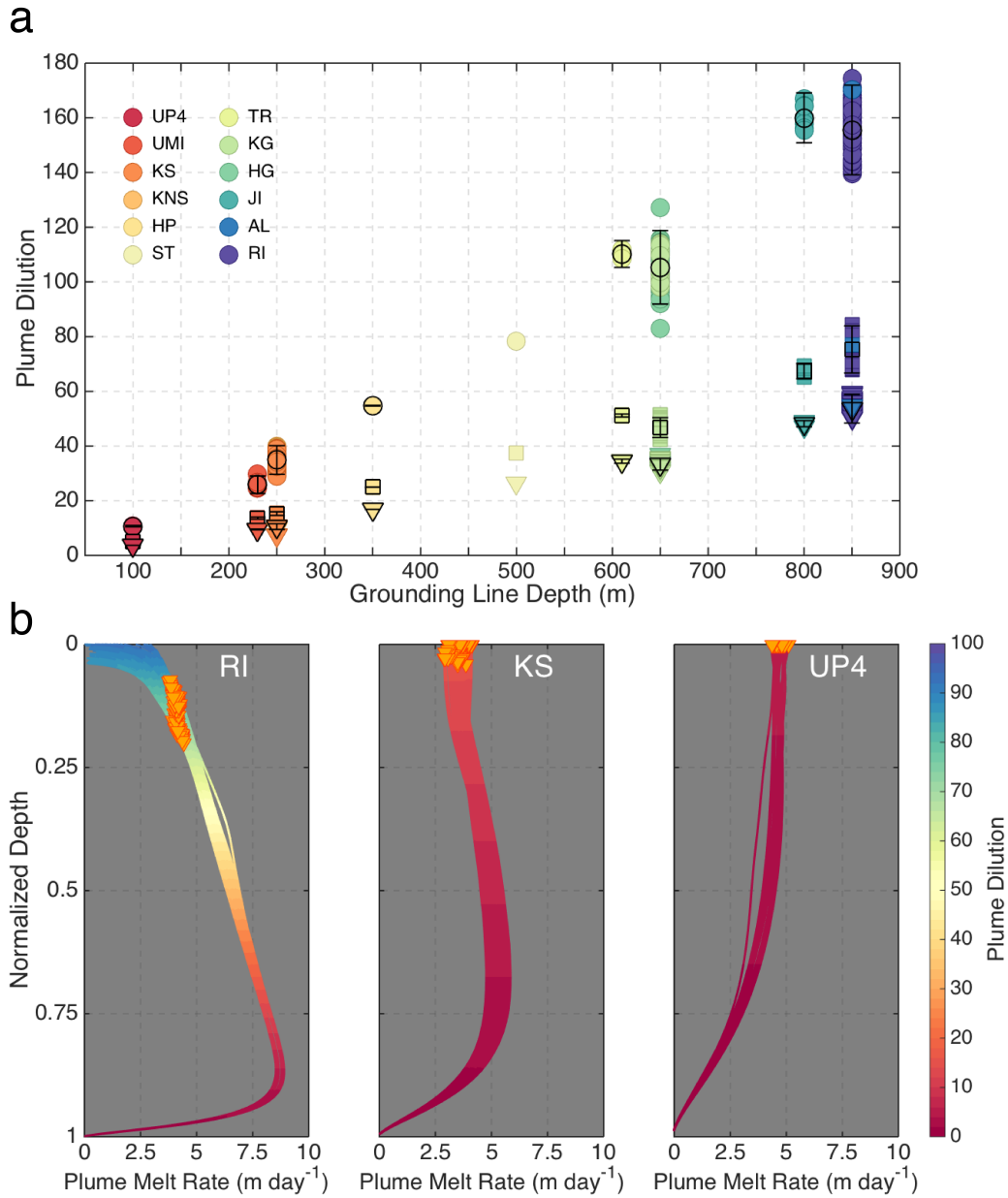
Figure S5. **(a)**, Plume dilution at the terminal level for subglacial discharges of 50 (circles), 250 (squares), and 500 (downward-pointing triangles) m^3 s^{-1}. Error bars represent uncertainty (two standard deviations) due to temporal and spatial variability in fjord stratification. All available hydrographic data for each system is shown. **(b)**, Vertical profiles of melt rate for Rink Isbræ (RI, 850 m), Kangerdlugssup Sermerssua (KS, 250 m), and Upernavik 4 (UP4, 100 m), representing our range of grounding line depths. Subglacial discharge is fixed at 250 m^3 s^{-1}, all available hydrographic data for each system is shown. Depth is normalized, colors represent plume dilution. Orange triangles represent the plume terminal level.
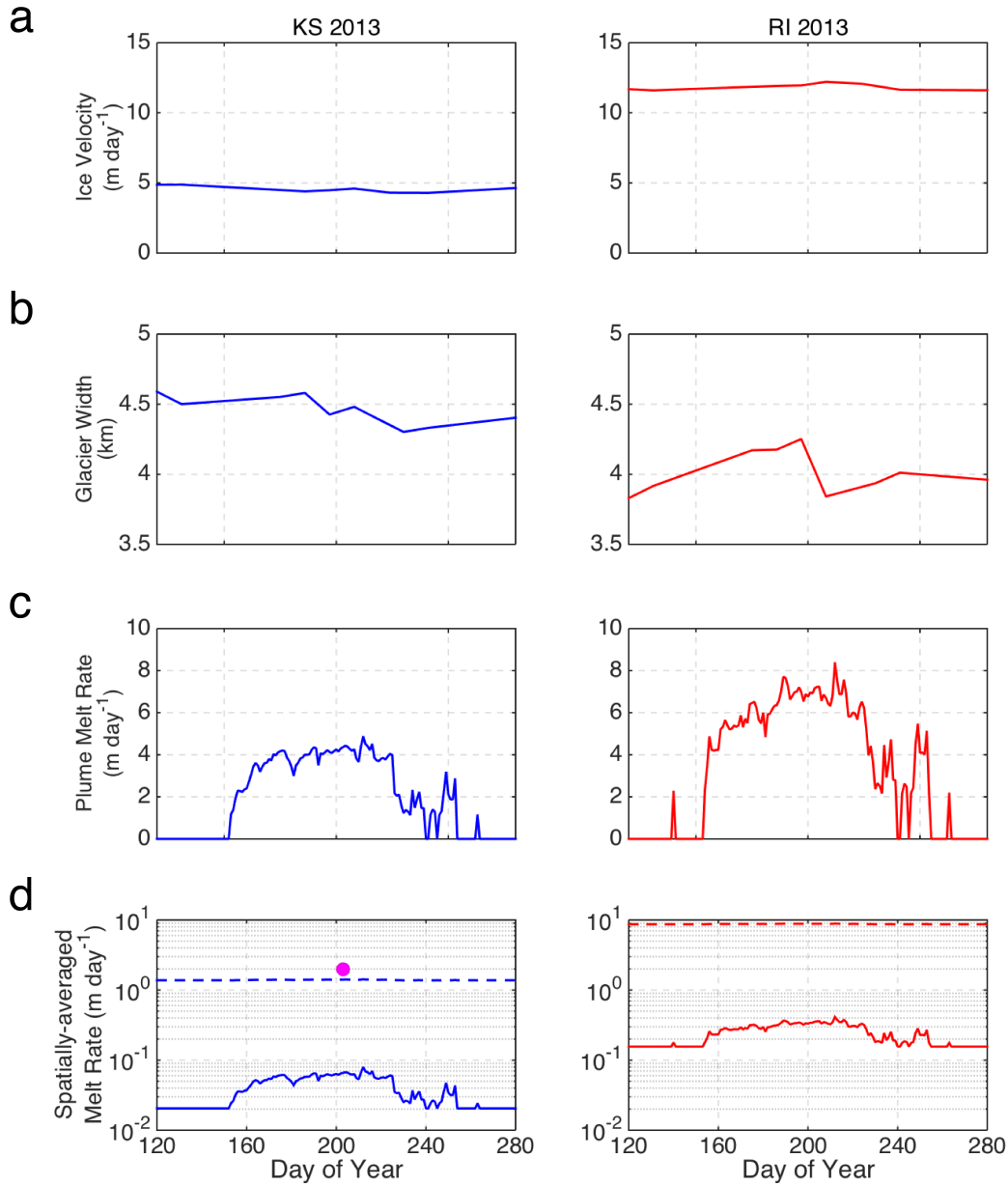
Figure S6. Spatially-averaged melt rate for Kangerdlugssup Sermerssua (KS) and Rink Isbræ (RI) during 2013. Ice velocity **(a)** and terminus width **(b)** from TerraSAR-X [Moon et al., 2014] and MEaSUREs Synthetic Aperture Radar mosaics [Moon and Joughin, 2008; Joughin and Moon, 2015]. **c**, Depth-averaged melt rate in the subglacial plume, hydrographic profiles are averaged across the summer. **d**, Solid line shows spatially-averaged melt rate (subglacial plume and ambient melt) across the terminus, dashed line shows effect of increasing thermal and haline Stanton numbers by an order of magnitude. Magenta dot is estimate of spatially-averaged submarine melt in KS from Fried et al., [2015].
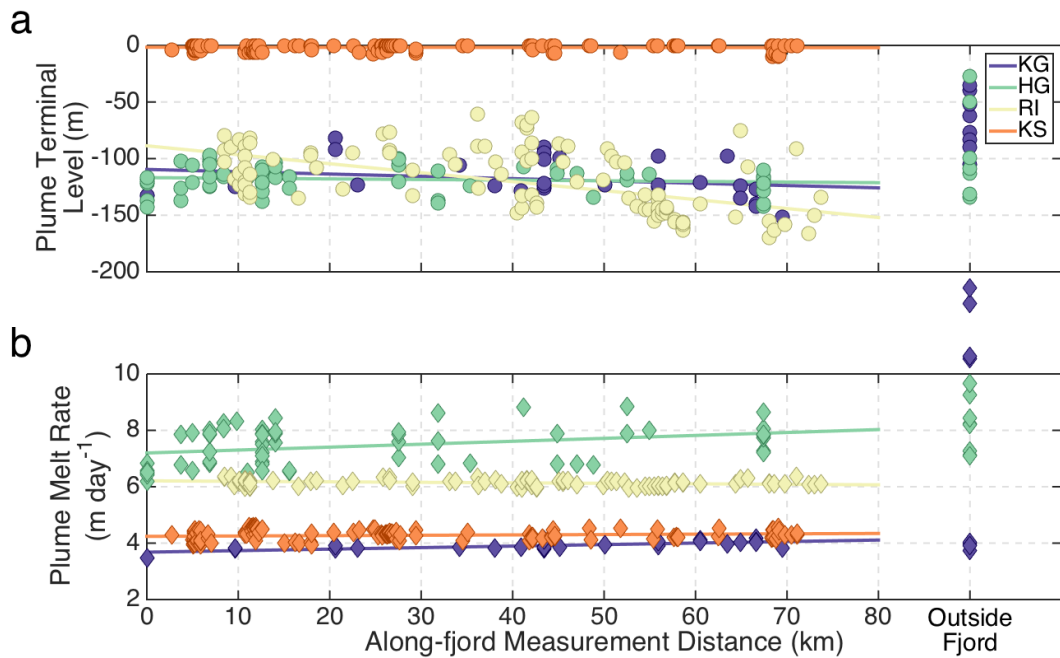
Figure S7. Sensitivity of plume properties to along-fjord measurement location. Plume terminal level **(a)** and depth-averaged melt rate **(b)** vs. along-fjord measurement distance along the thalweg. All available hydrographic data for Kangerdlugssuaq (KG), Helheim (HG), Rink Isbræ (RI), and Kangerdlugssup Sermerssua (KS) are shown, subglacial discharge is fixed at 250 m^3 s^{-1}. Along-fjord measurement distance in KG and HG begins at the seaward edge of the ice mélange, RI and KS begin at the terminus. Solid lines represent linear fits to profiles inside fjord. Profiles from the shelf outside KG and HG are shown on the far right.
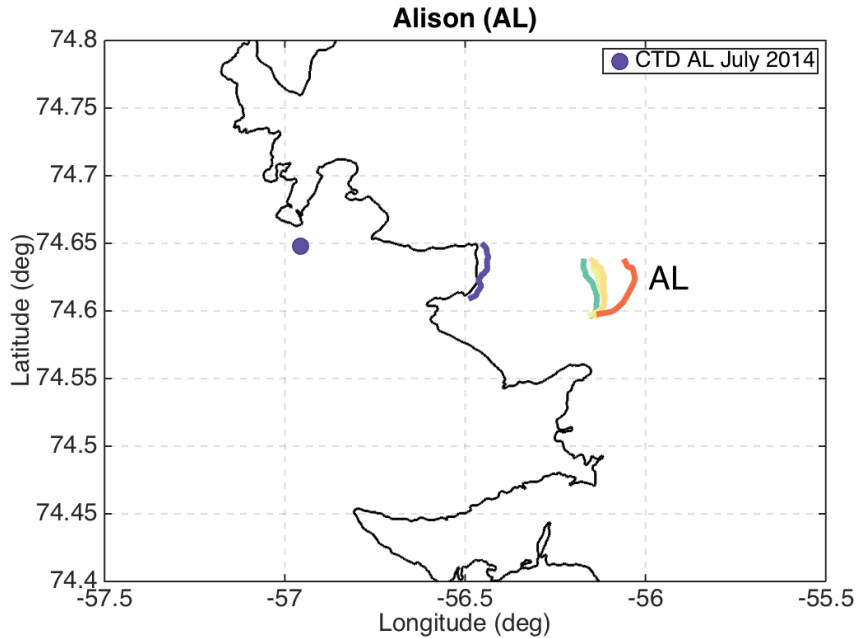
Figure S8: CTD location for Alison (AL). Colored lines represent winter terminus position from 2000-2001, 2005-2006, 2006-2007, 2007-2008, 2008-2009, and 2012-2013 from Joughin and Moon, [2015]. Terminus positions are colored in chronological order from cool to warm colors.
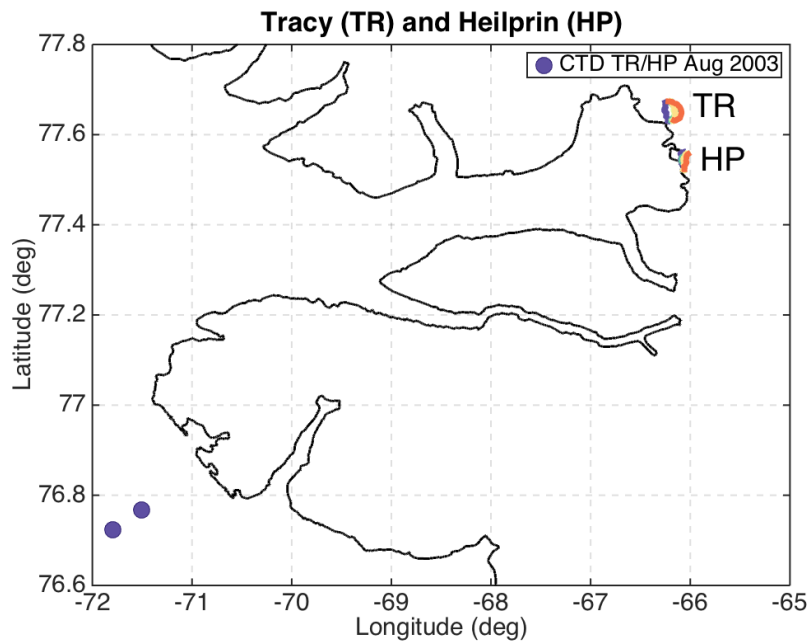
Figure S9: CTD locations for Tracy (TR) and Heilprin (HP). Colored lines represent winter terminus position from 2000-2001, 2005-2006, 2006-2007, 2007-2008, 2008-2009, and 2012-2013 from Joughin and Moon, [2015]. Terminus positions are colored in chronological order from cool to warm colors.

Figure S10: CTD locations for Helheim (HG). Downward-pointing triangles represent "outside fjord" profiles used in Figure S7. Colored lines represent winter terminus position from 2000-2001, 2005-2006, 2006-2007, 2007-2008, 2008-2009, and 2012-2013 from Joughin and Moon, [2015]. Terminus positions are colored in chronological order from cool to warm colors.

Figure S11: CTD locations for Jakobshavn (JI). Downward-pointing triangles represent "outside fjord" profiles shown in Figure S6. Colored lines represent winter terminus position from 2000-2001, 2005-2006, 2006-2007, 2007-2008, and 2012-2013 from Joughin and Moon, [2015]. Terminus positions are colored in chronological order from cool to warm colors.

Figure S12: CTD locations in fjord **(a)** and shelf **(b)** for Kangerdlugssuaq (KG). Downward-pointing triangles in panel b represent "outside fjord" profiles used in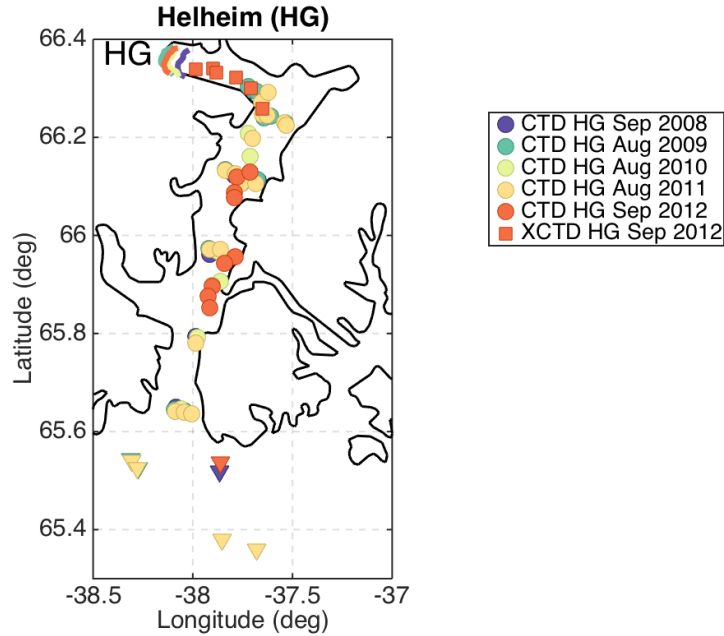 Figure S7. Colored lines represent winter terminus position from 2000-2001, 2005-2006, 2006-2007, 2007-2008, 2008-2009, and 2012-2013 from Joughin and Moon, [2015]. Terminus positions are colored in chronological order from cool to warm colors.
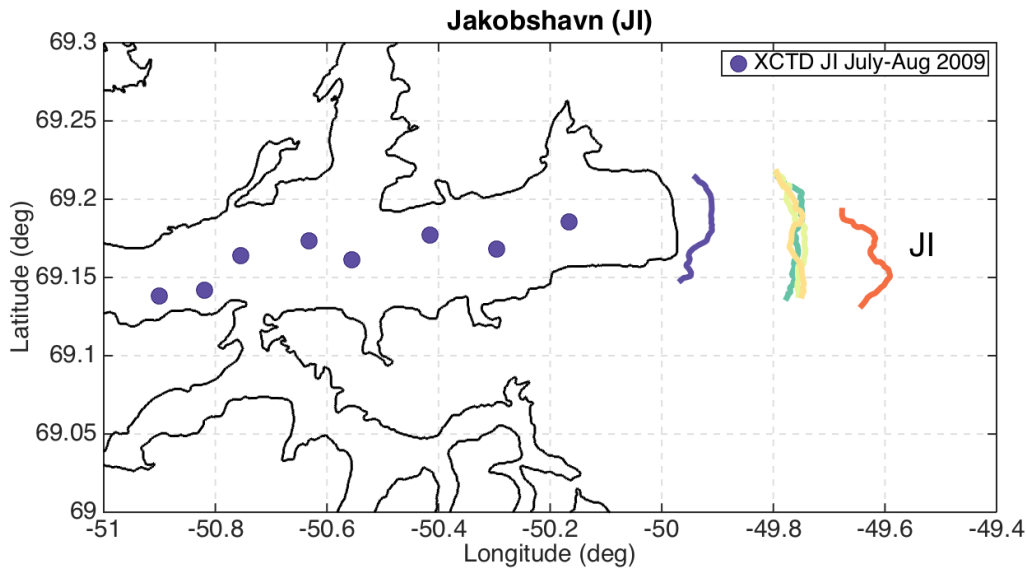
Figure S13: CTD locations for Kangiata Nunata Sermia (KNS). Colored lines represent winter terminus position from 2000-2001, 2005-2006, 2006-2007, 2007-2008, 2008-2009, and 2012-2013 from Joughin and Moon, [2015]. Terminus positions are colored in chronological order from cool to warm colors.

Figure S14: CTD locations for Umiamako (UMI), Rink Isbræ (RI), and Kangerdlugssup Sermerssua (KS). Colored lines represent winter terminus position from 2000-2001, 2005-2006, 2006-2007, 2007-2008, 2008-2009, and 2012-2013 from Joughin and Moon, [2015]. Terminus positions are colored in chronological order from cool to warm colors.
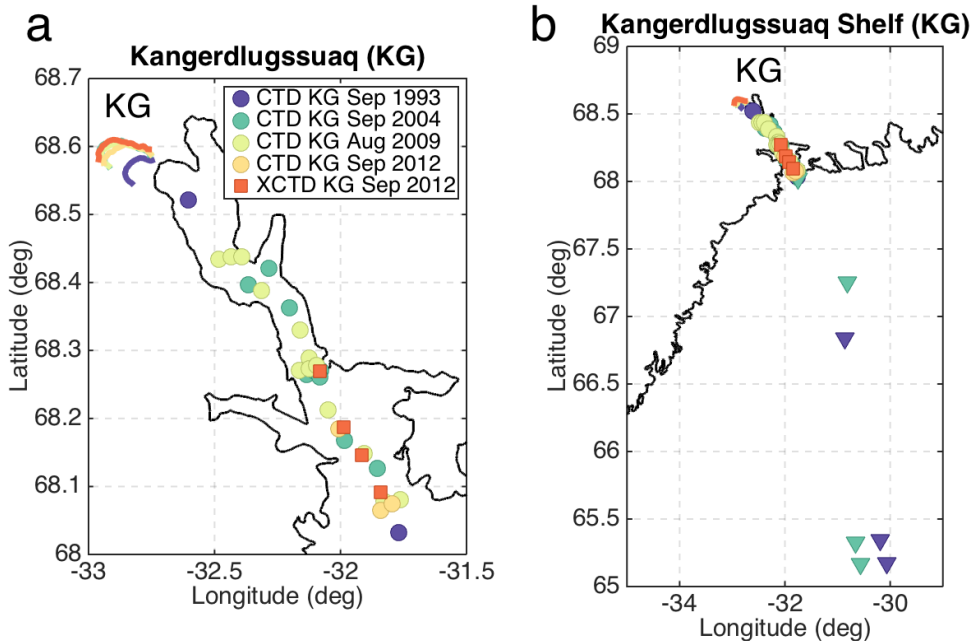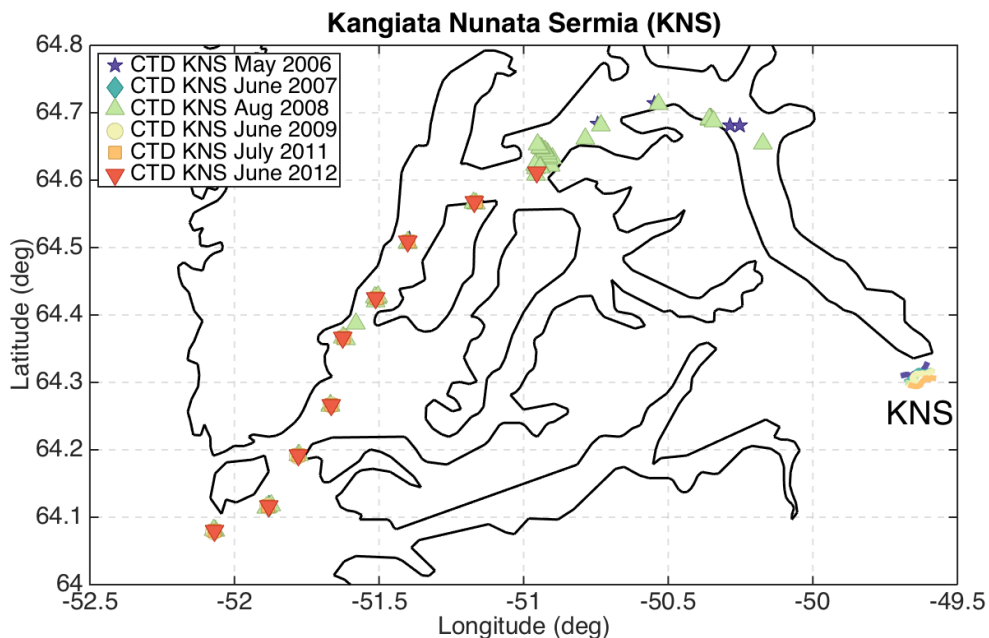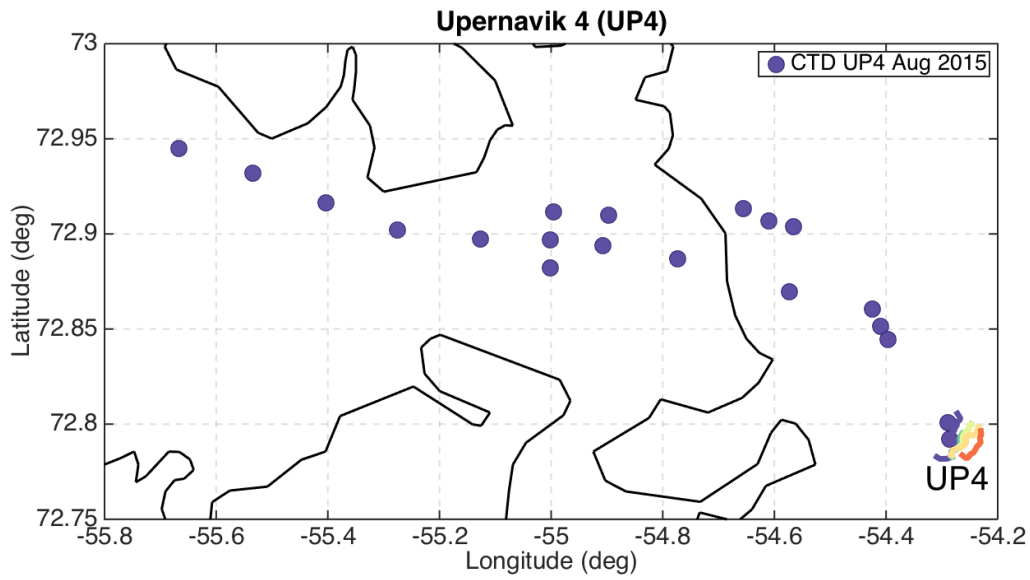
Figure S15: CTD locations for Upernavik 4 (UP4). Colored lines represent winter terminus position from 2000-2001, 2005-2006, 2006-2007, 2007-2008, 2008-2009, and 2012-2013 from Joughin and Moon, [2015]. Terminus positions are colored in chronological order from cool to warm colors.
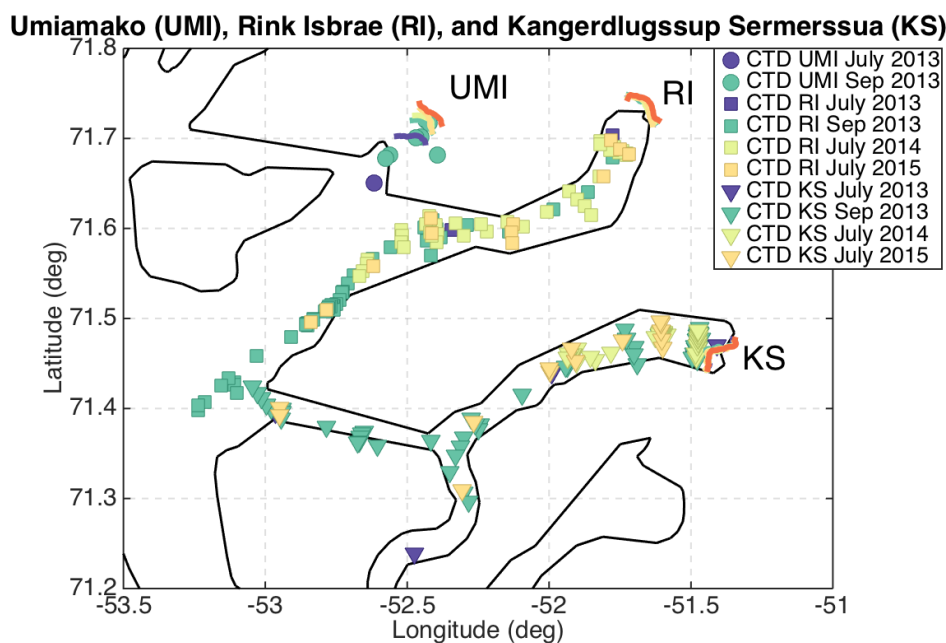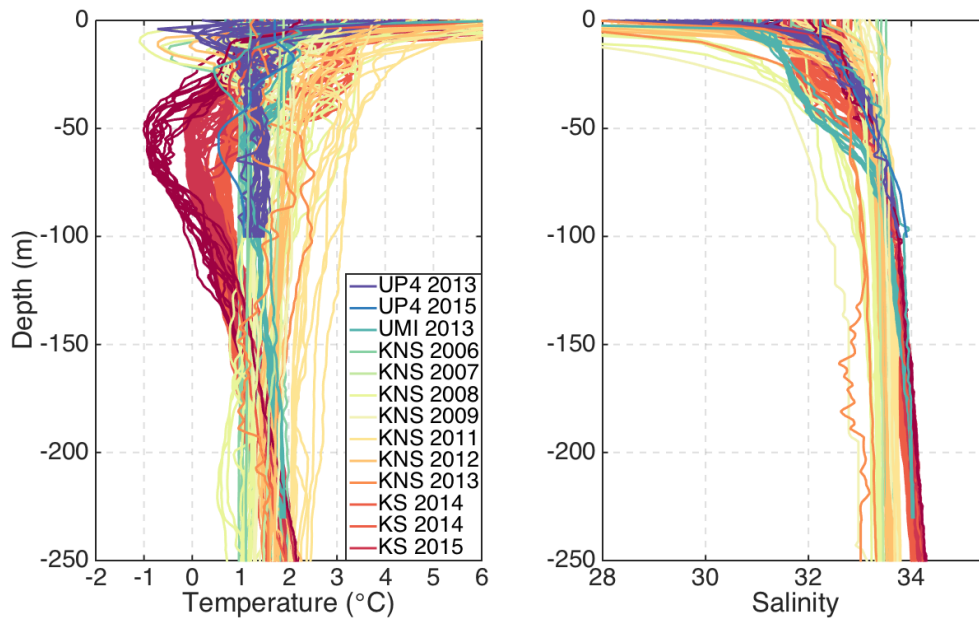

Figure S16: Ambient temperature and salinity profiles for all systems with grounding line depths ranging from 100 - 250 m.
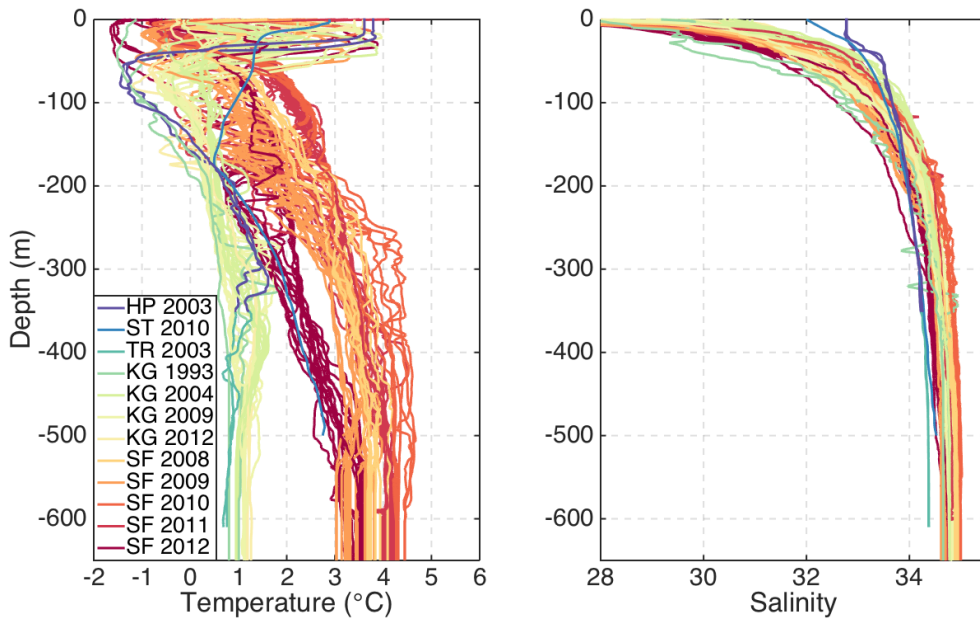
Figure S17: Ambient temperature and salinity profiles for all systems with grounding line depths ranging from 350 - 650 m.
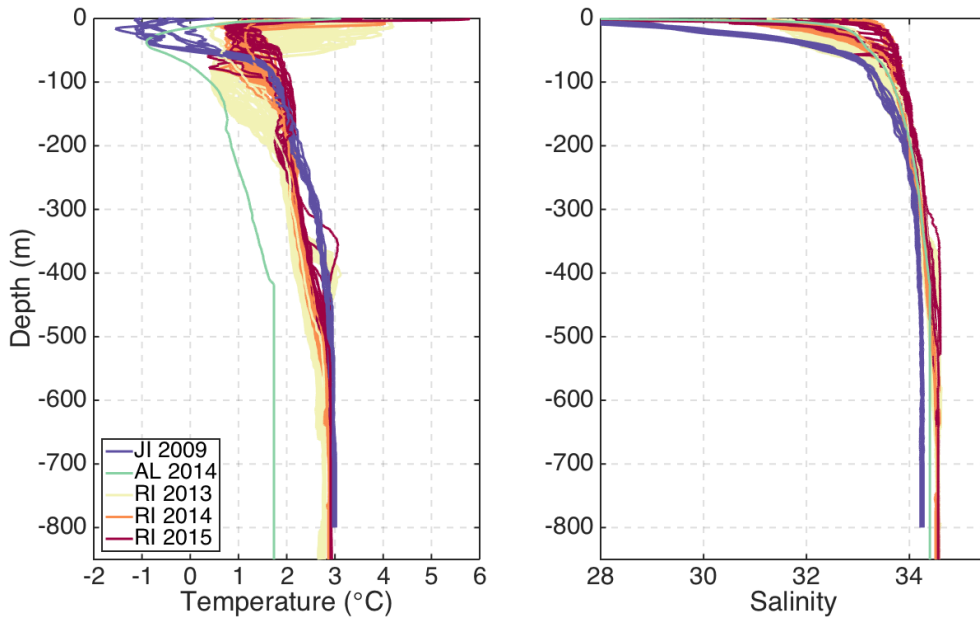
Figure S18: Ambient temperature and salinity profiles for all systems with grounding line depths ranging from 800 - 850 m.

Glacier Name	Date	CTD Location	Casts Used	Data Source	Reference
Alison **(AL)**	July 2014	Figure S7	1	D. Porter, pers. comm.	
Heilprin **(HP)**	Aug 2003	Figure S8	2	Canadian Archipelago Throughflow Study, https://www.aoncadis.org/dataset/Healy2003-01-CTD.html	Porter et al., 2014; Münchow et al., 2007, 2015
Helheim **(HG)**	Sep 2008	Figure S9	7	F. Straneo, pers. comm.	Straneo et al., 2010
Helheim **(HG)**	Aug 2009	Figure S9	14	F. Straneo, pers. comm.	Straneo et al., 2011, 2012; Sutherland et al. 2012, 2014
Helheim **(HG)**	Aug 2010	Figure S9	7	F. Straneo, pers. comm.	
Helheim **(HG)**	Aug 2011	Figure S9	20	F. Straneo, pers. comm.	
Helheim **(HG)**	Sep 2012	Figure S9	15	F. Straneo, pers. comm.	
Jakobshavn **(JI)**	July-Aug 2009	Figure S10	8	F. Straneo, per. communication	Straneo et al. 2012; Gladish et al. 2015a,b
Kangerdlugssuaq **(KG)**	Sep 1993	Figure S11	2	Global Seawater Oxygen-18 Database - v1.21 http://data.giss.nasa.gov/o18data/	Azetsu-Scott and Tan, 1997; Christoffersen et al., 2011
Kangerdlugssuaq	Sep 2004	Figure S11	9	British Antarctic Survey, R/V James	Christoffersen

(KG)				Clark Ross cruise #106	et al., 2011
Kangerdlugssuaq **(KG)**	Aug 2009	Figure S11	13	F. Straneo, pers. comm.	Straneo et al., 2012; Sutherland et al., 2014
Kangerdlugssuaq **(KG)**	Sep 2012	Figure S11	7	F. Straneo, pers. comm.	
Kangiata Nunata Sermia **(KNS)**	May 2006	Figure S12	13	Danish Meteorological Institute, cruise 26AJ	
Kangiata Nunata Sermia **(KNS)**	June 2007	Figure S12	1	Danish Meteorological Institute, cruise 26A3	
Kangiata Nunata Sermia **(KNS)**	Aug 2008	Figure S12	34	Danish Meteorological Institute cruise 26DA	
Kangiata Nunata Sermia **(KNS)**	June, Sep 2009	Figure S12, Mortensen et al., 2013 (Figure 1)	6,1	Danish Meteorological Institute, cruise 26TU; digitized	Mortensen et al., 2013
Kangiata Nunata Sermia **(KNS)**	July 2011	Figure S12	8	Danish Meteorological Institute, cruise 26TU	
Kangiata Nunata Sermia **(KNS)**	June 2012	Figure S12	9	Danish Meteorological Institute, cruise 26TU	
Kangiata Nunata Sermia **(KNS)**	Aug 2013	Bendtsen et al., 2015 (Figure 1a)	2	Digitized	Bendtsen et al., 2015

Kangerdlugssup Sermerssua **(KS)**	July 2013, Sep 2013	Figure S13	5,63	R/V Sanna Cruise	Bartholomaus et al., 2016
Kangerdlugssup Sermerssua **(KS)**	July, Aug 2014	Figure S13	68	R/V Sanna Cruise	Bartholomaus et al., 2016
Kangerdlugssup Sermerssua **(KS)**	July 2015	Figure S13	14	R/V Sanna cruise	
Rink Isbræ **(RI)**	July 2013, Sep 2013	Figure S13	2,56	R/V Sanna Cruise	Bartholomaus et al., 2016
Rink Isbræ **(RI)**	July, Aug 2014	Figure S13	49	R/V Sanna Cruise	Bartholomaus et al., 2016
Rink Isbræ **(RI)**	July 2015	Figure S13	12	R/V Sanna cruise	
Store **(ST)**	Aug 2010	Xu et al., 2013 (Figure 1a)	1	Digitized	Xu et al., 2013
Tracy **(TR)**	Aug 2003	Figure S8	2	Canadian Archipelago Throughflow Study, https://www.aoncadis.org/dataset/Healy2003-01-CTD.html	Porter et al., 2014; Münchow et al., 2007, 2015
Umiamako **(UMI)**	July, Sep 2013	Figure S13	1,9	R/V Sanna Cruise	Bartholomaus et al., 2016
Upernavik 4 **(UP4)**	Aug 2013	Andresen et al., 2014 (Figure 1)	1	Digitized	Andresen et al., 2014
Upernavik 4 **(UP4)**	Aug 2015	Figure S14	20	S/Y Ivilia Cruise	

Table S1. List of all hydrographic observations.

Glacier Name	Mean Grounding Line Depth (m)	Reference
Upernavik 4 **(UP4)**	100	Morlighem et al., 2014; Andresen et al., 2014
Umiamako **(UMI)**	230	Bartholomaus et al., 2016; Rignot et al., 2016a
Kangiata Nunata Sermia **(KNS)**	250	Mortensen et al. 2013; Bendtsen et al., 2015
Kangerdlugssup Sermerssua **(KS)**	250	Bartholomaus et al., 2016; Rignot et al., 2016a
Heilprin **(HP)**	350	Porter et al., 2014
Store **(ST)**	500	Xu et al., 2013; Chauché et al., 2014, Rignot et al., 2015,2016a
Tracy **(TR)**	610	Porter et al., 2014
Helheim **(HG)**	650	Straneo et al., 2012
Kangerdlugssuaq **(KG)**	650	Straneo et al., 2012
Jakobshavn **(JI)**	800	Holland et al., 2008; Straneo et al., 2012; Gladish et al., 2015
Alison **(AL)**	850	D. Porter, pers. comm.
Rink Isbræ **(RI)**	850	Dowdeswell et al., 2013; Ó Cofaigh et al., 2013; Chauché et al., 2014; Rignot et al., 2015,2016a; Bartholomaus et al., 2016

Table S2. List of mean grounding line depths for all modeled systems.

Glacier Group	Subglacial Discharge (m^3 s^{-1})	Slope (a)	y-intercept (b)
G1	50	0.4278	2.0296
G2	50	0.2804	2.0898
G3	50	0.2308	1.439
G4	50	0.0846	2.5951
G1	250	0.5385	2.3094
G2	250	0.4212	2.8094
G3	250	0.3351	2.2020
G4	250	0.1731	3.1780
G1	500	0.5683	2.2868
G2	500	0.4851	3.0636
G3	500	0.3971	2.5309
G4	500	0.2347	3.3379

Table S3. Linear fit of depth-averaged plume melt rate to ocean heat content. $\dot{m}$ = a*OHC + b. Group G1 = UP4, Group G2 = UMI, KS, KNS, Group G3 = KG, HG, and Group G4 = RI, AL, JI. Shaded rows correspond to characteristic lines shown in Figure 3a. HP, ST, and TR are not included in the groupings as these systems did not have sufficient hydrographic data to compute robust slopes.

APPENDIX B

SUPPLEMENTAL INFORMATION FOR CHAPTER IV

This supplemental information was submitted to the *Journal of Geophysical Research: Oceans* in April 2017.

Text S1. Momentum Balance

Diagnosing the along- and cross-fjord momentum budget in the narrow and wide fjord (W = 2 and 10 km) lends insight into the dynamics of the exchange flow (Figure S2). Here we focus on the sill-glacier geometry employed in Figures 7-9 ($H_{gl} / H = 1$ and $H_s / H = 0.5$). For a fjord width of 2 km (dashed line) and 5 km (not shown), the along-fjord momentum balance in the plume and return flow is primarily between the pressure gradient and viscosity (Figure S2a,b). Smaller contributions from along-fjord nonlinear advection and Coriolis acceleration are present in the plume and increase toward the north wall; these terms are negligible in the return flow. The cross-fjord plume and return flow momentum balance in the narrowest case is approximately geostrophic with maxima in the Coriolis and pressure gradient terms near the fjord centerline (i.e., $y / W \sim 0.5$) (Figure S2c,d). As the fjord width increases to 10 km (solid line), the along-fjord momentum balance exhibits more complex spatial structure and balance (Figure S2a,b). In the plume, the dominant along-fjord geostrophic terms are largest below the fjord centerline, with the ageostrophic balance between smaller advective and viscous terms. Above y / W ~ 0.6, the ageostrophic balance dominates, peaking near the north wall. The cross-fjord balance in the plume is primarily geostrophic and oppositely directed above and below the fjord centerline, with a small contribution from nonlinear advection in the plume core at $y / W \sim 0.8$ (Figure S2c). Both along- and cross-fjord momentum budgets

are approximately geostrophic in the return flow, with peak magnitudes occurring

between $y / W = 0.3$-0.4 (Figure S2b,d). For the equivalent fjord width, the along- and

cross-fjord plume and return flow momentum budget for the shallow grounding line case

(i.e., surface-confined plume) is also dominated by the pressure gradient and Coriolis

terms, albeit with larger contributions from the viscous and nonlinear terms (not shown).

Text S2. Effect of Forcing on Hydrography

We summarize the effect of vertical plume, tide, and wind forcing on fjord

hydrography for both shallow and deeply-grounded glaciers (Figure S4). Subglacial

discharge emerging from a shallow grounding line results in a cold, fresh surface-

confined plume (red line), pulling near-surface potential temperature/salinity (θ-S)

downward towards the runoff line (Figure S4a). A deep grounding line produces a warm,

salty subsurface plume that pulls θ-S in the upper 110 m upward toward the runoff line

(Figure S4b). Simulations with vertical plume and tidal forcing (blue lines) show that

tide-sill interactions result in significant mixing at depth, eroding ambient stratification in

the upper 200 m. In contrast, wind forcing events (green and purple lines) have a limited

effect on deep fjord hydrography, with mixing primarily confined to the upper 75 m of

the water column. In the shallow grounding line case, wind-driven mixing of near-surface

waters alters the ambient waters entrained in the vertical plume, resulting in cooler,

fresher plume waters (Figure S4a). For the deep glacier, wind forcing pulls θ-S in the

near-glacier plume upward and along-isopycnal toward the runoff line between 75 and

200 m depth, with a slight increase in salinity and cooling in near-surface waters (Figure

S4b).
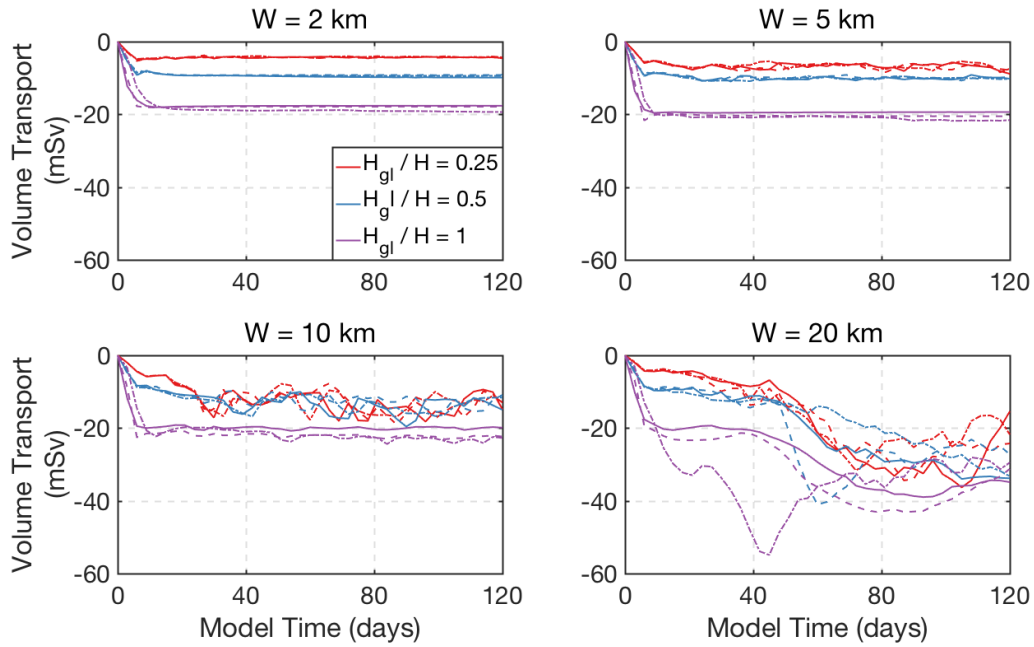
Figure S1. Transient evolution of volume transport at the fjord mouth for varying sill, fjord, and glacier geometry. Volume transports are time averaged into 3-day bins. Colors represent grounding line depth. Dashed-dot line represents $H_s / H = 0.25$, dashed line represents $H_s / H = 0.5$, and solid line represents $H_s / H = 1$, respectively.
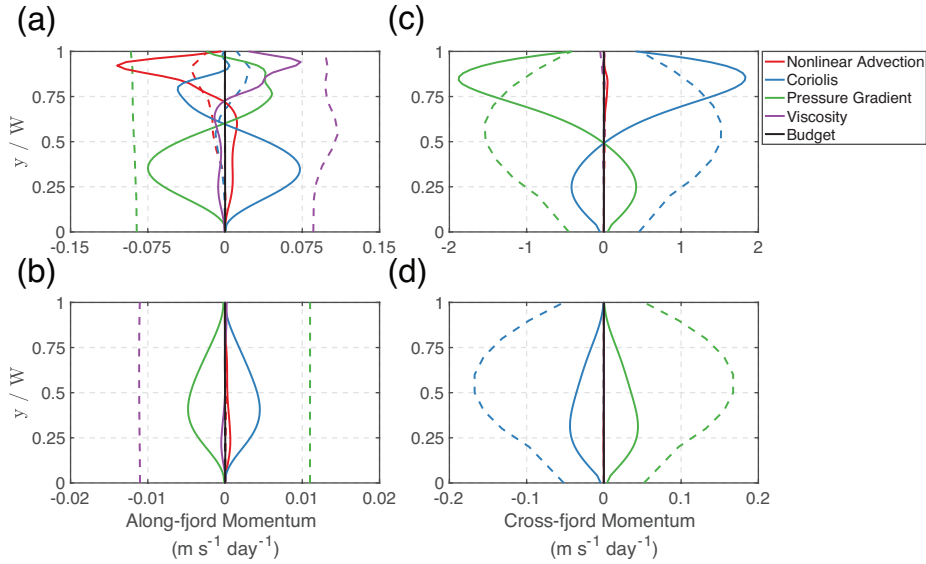
Figure S2. Along- and cross-fjord momentum budget for the plume (a,c) and depth-averaged return flow (b,d) as a function of normalized cross-fjord position. Sill-glacier geometry corresponds to $H_s / H = 0.5$, $H_{gl} / H = 1$; subglacial discharge flux is 250 m^3 s^{-1}. Dashed line represents fjord width of 2 km, solid line is 10 km. Terms shown are: nonlinear advection (red), Coriolis (blue), pressure gradient (green), viscosity (purple), and budget (black). Budget represents the sum of terms in the momentum equation. Momentum terms are averaged over day 90 to 120 and evaluated 15 km downstream of the glacier (x = -15 km). Momentum terms in the plume and return flow are computed at z = -45 m and depth-averaged between the sill and basin depth, respectively. Note the different scales used on the x-axis.
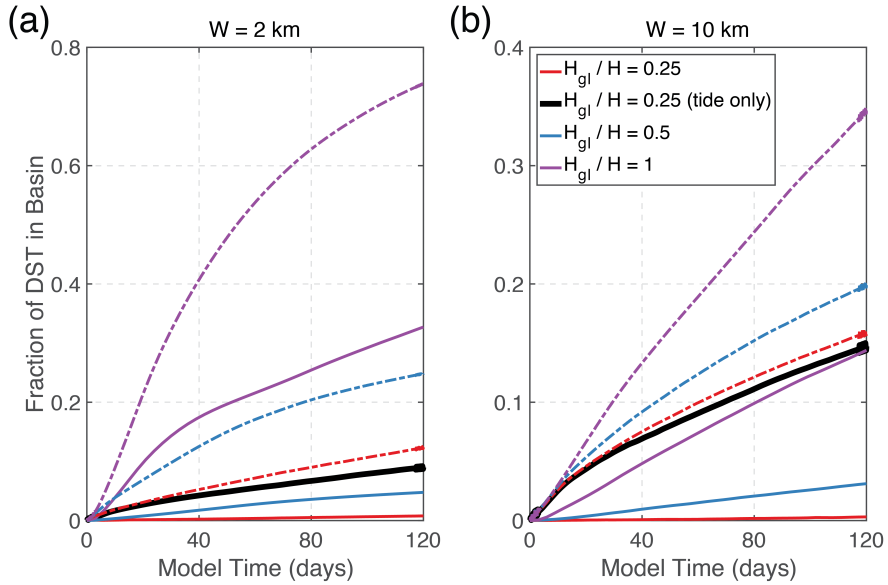
Figure S3. Temporal evolution of DST fraction in the fjord basin for varying fjord-glacier geometry and forcing. Sill geometry corresponds to $H_s / H = 0.25$; subglacial discharge flux is 250 m^3 s^{-1}. Solid colored lines show simulations with plume forcing only, colors represent grounding line depth. Thick solid black line shows simulations with only tidal forcing, and dashed lines show simulations with both vertical plume and tidal forcing. Simulations that include tidal forcing are filtered with a Godin filter. Note the different scales used on the y-axis.
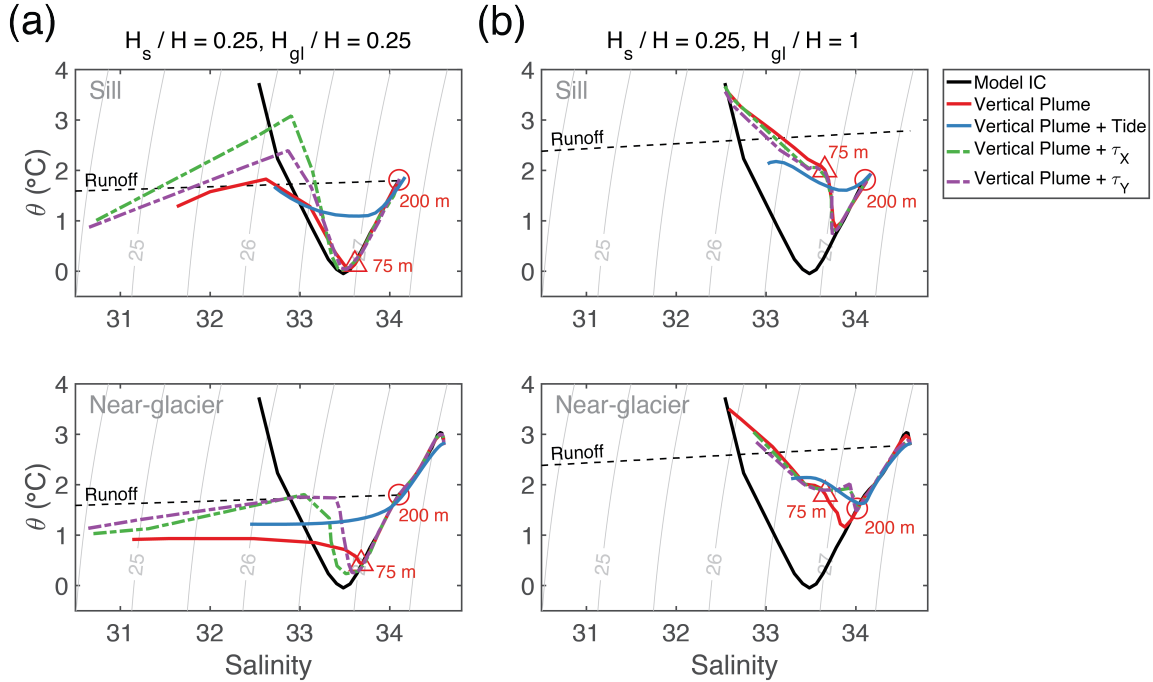
Figure S4. Mean potential temperature-salinity profiles at the sill crest and 5 km down-glacier for shallow (a) and deep (b) grounding lines with varied forcing. Fjord width is 10 km; all profiles are averaged in the cross-fjord direction. Simulations with tidal forcing are filtered with a Godin filter, vertical plume and vertical plume and tidal forcing simulations are averaged over day 84 to 114 (to account for Godin filter window). Vertical plume and three day along-fjord (τ_X) and along-shelf wind stress (τ_Y) simulations are averaged over day 150 to 160. Black dashed line represents the mixing line between initial fjord hydrography at the grounding line depth and subglacial discharge (i.e., runoff line). Gray contours represent isopycnals spaced at 0.5 kg m^{-3} intervals; open red triangles and circles show -75 m and the sill depth ($z = -200$ m) for the vertical plume case, respectively.
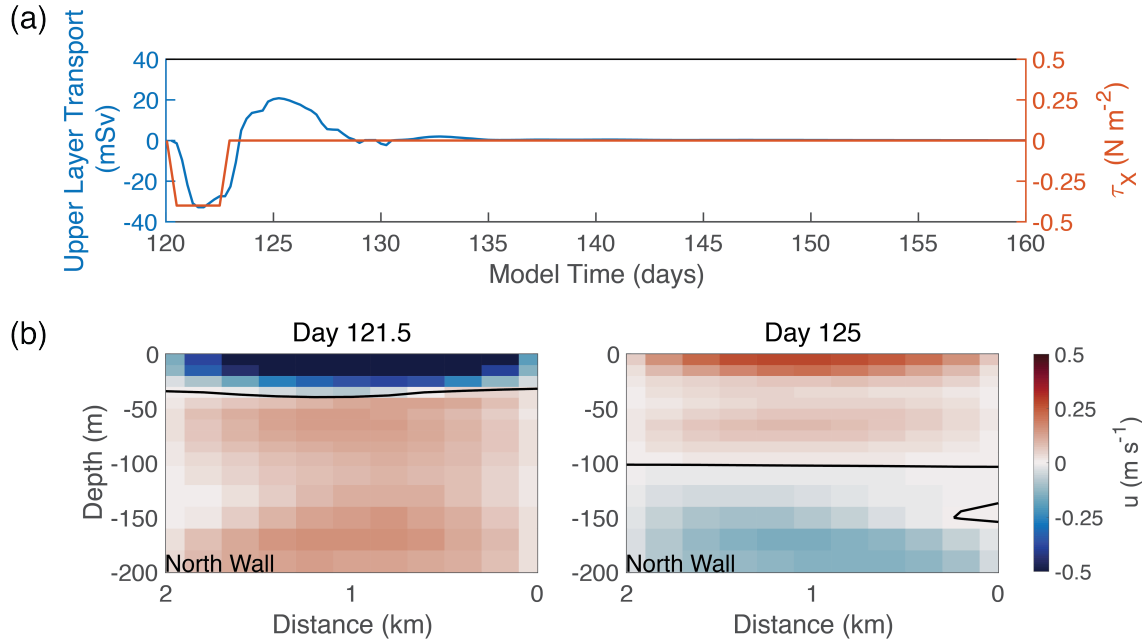
Figure S5. Upper layer volume transport (a) and cross-section of along-fjord velocity (b) for a three day along-fjord wind stress (τ_X) simulation. Fjord width is 2 km; sill-glacier geometry corresponds to $H_s / H = 0.25$, $H_{gl} / H = 0.25$. subglacial discharge flux is 0 m³ s⁻¹ (i.e., wind forcing only). Upper layer volume transport is computed across the fjord as the integrated transport from the free surface to the depth of the first zero crossing in along-fjord velocity. Shaded colors in (b) represent along fjord velocity; black contours represent zero.

Movie S1. 3-D visualization of sill-tide interactions for a fjord width of 2 and 10 km. Sill-glacier geometry corresponds to $H_s / H = 0.25$, $H_{gl} / H = 0.25$; subglacial discharge flux is 250 m³ s⁻¹. Colored slices represent along-fjord velocity (color scale ranges from -0.1 to 0.1 m s⁻¹). Blue and magenta colors represent plume and DST tracer concentrations of 0.1, respectively.

Movie S2. Plan view of simulation shown in Movie S1.

REFERENCES CITED

CHAPTER II

Andersen, M. L., and Coauthors, 2010: Spatial and temporal melt variability at Helheim Glacier, East Greenland, and its effect on ice dynamics. *J. Geophys. Res.: Earth Surf.*, **115**, F04041.

Ansong, J. K., P. J. Kyba, and B. R. Sutherland, 2008: Fountains impinging on a density interface. *J. Fluid Mech.*, **595**, 115–139.

Arakawa, A., and V. R. Lamb, 1977: Computational design of the basic dynamical processes of the UCLA general circulation model. *Advances in Research and Applications*, J. Chang, Eds., Methods in Computational Physics Series, Vol. 17, Elsevier, 173–265.

Arakeri, J. H., D. Das, and J. Srinivasan, 2000: Bifurcation in a buoyant horizontal laminar jet. *J. Fluid Mech.*, **412**, 61–73.

Burden, R. L., and J. D. Faires, 2010: Numerical analysis. Thomson Brooks/Cole, 896 pp.

Caulfield, C., and A. Woods, 1998: Turbulent gravitational convection from a point source in a non-uniformly stratified environment. *J. Fluid Mech.*, **360**, 229–248.

Cazenave, A., and W. Llovel, 2010: Contemporary sea level rise. *Annu. Rev. Mar. Sci.*, **2**, 145–173.

Cenedese, C., and P. Linden, 2014: Entrainment in two coalescing axisymmetric turbulent plumes. *J. Fluid Mech.*, **752**, R2.

Chauche´, N., and Coauthors, 2014: Ice-ocean interaction and calving front morphology at two west greenland tidewater outlet glaciers. *The Cryosphere*, **8**, 1457–1468.

Chu, V. W., 2014: Greenland ice sheet hydrology: A review. *Prog. in Phys. Geog.*, **38**, 19–54.

Cowton, T., P. Nienow, A. Sole, J. Wadham, G. Lis, I. Bartholomew, D. Mair, and D. Chandler, 2013: Evolution of drainage system morphology at a land-terminating greenlandic outlet glacier. *J. Geophys. Res.: Earth Surf.*, **118**, 29–41

Cowton, T., D. Slater, A. Sole, D. Goldberg, and P. Nienow, 2015: Modeling the impact of glacial runoff on fjord circulation and submarine melt rate using a new subgrid-scale parameterization for glacial plumes. *J. Geophys. Res.: Oceans*, **120**, 796–812

Echelmeyer, K., T. Clarke, and W. Harrison, 1991: Surficial glaciology of Jakobshavns Isbræ, West Greenland: Part I. Surface morphology. *J. Glaciol.*, **37**, 368–382.

Ellison, T., and J. Turner, 1959: Turbulent entrainment in stratified flows. *J. Fluid Mech.*, **6**, 423–448.

Enderlin, E. M., I. M. Howat, S. Jeong, M.-J. Noh, J. H. Angelen, and M. R. Broeke, 2014: An improved mass budget for the Greenland ice sheet. *Geophys. Res. Lett.*, **41**, 866–872.

Gade, H. G., 1979: Melting of ice in sea water: A primitive model with application to the Antarctic ice shelf and icebergs. *J. Phys. Oceanogr.*, **9**, 189–198.

Gladish, C. V., D. M. Holland, A. Rosing-Asvid, J. W. Behrens, and J. Boje, 2015: Oceanic boundary conditions for jakobshavn glacier. part i: Variability and renewal of ilulissat icefjord waters, 2001–14*. *J. Phys. Oceanogr.*, **45**, 3-32.

Hellmer, H., and D. Olbers, 1989: A two-dimensional model for the thermohaline circulation under an ice shelf. *Antarct. Sci.*, **1**, 325–336.

Holland, D., and A. Jenkins, 1999: Modeling thermodynamic ice-ocean interactions at the base of an ice shelf. *J. Phys. Oceanogr.*, **29**, 1787–1800.

Huang, R. X., 1993: Real freshwater flux as a natural boundary condition for the salinity balance and thermohaline circulation forced by evaporation and precipitation. *J. Phys. Oceanogr.*, **23**, 2428–2446.

Jackett, D. R., and T. J. Mcdougall, 1995: Minimal adjustment of hydrographic profiles to achieve static stability. *J. Atmos. Oceanic Technol.*, **12**, 381–389.

Jackson, R., F. Straneo, and D. Sutherland, 2014: Externally forced fluctuations in ocean temperature at Greenland glaciers in non-summer months. *Nat. Geosci.*, **7**, 503–508.

Jenkins, A., 1999: The impact of melting ice on ocean waters. *J. Phys. Oceanogr.*, **29**, 2370–2381.

Jenkins, A., 2011: Convection-driven melting near the grounding lines of ice shelves and tidewater glaciers. *J. Phys. Oceanogr.*, **41**, 2279–2294.

Joughin, I., R. B. Alley, and D. M. Holland, 2012: Ice-sheet response to oceanic forcing. *Science*, **338**, 1172–1176.

Kaye, N., 2008. Turbulent plumes in stratified environments: A review of recent work. *Atmos.-Ocean*, **46**, 433–441.

Kaye, N., and P. Linden, 2004: Coalescing axisymmetric turbulent plumes. *J. Fluid Mech.*, **502**, 41–63.

Kimura, S., P. R. Holland, A. Jenkins, and M. Piggott, 2014: The effect of meltwater plumes on the melting of a vertical glacier face. *J. Physical Oceanogr.*, **44**, 3099–3117.

Kjeldsen, K. K., J. Mortensen, J. Bendtsen, D. Petersen, K. Lennert, and S. Rysgaard, 2014: Ice-dammed lake drainage cools and raises surface salinities in a tidewater outlet glacier fjord, west Greenland. *J. Geophys. Res.: Earth Surf.*, **119**, 1310–1321.

Kopp, R. E., R. M. Horton, C. M. Little, J. X. Mitrovica, M. Oppenheimer, D. J. Rasmussen, B. H. Strauss, and C. Tebaldi, 2014: Probabilistic 21st and 22nd century sea-level projections at a global network of tide-gauge sites. *Earth's Future*, **2**, 383–406.

Linden, P., 2000: Convection in the environment. Cambridge University Press, 289–345 pp.

List, E., 1982: Turbulent jets and plumes. *Annu. Rev. Fluid Mech.*, **14**, 189–212.

Losch, M., 2008: Modeling ice shelf cavities in a z coordinate ocean general circulation model. *J. Geophys. Res.*, **113**, 1–15.

Marshall, J., A. Adcroft, C. Hill, L. Perelman, and C. Heisey, 1997: A finite-volume, incompressible Navier Stokes model for studies of the ocean on parallel computers. *J. Geophys. Res.: Oceans*, **102**, 5753–5766.

Marshall, J., H. Jones, and C. Hill, 1998: Efficient ocean modeling using non-hydrostatic algorithms. *J. Mar. Syst.*, **18**, 115–134.

Mortensen, J., J. Bendtsen, R. Motyka, K. Lennert, M. Truffer, M. Fahnestock, and S. Rysgaard, 2013: On the seasonal freshwater stratification in the proximity of fast-flowing tidewater outlet glaciers in a sub-Arctic sill fjord. *J. Geophys. Res.: Oceans*, **118**, 1382– 1395.

Mortensen, J., K. Lennert, J. Bendtsen, and S. Rysgaard, 2011: Heat sources for glacial melt in a sub-Arctic fjord (Godthåbsfjord) in contact with the Greenland Ice Sheet. *J. Geophys. Res.: Oceans*, **116** (C1).

Morton, B., G. Taylor, and J. Turner, 1956: Turbulent gravitational convection from maintained and instantaneous sources. *Proc. Roy. Soc. London*, **234**, 1–23.

Motyka, R. J., W. P. Dryer, J. Amundson, M. Truffer, and M. Fahnestock, 2013: Rapid submarine melting driven by subglacial discharge, LeConte Glacier, Alaska. *J. Geophys. Res.*, **40**, 5153–5158.

Motyka, R. J., L. Hunter, K. a. Echelmeyer, and C. Connor, 2003: Submarine melting at the terminus of a temperate tidewater glacier, LeConte Glacier, Alaska, U.S.A. *Ann. Glaciol.*, **36**, 57–65.

Mugford, R., and J. Dowdeswell, 2011: Modeling glacial meltwater plume dynamics and sedimentation in high-latitude fjords. *J. Geophys. Res.: Earth Surf.*, **116** (F1).

Rignot, E., M. Koppes, and I. Velicogna, 2010: Rapid submarine melting of the calving faces of West Greenland glaciers. *Nat. Geosci.*, **3**, 187–191.

Salcedo-Castro, J., D. Bourgault, and B. Deyoung, 2011: Circulation induced by subglacial discharge in glacial fjords: Results from idealized numerical simulations. *Cont. Shelf Res.*, **31**, 1396–1406.

Sciascia, R., C. Cenedese, D. Nicol, P. Heimbach, and F. Straneo, 2014: Impact of periodic intermediary flows on submarine melting of a Greenland glacier. *J. Geophys. Res.: Oceans.*, **119**, 7078– 7098

Sciascia, R., F. Straneo, C. Cenedese, and P. Heimbach, 2013: Seasonal variability of submarine melt rate and circulation in an East Greenland fjord. *J. Geophys. Res.: Oceans.*, **118**, 2492– 2506.

Slater, D., P. Nienow, T. Cowton, D. Goldberg, and A. Sole, 2015: Effect of near-terminus subglacial hydrology on tidewater glacier submarine melt rates. *Geophys. Res. Lett.*, **42**, 2861– 2868.

Straneo, F., R. G. Curry, D. A. Sutherland, G. S. Hamilton, C. Cenedese, K. Våge, and L. A. Stearns, 2011: Impact of fjord dynamics and glacial runoff on the circulation near Helheim Glacier. *Nat. Geosci.*, **4**, 322–327.

Straneo, F., G. S. Hamilton, D. A. Sutherland, L. A. Stearns, F. Davidson, M. O. Hammill, G. B. Stenson, and A. Rosing-Asvid, 2010: Rapid circulation of warm subtropical waters in a major glacial fjord in East Greenland. *Nat. Geosci.*, **3**, 182– 186.

Straneo, F., and P. Heimbach, 2013: North Atlantic warming and the retreat of Greenland's outlet glaciers. *Nature*, **504**, 36–43.

Straneo, F., and Coauthors, 2012: Characteristics of ocean waters reaching Greenland's glaciers. *Ann. Glaciol.*, **53**, 202–210.

Sutherland, D. A., and F. Straneo, 2012: Estimating ocean heat transports and submarine melt rates in Sermilik Fjord, Greenland, using lowered acoustic Doppler current profiler (LADCP) velocity profiles. *Ann. Glaciol.*, **53**, 50–58.

Sutherland, D. A., F. Straneo, and R. S. Pickart, 2014: Characteristics and dynamics of two major greenland glacial fjords. *J. Geophys. Res.: Oceans*, **119**, 3767–3791.

Syvitski, J., 1989: On the deposition of sediment within glacier-influenced fjords: oceanographic controls. *Mar. Geol.*, **85**, 301–329.

Turner, J., 1973: Buoyancy effects in Fluids. Cambridge University Press, 412 pp.

Turner, J. S., 1966: Jets and plumes with negative or reversing buoyancy. *J. Fluid Mech*., **26**, 779–792.

Woods, A. W., 2010: Turbulent plumes in nature. *Annu. Rev. Fluid Mech*., **42**, 391– 412.

Xu, Y., E. Rignot, I. Fenty, D. Menemenlis, and M. M. Flexas, 2013: Subaqueous melting of Store Glacier, west Greenland from three-dimensional, high-resolution numerical modeling and ocean observations. *Geophys. Res. Lett*., **40** , 4648–4653.

Xu, Y., E. Rignot, D. Menemenlis, and M. Koppes, 2012: Numerical experiments on subaqueous melting of Greenland tidewater glaciers in response to ocean warming and enhanced subglacial discharge. *Ann. Glaciol*., **53**, 229–234.

CHAPTER III

Andresen, C.S., Kjeldsen, K.K., Harden B., Nørgaard-Pedersen N., and K H. Kjær, 2014: Outlet glacier dynamics and bathymetry at Upernavik Isstrøm and Upernavik Isfjord North-West Greenland. *Geological Survey of Denmark and Greenland Bulletin*, **31**, 79–82.

Azetsu-Scott, K., and F.C. Tan, 1997: Oxygen isotope studies from Iceland to an East Greenland Fjord: Behaviour of glacial meltwater plume. *Mar. Chem*., **56**, 239-251.

Bartholomaus, T. C., and Coauthors, 2016: Contrasts in the response of adjacent fjords and glaciers to surface melt in western Greenland. *Ann. Glaciol*., 1-14.

Beaird, N., Straneo, F., and W. Jenkins, 2015: Spreading of Greenland meltwaters in the ocean revealed by noble gases. *Geophys. Res. Lett*., **42**, 7705-7713.

Bendtsen, J., Mortensen, J., Lennert, K., and S. Rysgaard, 2015: Heat sources for glacial ice melt in a west Greenland tidewater outlet glacier fjord: The role of subglacial freshwater discharge. *Geophys. Res. Lett*., **42**, 4089-4095.

Boghosian, A., Tinto, K., Cochran, J. R., Porter, D., Elieff, S., Burton, B. L., and R.E. Bell, 2015: Resolving bathymetry from airborne gravity along Greenland fjords. J. *Geophys. Res.: Solid Earth*, **120**, 8516-8533.

Carroll, D., Sutherland, D. A., Shroyer, E. L., Nash, J. D., Catania, G. A., and L.A. Stearns, 2015: Modeling turbulent subglacial meltwater plumes: Implications for fjord-scale buoyancy-driven circulation. *J. Phys. Oceanogr*., **45**, 2169-2185.

Chauché, N., Hubbard, A., Gascard, J. C., Box, J. E., Bates, R., Koppes, M., and H. Patton, 2014:. Ice–ocean interaction and calving front morphology at two west Greenland tidewater outlet glaciers. *The Cryosphere*, **8**, 1457-1468.

Christoffersen, P., Mugford, R. I., Heywood, K. J., Joughin, I., Dowdeswell, J. A., Syvitski, J. P. M., and T.J. Benham, 2011: Warming of waters in an East Greenland fjord prior to glacier retreat: mechanisms and connection to large-scale atmospheric conditions. *The Cryosphere*, 5, 701-714.

Cofaigh, C. Ó., Dowdeswell, J. A., Jennings, A. E., Hogan, K. A., Kilfeather, A., Hiemstra, J. F., and J.M. Lloyd, 2013: An extensive and dynamic ice sheet on the West Greenland shelf during the last glacial cycle. *Geology*, **41**, 219-222.

Cowton, T., Slater, D., Sole, A., Goldberg, D., and P. Nienow, 2015: Modeling the impact of glacial runoff on fjord circulation and submarine melt rate using a new subgrid-scale parameterization for glacial plumes. *J. Geophys. Res.: Oceans*, **120**, 796-812.

Cuffey, K. M., and W.S.B Paterson, 2010: The physics of glaciers, Academic Press, 704 pp.

Dowdeswell, J. A., Hogan, K. A., Cofaigh, C. Ó., Fugelli, E. M. G., Evans, J., and R. Noormets, 2014. Late Quaternary ice flow in a West Greenland fjord and cross-shelf trough system: submarine landforms from Rink Isbrae to Uummannaq shelf and slope. *Quat. Sci. Rev.*, **92**, 292-309.

Enderlin, E. M., Howat, I. M., Jeong, S., Noh, M. J., Angelen, J. H., and M.R. van den Broeke, 2014: An improved mass budget for the Greenland ice sheet. *Geophys. Res. Lett.*, **41**, 866-872.

Fried, M. J., Catania, G. A., Bartholomaus, T. C., Duncan, D., Davis, M., Stearns, L. A., and D.A. Sutherland, 2015: Distributed subglacial discharge drives significant submarine melt at a Greenland tidewater glacier. *Geophys. Res. Lett.*, **42**, 9328-9336.

Gladish, C. V., Holland, D. M., Rosing-Asvid, A., Behrens, J. W., and J. Boje, 2015: Oceanic Boundary Conditions for Jakobshavn Glacier. Part I: Variability and Renewal of Ilulissat Icefjord Waters, 2001–14*. *J. Phys. Oceanogr.*, **45**, 3-32.

Holland, D. M., and A. Jenkins, 1999: Modeling thermodynamic ice-ocean interactions at the base of an ice shelf. *J. Phys. Oceanogr.*, **29**, 1787-1800.

Holland, D. M., Thomas, R. H., De Young, B., Ribergaard, M. H., and B. Lyberth, 2008: Acceleration of Jakobshavn Isbrae triggered by warm subsurface ocean waters. *Nat. Geosci.*, **1**, 659-664.

Inall, M. E., Murray, T., Cottier, F. R., Scharrer, K., Boyd, T. J., Heywood, K. J., and S.L. Bevan, 2014: Oceanic heat delivery via Kangerdlugssuaq Fjord to the south-east Greenland ice sheet. *J. Geophys. Res.: Oceans*, **119**, 631-645.

Jackson, R. H., Straneo, F., and D.A. Sutherland, 2014: Externally forced fluctuations in ocean temperature at Greenland glaciers in non-summer months. *Nat. Geosci.*, **7**, 503-508.

Jackson, R., and F. Straneo, 2016: Heat, salt, and freshwater budgets for a glacial fjord in Greenland. *J. Phys. Oceanogr.*, **46**, 2735-2768.

Jenkins, A., Nicholls, K. W., and H.F. Corr, 2010: Observation and parameterization of ablation at the base of Ronne Ice Shelf, Antarctica. *J. Phys. Oceanogr.*, **40**, 2298-2312.

Jenkins, A., 2011: Convection-driven melting near the grounding lines of ice shelves and tidewater glaciers. *J. Phys. Oceanogr.*, **41**, 2279-2294.

Joughin, I., and T. Moon T, 2015: MEaSUREs Annual Greenland Outlet Glacier Terminus Positions from SAR Mosaics, [73°N, 72°W; 63°N, 32°W]. Boulder, Colorado USA: NASA National Snow and Ice Data Center Distributed Active Archive Center. Accessed October 18, 2015

Killworth, P. D., 1977: Mixing of the Weddell Sea continental slope. *Deep-Sea Res.*, **24**, 427-448.

Lenaerts, J., Le Bars, D., Kampenhout, L., Vizcaino, M., Enderlin, E. M., and M.R. van den Broeke, 2015: Representing Greenland ice sheet freshwater fluxes in climate models. *Geophys. Res. Lett.*, **42**, 6373-6381.

Lewis, S. M., and L.C. Smith, 2009: Hydrologic drainage of the Greenland ice sheet. *Hydrol. Processes*, b, 2004.

Luckman, A., Benn, D. I., Cottier, F., Bevan, S., Nilsen, F., and M. Inall, 2015: Calving rates at tidewater glaciers vary strongly with ocean temperature. *Nat. Commun.*, **6**.

MacAyeal, D. R., 1985: Evolution of tidally triggered meltwater plumes below ice shelves. *Oceanol. Antar. Cont. Shelf*, 133-143.

Moon, T., and I. Joughin, I, 2008: Changes in ice front position on Greenland's outlet glaciers from 1992 to 2007. *J. Geophys. Res.: Earth Surf*, **113** (F2).

Moon, T., Joughin, I., Smith, B., Broeke, M. R., Berg, W. J., Noël, B., and M. Usher, 2014: Distinct patterns of seasonal Greenland glacier velocity. *Geophys. Res. Lett.*, **41**, 7209-7216.

Morlighem, M., Rignot, E., Mouginot, J., Seroussi, H., and E. Larour, 2014: Deeply incised submarine glacial valleys beneath the Greenland ice sheet. *Nat. Geosci.*, **7**, 418-422.

Morlighem, M., E. Rignot, J. Mouginot, H. Seroussi and E. Larour. 2015. IceBridge BedMachine Greenland, Version 2, [73°N, 72°W; 63°N, 32°W]. Boulder, Colorado USA: NASA DAAC at the National Snow and Ice Data Center.

Mortensen, J., Bendtsen, J., Motyka, R. J., Lennert, K., Truffer, M., Fahnestock, M., and S. Rysgaard, 2013: On the seasonal freshwater stratification in the proximity of fast-flowing tidewater outlet glaciers in a sub-Arctic sill fjord. *J. Geophys. Res.: Oceans*, **118**, 1382-1395.

Morton, B., G. Taylor, and J. Turner, 1956: Turbulent gravitational convection from maintained and instantaneous sources. *Proc. Roy. Soc. London*, **234**, 1–23.

Motyka, R. J., Truffer, M., Fahnestock, M., Mortensen, J., Rysgaard, S., and I. Howat, 2011: Submarine melting of the 1985 Jakobshavn Isbræ floating tongue and the triggering of the current retreat. *J. Geophys. Res.: Earth Surf.*, **116** (F1).

Münchow, A., Falkner, K. K., and H. Melling, 2007: Spatial continuity of measured seawater and tracer fluxes through Nares Strait, a dynamically wide channel bordering the Canadian Archipelago. *J. Mar. Res.*, **65**, 759-788.

Münchow, A., Falkner, K. K., and H. Melling, 2015: Baffin Island and West Greenland Current Systems in northern Baffin Bay. *Prog. Oceanogr.*, **132**, 305-317.

Nick, F. M., Vieli, A., Howat, I. M., and I. Joughin, 2009: Large-scale changes in Greenland outlet glacier dynamics triggered at the terminus. *Nat. Geosci.*, **2**, 110-114.

Noël, B., Van De Berg, W. J., Van Meijgaard, E., Kuipers Munneke, P., Van De Wal, R., and M.R. Van Den Broeke, 2015: Evaluation of the updated regional climate model RACMO2.3: summer snowfall impact on the Greenland Ice Sheet. *The Cryosphere*, **9**, 1831-1844.

O'Callaghan, J. F., and D.M. Mark, 1984: The extraction of drainage networks from digital elevation data. Comp. *Vis. Graph. and Image Proc.*, **28**, 323-344.

O'Leary, M., and P. Christoffersen, 2013: Calving on tidewater glaciers amplified by submarine frontal melting. *The Cryosphere*, **7**, 119-128.

Porter, D. F., Tinto, K. J., Boghosian, A., Cochran, J. R., Bell, R. E., Manizade, S. S., and J.G. Sonntag, 2014: Bathymetric control of tidewater glacier mass loss in northwest Greenland. *Earth Planet. Sci. Lett.*, **401**, 40-46.

Rignot, E., Koppes, M., and I. Velicogna, 2010: Rapid submarine melting of the calving faces of West Greenland glaciers. *Nat. Geosci.*, **3**, 187-191.

Rignot, E., Fenty, I., Xu, Y., Cai, C., and C. Kemp, 2015: Undercutting of marine-terminating glaciers in West Greenland. *Geophys. Res. Lett.*, **42**, 5909-5917.

Rignot, E., Fenty, I., Xu, Y., Cai, C., Velicogna, I., Cofaigh, C. Ó., and D. Duncan, 2016: Bathymetry data reveal glaciers vulnerable to ice-ocean interaction in Uummannaq and Vaigat glacial fjords, west Greenland. *Geophys. Res. Lett.*, **43**, 2667-2674.

Rignot, E., Xu, Y., Menemenlis, D., Mouginot, J., Scheuchl, B., Li, X., and C. Cai, 2016: Modeling of ocean-induced ice melt rates of five West Greenland glaciers over the past two decades. *Geophys. Res. Lett.*, **43**, 6374-6382.

Sciascia, R., Straneo, F., Cenedese, C., and P. Heimbach, 2013: Seasonal variability of submarine melt rate and circulation in an East Greenland fjord. *J. Geophys. Res.: Oceans*, **118**, 2492-2506.

Shepherd, A and Coauthors, 2012: A reconciled estimate of ice-sheet mass balance. *Science*, **338**, 1183-1189.

Slater, D. A., Nienow, P. W., Cowton, T. R., Goldberg, D. N., and A.J. Sole, 2015: Effect of near-terminus subglacial hydrology on tidewater glacier submarine melt rates. *Geophys. Res. Lett.*, **42**, 2861-2868.

Slater, D. A., Goldberg, D. N., Nienow, P. W., and T.R. Cowton, 2016: Scalings for Submarine Melting at Tidewater Glaciers from Buoyant Plume Theory. *J. Phys. Oceanogr.*, **46**, 1839-1855.

Smith, P.C., 1975: A streamtube model for bottom boundary currents in the ocean. *Deep-Sea Res. Oceanogr. Abstr.*, **22**, 853-873.

Stevens, L. A., Straneo, F., Das, S. B., Plueddemann, A. J., Kukulya, A. L., and M. Morlighem, 2016: Linking glacially modified waters to catchment-scale subglacial discharge using autonomous underwater vehicle observations. *The Cryosphere*, **10**, 417-432.

Straneo, F., Hamilton, G. S., Sutherland, D. A., Stearns, L. A., Davidson, F., Hammill, M. O., and A. Rosing-Asvid, 2010: Rapid circulation of warm subtropical waters in a major glacial fjord in East Greenland. *Nat. Geosci.*, **3**, 182-186.

Straneo, F., Curry, R. G., Sutherland, D. A., Hamilton, G. S., Cenedese, C., Våge, K., and L.A Stearns, 2011: Impact of fjord dynamics and glacial runoff on the circulation near Helheim Glacier. *Nat. Geosci.*, **4**, 322-327.

Straneo, F., Sutherland, D. A., Holland, D., Gladish, C., Hamilton, G. S., Johnson, H. L., and M. Koppes, 2012: Characteristics of ocean waters reaching Greenland's glaciers. *Ann. Glaciol.*, **53**, 202-210.

Straneo, F., and P. Heimbach, 2013: North Atlantic warming and the retreat of Greenland's outlet glaciers. *Nature*, **504**, 36-43.

Straneo, F. and C. Cenedese, 2015: The Dynamics of Greenland's glacial fjords and their role in climate. *Annu. Rev. Mar. Sci.*, **7**, 89-112.

Sutherland, D. A., and F. Straneo, 2012: Estimating ocean heat transports and submarine melt rates in Sermilik Fjord, Greenland, using lowered acoustic Doppler current profiler (LADCP) velocity profiles. *Ann. Glaciol.*, **53**, 50-58.

Sutherland, D. A., Straneo, F., and R.S. Pickart, 2014: Characteristics and dynamics of two major Greenland glacial fjords. *J. Geophys. Res.: Oceans*, **119**, 3767-3791.

Tarboton, D.G., 1997: A new method for the determination of flow directions and upslope areas in grid digital elevation models. *Water Resour. Res.*, **33**, 309-319.

van den Broeke, M. R., Bamber, J., Ettema, J., Rignot, E., Schrama, E., van de Berg, W. J., and B. Wouters, 2009: Partitioning recent Greenland mass loss. *Science*, **326**, 984-986.

Vieli, A., and F.M. Nick, 2011: Understanding and modelling rapid dynamic changes of tidewater outlet glaciers: issues and implications. *Surv. in Geophys.*, **32**, 437-458.

Xu, Y., Rignot, E., Menemenlis, D., and M. Koppes, 2012: Numerical experiments on subaqueous melting of Greenland tidewater glaciers in response to ocean warming and enhanced subglacial discharge. *Ann. Glaciol.*, **53**, 229-234.

Xu, Y., Rignot, E., Fenty, I., Menemenlis, D., and M. Flexas, 2013: Subaqueous melting of Store Glacier, west Greenland from three-dimensional, high-resolution numerical modeling and ocean observations. *Geophys. Res. Lett.*, **40**, 4648-4653.

CHAPTER IV

Adcroft, A., C. Hill, and J. Marshall, 1997: Representation of topography by shaved cells in a height coordinate ocean model. *Mon. Weather Rev.*, **125**, 2293–2315.

Arakawa, A., and V. R. Lamb, 1977: Computational design of the basic dynamical processes of the UCLA general circulation model. *Advances in Research and Applications*, J. Chang, Eds., Methods in Computational Physics Series, Vol. 17, Elsevier, 173–265.

Arneborg, L., and B. Liljebladh, 2009: Overturning and dissipation caused by baroclinic tidal flow near the sill of a fjord basin. *J. Phys. Oceanogr.*, **39**, 2156–2174.

Arneborg, L., C. P. Erlandsson, B. Liljebladh, and A. Stigebrandt, 2004: The rate of inflow and mixing during deep-water renewal in a sill fjord. *Limnol. Oceanogr*, **49**, 768–777.

Aure, J., and A. Stigebrandt, 1990: Quantitative estimates of the eutrophication effects of fish farming on fjords. *Aquaculture*, **90**, 135–156.

Aure, J., J. Molvær, and A. Stigebrandt, 1996: Observations of inshore water exchange forced by a fluctuating offshore density field. *Mar. Pollut. Bull.*, **33**, 112–119.

Baines, W., and J. Turner, 1969: Turbulent buoyant convection from a source in a confined region. *J. Fluid Mech.*, **37**, 51–80.

Bamber, J., M. den Broeke, J. Ettema, J. Lenaerts, and E. Rignot, 2012: Recent large increases in freshwater fluxes from greenland into the north Atlantic. *Geophys. Res. Lett.*, **39** (19).

Bartholomaus, T. C., and Coauthors, 2016: Contrasts in the response of adjacent fjords and glaciers to ice-sheet surface melt in west greenland. *Ann. Glaciol.*, 1–14.

Beaird, N., F. Straneo, and W. Jenkins, 2015: Spreading of greenland meltwaters in the ocean revealed by noble gases. *Geophys. Res. Lett.*, **42**, 7705–7713.

Bendtsen, J., J. Mortensen, and S. Rysgaard, 2015: Modelling subglacial discharge and its influence on ocean heat transport in arctic fjords. *Ocean Dynamics*, **65**, 1535–1546.

Berntsen, J., J. Xing, and A. M. Davies, 2009: Numerical studies of flow over a sill: sensitivity of the non-hydrostatic effects to the grid size. *Ocean Dynamics*, **59**, 1043–1059.

Carroll, D., D. A. Sutherland, E. L. Shroyer, J. D. Nash, G. A. Catania, and L. A. Stearns, 2015: Modeling turbulent subglacial meltwater plumes: Implications for fjord-scale buoyancy-driven circulation. *J. Phys. Oceanogr.*, **45**, 2169–2185.

Carroll, D., and Coauthors, 2016: The impact of glacier geometry on meltwater plume structure and submarine melt in greenland fjords. *Geophys. Res. Lett.*, **43**, 9739–9748.

Chauché N., A. Hubbard, J.C. Gascard, J. Box, R. Bates, M. Koppes, A. Sole, P. Christoffersen, and H. Patton, 2014: Ice–ocean interaction and calving front morphology at two west Greenland tidewater outlet glaciers. *The Cryosphere*, **8**, 1457–1468.

Cottier, F., V. Tverberg, M. Inall, H. Svendsen, F. Nilsen, and C. Griffiths, 2005: Water mass modification in an arctic fjord through cross-shelf exchange: The seasonal hydrography of kongsfjorden, svalbard. *J. Geophys. Res.: Oceans*, **110** (C12).

Cowton, T., D. Slater, A. Sole, D. Goldberg, and P. Nienow, 2015: Modeling the impact of glacial runoff on fjord circulation and submarine melt rate using a new subgrid-scale parameterization for glacial plumes. *J. Geophys. Res.: Oceans*, **120**, 796–812.

Cowton, T., A. Sole, P. Nienow, D. Slater, D. Wilton, and E. Hanna, 2016: Controls on the transport of oceanic heat to kangerdlugssuaq glacier, east greenland. *J. Glaciol.*, **62**, 1167-1180.

Deremble, B., 2016: Convective plumes in rotating systems. *J. Fluid Mech.*, **799**, 27–55.

Enderlin, E. M., I. M. Howat, S. Jeong, M.J. Noh, J. H. Angelen, and M. R. van den Broeke, 2014: An improved mass budget for the Greenland ice sheet. *Geophys. Res. Lett*, **41** (3), 866–872.

Enderlin, E. M., G. S. Hamilton, F. Straneo, and D. A. Sutherland, 2016: Iceberg melt-water fluxes dominate the freshwater budget in greenland's iceberg-congested glacial fjords. *Geophys. Res. Lett.*, **43**, 11287–11294.

Farmer, D. M., and R. A. Denton, 1985: Hydraulic control of flow over the sill in observatory inlet. *J. Geophys. Res.: Oceans*, **90**, 9051–9068.

Farmer, D. M., and H. J. Freeland, 1983: The physical oceanography of fjords. *Prog. Oceanogr.*, **12**, 147IN1195–194,219.

Fernando, H., R. Chen, and B. Ayotte, 1998: Development of a point plume in the presence of background rotation. *Phys. Fluids*, **10**, 2369–2383.

Garabato, A. C. N., A. Forryan, P. Dutrieux, L. Brannigan, L. C. Biddle, K. J. Heywood, A. Jenkins, Y. L. Firing, and S. Kimura, 2017: Vigorous lateral export of the meltwater outflow from beneath an antarctic ice shelf. *Nature*, **542**, 219-222.

Garvine, R. W., and M. M. Whitney, 2006: An estuarine box model of freshwater delivery to the coastal ocean for use in climate models. *J. Mar. Res.*, **64**, 173–194.

Geyer, W., and G. Cannon, 1982: Sill processes related to deep water renewal in a fjord. *J. Geophys. Res.: Oceans*, **87**, 7985–7996.

Geyer, W., and D. Ralston, 2011: The dynamics of strongly stratified estuaries. Treat. on *Estuar. and Coastal Sci.*, **2**, 37–51.

Gillibrand, P. A., M. E. Inall, E. Portilla, and P. Tett, 2013: A box model of the seasonal exchange and mixing in regions of restricted exchange: application to two contrasting scottish inlets. *Environ. Model. and Soft.*, **43**, 144–159.

Gladish, C. V., D. M. Holland, A. Rosing-Asvid, J. W. Behrens, and J. Boje, 2015: Oceanic boundary conditions for jakobshavn glacier. part i: Variability and renewal of ilulissat icefjord waters, 2001–14*. *J. Phys. Oceanogr.*, **45**, 3–32.

Godin, G., 1991: The analysis of tides and currents. *Tidal Hydrodynamics*, Wiley, New York, 675-709.

Harden, B., I. Renfrew, and G. Petersen, 2011: A climatology of wintertime barrier winds off southeast greenland. *J. Clim.*, **24**, 4701–4717.

Helfrich, K. R., and T. M. Battisti, 1991: Experiments on baroclinic vortex shedding from hydrothermal plumes. *J. Geophys. Res.: Oceans*, **96**, 12511–12518.

Heuzé, C., A. Wåhlin, H. L. Johnson, and A. Münchow, 2016: Pathways of meltwater export from petermann glacier, greenland. *J. Phys. Oceanogr.*, **47**, 405-418.

Holland, D., and A. Jenkins, 1999: Modeling thermodynamic ice-ocean interactions at the base of an ice shelf. *J. Phys. Oceanogr.*, **29**, 1787–1800.

Huang, R.X., 1993: Real freshwater flux as a natural boundary condition for the salinity balance and thermohaline circulation forced by evaporation and precipitation. *J. Phys. Oceanogr.*, **23**, 2428–2446.

Inall, M., F. Cottier, C. Griffiths, and T. Rippeth, 2004: Sill dynamics and energy transformation in a jet fjord. *Ocean Dynamics*, **54**, 307–314.

Jackett, D. R., and T. J. Mcdougall, 1995: Minimal adjustment of hydrographic profiles to achieve static stability. *J. Atmos. Oceanic Technol.*, **12**, 381–389.

Jackson, R., and F. Straneo, 2016: Heat, Salt, and Freshwater Budgets for a Glacial Fjord in Greenland. *J. Phys. Oceanogr.*, **46**, 2735–2768,

Jackson, R., F. Straneo, and D. Sutherland, 2014: Externally forced fluctuations in ocean temperature at Greenland glaciers in non-summer months. *Nat. Geosci.*, **7**, 503–508.

Jenkins, A., 2011: Convection-driven melting near the grounding lines of ice shelves and tidewater glaciers. *J. Phys. Oceanogr.*, **41**, 2279–2294.

Killworth, P., and J. Turner, 1982: Plumes with time-varying buoyancy in a confined region. *Geophys. Astrophys. Fluid Dyn.*, **20**, 265–291.

Klinck, J. M., J. J. O'Brien, and H. Svendsen, 1981: A simple model of fjord and coastal circulation interaction. *J. Phys. Oceanogr.*, **11**, 1612–1626.

Large, W. G., J. C. McWilliams, and S. C. Doney, 1994: Oceanic vertical mixing: A review and a model with a nonlocal boundary layer parameterization. *Rev. Geophys.*, **32**, 363–403.

Love, K. B., B. Hallet, T. L. Pratt, and S. O'Neel, 2016: Observations and modeling of fjord sedimentation during the 30 year retreat of columbia glacier, ak. *J. Glaciol.*, **62**, 778–793.

Mankoff, K. D., F. Straneo, C. Cenedese, S. B. Das, C. G. Richards, and H. Singh, 2016: Structure and dynamics of a subglacial discharge plume in a greenlandic fjord. *J. Geophys. Res.: Oceans*, **121**, 8670–8688.

Marshall, J., A. Adcroft, C. Hill, L. Perelman, and C. Heisey, 1997: A finite-volume, incompressible Navier Stokes model for studies of the ocean on parallel computers. *J. Geophys. Res.: Oceans*, **102**, 5753–5766.

Moffat, C., 2014: Wind-driven modulation of warm water supply to a proglacial fjord, jorge montt glacier, patagonia. *Geophys. Res. Lett.*, **41**, 3943–3950.

Morlighem, M., E. Rignot, and J. Willis, 2016: Improving bed topography mapping of greenland glaciers using nasas oceans melting greenland (omg) data. *Oceanography*, **29**, 40.

Mortensen, J., K. Lennert, J. Bendtsen, and S. Rysgaard, 2011: Heat sources for glacial melt in a sub-Arctic fjord (Godthåbsfjord) in contact with the Greenland Ice Sheet. *J. Geophys. Res.: Ocean*, **116**, C1.

Mortensen, J., J. Bendtsen, R. Motyka, K. Lennert, M. Truffer, M. Fahnestock, and S. Rysgaard, 2013: On the seasonal freshwater stratification in the proximity of fast-flowing tidewater outlet glaciers in a sub-Arctic sill fjord. *J. Geophys. Res.: Ocean,* **118**, 1382–1395.

Mortensen, J., J. Bendtsen, K. Lennert, and S. Rysgaard, 2014: Seasonal variability of the circulation system in a west greenland tidewater outlet glacier fjord, godthåbsfjord (64 n). *J. Geophys. Res.: Earth Surf.*, **119**, 2591–2603.

Morton, B., G. Taylor, and J. Turner, 1956: Turbulent gravitational convection from maintained and instantaneous sources. *Proc. Roy. Soc. London*, **234**, 1–23.

Motyka, R. J., L. Hunter, K. a. Echelmeyer, and C. Connor, 2003: Submarine melting at the terminus of a temperate tidewater glacier, LeConte Glacier, Alaska, U.S.A. *Ann. Glaciol.*, **36**, 57–65.

Motyka, R. J., W. P. Dryer, J. Amundson, M. Truffer, and M. Fahnestock, 2013: Rapid submarine melting driven by subglacial discharge, LeConte Glacier, Alaska. *Geophys. Res. Lett.*, **40**, 5153–5158.

Nilsen, F., F. Cottier, R. Skogseth, and S. Mattsson, 2008: Fjord–shelf exchanges controlled by ice and brine production: the interannual variation of atlantic water in isfjorden, svalbard. *Cont. Shelf Res.*, **28**, 1838–1853.

Padman, L., and S. Erofeeva, 2004: A barotropic inverse tidal model for the arctic ocean. *Geophys. Res. Lett.*, **31** (2).

Pedlosky, J., 2013: Geophysical Fluid Dynamics. Springer Science and Business Media, 710 pp.

Pickart, R. S., D. J. Torres, and P. S. Fratantoni, 2005: The east greenland spill jet. J. *Phys. Oceanogr.*, **35**, 1037–1053.

Qiu, B., N. Imasato, and T. Awaji, 1988: Baroclinic instability of buoyancy-driven coastal density currents. *J. Geophys. Res.: Oceans*, **93**, 5037–5050.

Rignot, E., I. Fenty, Y. Xu, C. Cai, I. Velicogna, C.O′. Cofaigh, J. Dowdeswell, W. Weinrebe, G. Catania, and D. Duncan, 2016: Bathymetry data reveal glaciers vulnerable to ice-ocean interaction in uummannaq and vaigat glacial fjords, west greenland. *Geophys. Res. Lett.*, **43**, 2667–2674.

Sciascia, R., F. Straneo, C. Cenedese, and P. Heimbach, 2013: Seasonal variability of submarine melt rate and circulation in an East Greenland fjord. *J. Geophys. Res.: Oceans*, **118**, 2492–2506.

Sciascia, R., C. Cenedese, D. Nicol, P. Heimbach, and F. Straneo, 2014: Impact of periodic intermediary flows on submarine melting of a Greenland glacier. *J. Geophys. Res.: Oceans*, **119**, 7078-7098.

Slater, D., P. Nienow, T. Cowton, D. Goldberg, and A. Sole, 2015: Effect of near-terminus subglacial hydrology on tidewater glacier submarine melt rates. *Geophys. Res. Lett.*, **42**, 2861-2868.

Slater, D., P. Nienow, A. Sole, T. Cowton, R. Mottram, P. Langen, and D. Mair, 2017: Spatially distributed runoff at the grounding line of a large greenlandic tidewater glacier inferred from plume modelling. *J. Glaciol.*, **63**, 309-323.

Slater, D. A., D. N. Goldberg, P. W. Nienow, and T. R. Cowton, 2016: Scalings for submarine melting at tidewater glaciers from buoyant plume theory. *J. Phys. Oceanogr.*, **46**, 1839–1855.

Speer, K. G., 1989: A forced baroclinic vortex around a hydrothermal plume. *Geophys. Res. Lett.*, **16**, 461–464.

Speer, K. G., and J. Marshall, 1995: The growth of convective plumes at seafloor hot springs. *J. Mar. Res.*, **53**, 1025–1057.

Staalstrøm, A., L. Arneborg, B. Liljebladh, and G. Broström, 2015: Observations of turbulence caused by a combination of tides and mean baroclinic flow over a fjord sill. *J. Phys. Oceanogr.*, **45**, 355–368.

Stashchuk, N., M. Inall, and V. Vlasenko, 2007: Analysis of supercritical stratified tidal flow in a scottish fjord. *J. Phys. Oceanogr.*, **37**, 1793–1810.

Stevens, L. A., F. Straneo, S. B. Das, A. J. Plueddemann, A. L. Kukulya, and M. Morlighem, 2016: Linking glacially modified waters to catchment-scale subglacial discharge using autonomous underwater vehicle observations. *The Cryosphere*, **10**, 417–432.

Stigebrandt, A., 1987: A model for the vertical circulation of the baltic deep water. *J. Phys. Oceanogr.*, **17**, 1772–1785.

Stigebrandt, A., 2012: Hydrodynamics and circulation of fjords. Encyclopedia of Lakes and Reservoirs, Springer, 327–344.

Stigebrandt, A., and J. Aure, 1989: Vertical mixing in basin waters of fjords. *J. Phys. Oceanogr.*, **19**, 917–926.

Støylen, E., and I. Fer, 2014: Tidally induced internal motion in an arctic fjord. *Nonlin. Proc. In Geophys.*, **21**, 87–100.

Støylen, E., and J. E. H. Weber, 2010: Mass transport induced by internal kelvin waves beneath shore-fast ice. *J. Geophys. Res.: Oceans*, **115**, C03022.

Straneo, F., and C. Cenedese, 2015: The dynamics of greenland's glacial fjords and their role in climate. *Annu. Rev. Mar. Sci.*, **7**, 89–112.

Straneo, F., and P. Heimbach, 2013: North Atlantic warming and the retreat of Greenland's outlet glaciers. *Nature*, **504**, 36–43.

Straneo, F., G. S. Hamilton, D. A. Sutherland, L. A. Stearns, F. Davidson, M. O. Hammill, G. B. Stenson, and A. Rosing-Asvid, 2010: Rapid circulation of warm subtropical waters in a major glacial fjord in East Greenland. *Nat. Geosci.*, **3**, 182–186.

Straneo, F., R. G. Curry, D. A. Sutherland, G. S. Hamilton, C. Cenedese, K. Våge, and L. A. Stearns, 2011: Impact of fjord dynamics and glacial runoff on the circulation near Helheim Glacier. *Nat. Geosci.*, **4**, 322–327.

Sulak, D., 2016: Iceberg properties and distributions in three greenlandic fjords using satellite imagery. M.S. thesis, Dept. of Earth Sciences, The University of Oregon, 50 pp.

Sulak, D., D. Sutherland, E. Enderlin, L. Stearns, and G. Hamilton (2017), Iceberg properties and distributions in three greenlandic fjords using satellite imagery. *Ann. Glaciol.*, 1-15.

Sutherland, D. A., and F. Straneo, 2012: Estimating ocean heat transports and submarine melt rates in Sermilik Fjord, Greenland, using lowered acoustic Doppler current profiler (LADCP) velocity profiles. *Ann. Glaciol*, **53**, 50–58.

Sutherland, D. A., F. Straneo, and R. S. Pickart, 2014: Characteristics and dynamics of two major greenland glacial fjords. *J. Geophys. Res.: Oceans, 119*, 3767–3791.

Svendsen, H., and R. O. Thompson, 1978: Wind-driven circulation in a fjord. *J. Phys. Oceanogr*., **8**, 703–712.

Svendsen, H., and Coauthors, 2002: The physical environment of kongsfjorden–krossfjorden, an arctic fjord system in svalbard. *Polar Res*., **21**, 133–166.

Tseng, Y.H., F. O. Bryan, and M. M. Whitney, 2016: Impacts of the representation of riverine freshwater input in the community earth system model. *Ocean Modelling*, **105**, 71–86.

van den Broeke, M. R., J. Bamber, J. Ettema, E. Rignot, E. Schrama, W. J. van de Berg, E. van Meijgaard, I. Velicogna, and B. Wouters, 2009: Partitioning recent greenland mass loss. *Science*, **326**, 984–986.

Walters, R. A., E. Josberger, and C. Driedger, 1988: Columbia bay, alaska: an upside down' estuary. *Estuarine, Coastal Shelf Sci*., **26**, 607–617.

Xu, Y., E. Rignot, D. Menemenlis, and M. Koppes, 2012: Numerical experiments on subaqueous melting of Greenland tidewater glaciers in response to ocean warming and enhanced subglacial discharge. *Ann. Glaciol*., **53**, 229–234.

Xu, Y., E. Rignot, I. Fenty, D. Menemenlis, and M. M. Flexas, 2013: Subaqueous melting of Store Glacier, west Greenland from three-dimensional, high-resolution numerical modeling and ocean observations. *Geophys. Res. Lett*., **40**, 4648–4653.